

# D2.3 – Report on simulation framework for H<sub>2</sub>/O<sub>2</sub> and H<sub>2</sub>/air combustion

Marco Vivenzo, Florence Cameron, Huanhuan Xu, Joachim Beeckmann, Michael Gauding, and Heinz Pitsch | RWTH Aachen University – ITV

Alex Garcia Vergara, Johannes Losacker, and Nico Schmitz | RWTH Aachen University – IOB

Daniel Mira, Eduardo Pérez, Emiliano Fortes and Jon Lumbreras | Barcelona Supercomputing Center

January 2025



## Credits

Copyright © 2025 HyInHeat project

## Disclaimer

The sole responsibility of this publication lies with the author.  
The European Union is not responsible for any use that may be  
made of the information contained therein.



This project has received funding from the European Union's Horizon Europe research and innovation programme under grant agreement No 101091456.

## Technical references

Grant Agreement N°	101091456	Acronym	HyInHeat
Full Title	Hydrogen Technologies for Decarbonization of Industrial Heating Processes		
Work Package (WP)	WP2		
Authors	Marco Vivenco, Florence Cameron, Alex Garcia Vergara, Eduardo Pérez, Huanhuan Xu, Joachim Beeckmann, Michael Gauding, Heinz Pitsch, Johannes Losacker, Nico Schmitz, Emiliano Fortes, Jon Lumbreras and Daniel Mira		
Leading organisation	RWTH Aachen University		
Date of publication	31/01/2025		
Contributors			
Document Type	R - Document, report		
Document Title	Report on simulation framework for H <sub>2</sub> /O <sub>2</sub> and H <sub>2</sub> /air combustion		
Dissemination Level	Public		

## Document history

Version	Date	Partner	Author
1	7/11/2024	RWTH-ITV	Marco Vivenco
2	13/12/2024	RWTH-IOB, BSC	Alex Garcia Vergara and Eduardo J. Pérez
3	18/12/2024	RWTH-ITV	Marco Vivenco and Florence Cameron
4	03/01/2025	RWTH-ITV, BSC, RWTH-IOB	Alex Garcia Vergara, Florence Cameron, Eduardo J. Pérez, and Marco Vivenco
5	17/01/2025	RWTH-ITV, BSC, RWTH-IOB	Alex Garcia Vergara, Florence Cameron, and Eduardo J. Pérez
Final	30/01/2025	RWTH-ITV	Marco Vivenco and Heinz Pitsch

## Content

Technical references .....	3
Document history .....	3
Content .....	4
Tables & figures .....	6
List of abbreviations .....	9
<b>1 Introduction .....</b>	<b>10</b>
1.1 Objective and structure .....	10
<b>2 Turbulent H<sub>2</sub> jet flame experiments .....</b>	<b>11</b>
2.1 Description of the experimental setup and techniques .....	11
2.1.1 Jet burner configuration .....	11
2.1.2 OH* chemiluminescence setup .....	12
2.1.3 LIBS setup .....	12
2.2 Diffusion flame measurements .....	12
2.3 Premixed flame measurements .....	16
<b>3 Tabulated models for thermo-diffusive instabilities .....</b>	<b>18</b>
3.1 Introduction .....	18
3.2 LES combustion model for preferential diffusion .....	20
3.3 Model A description .....	21
3.4 Model A validation .....	23
3.5 Model B description in the frame of laminar combustion .....	26
3.6 Model B description in the frame of turbulent combustion .....	30
3.7 Model B validation in 1D and 2D configurations .....	31
3.8 Model B application: analysis of the freely propagating flames for different boundary conditions in the non-linear regime .....	34
<b>4 High-fidelity LES .....</b>	<b>37</b>
4.1 Introduction .....	37
4.2 Analysis of the planar turbulent jet flame with LES .....	37
4.3 LES results of the IOB lab-scale furnace comparing $Le = 1$ and $Le \neq 1$ .....	39
4.4 LES of a turbulent jet premixed flame using Model A .....	42
4.5 LES of a turbulent jet diffusion flame using the FPVA .....	46
<b>5 RANS simulations framework .....</b>	<b>47</b>
5.1 Implementation of the tabulated-chemistry combustion model with preferential diffusion in commercial CFD software .....	47
5.1.1 Laminar configuration .....	48
5.1.2 Turbulent configuration .....	49
5.2 RANS simulations of H <sub>2</sub> -air lean premixed flame .....	50
5.2.1 Hydrogen-air lean premixed round jet flame .....	51
5.2.2 Hydrogen-air lean premixed slot jet flame .....	53

## D2.3 - Report on simulation framework for H<sub>2</sub>/O<sub>2</sub> and H<sub>2</sub>/air combustion

5.3	RANS simulations of non-premixed turbulent jet flame .....	55
<b>6</b>	<b>Publications &amp; conference participation .....</b>	<b>57</b>
<b>7</b>	<b>Bibliography .....</b>	<b>58</b>

## Tables & figures

Table	Page
Table 1. Investigated flame conditions for liftoff height measurements in diffusion flames.....	13
Table 2. Consumption speed prediction comparison for 1D simulations using different modeling approaches.....	24
Table 3. Description of the simulated cases.....	34
Table 4. Flame length and consumption speed comparison for different LES resolutions.....	39
Table 5. Transport equations of control variables for adiabatic laminar flames.....	48
Table 6. RANS transport equations of control variables for adiabatic turbulent flames.....	50

Figure	Page
Figure 1. Schematic of the burner setup with a chemiluminescence imaging system (left panel) and laser diagnostic measurement system for LIBS measurements (right panel).....	11
Figure 2. Exemplary LIBS spectrum of a CH <sub>4</sub> -air flame before (raw data) and after spectral correction showing peaks of C (I), H, O, and N.....	12
Figure 3. H <sub>if</sub> for variation of U <sub>ox</sub> in the range of 0 to 4 m/s and Re up to 14000. X <sub>H2</sub> = 0.8 and X <sub>O2</sub> = 0.21 are constant for the presented measurements.....	13
Figure 4. H <sub>if</sub> for variation of X <sub>H2</sub> in the range of 0.6 to 0.9 and Re up to 14000. U <sub>ox</sub> = 3 m/s and X <sub>O2</sub> = 0.21 are constant for the presented measurements.....	14
Figure 5. H <sub>if</sub> for variation of X <sub>O2</sub> = 0.21 – 0.3 and Re up to 14000. U <sub>ox</sub> = 3 m/s and X <sub>H2</sub> = 0.8 are constant for the presented measurements.....	14
Figure 6. Liftoff height as a function of the flame base diameter for different oxidizer coflow velocities and X <sub>H2</sub> = 0.8.....	15
Figure 7. Vertical mixture fraction profiles along the burner centerline from the burner nozzle up to the flame base for U <sub>ox</sub> = 1 m/s (left) and U <sub>ox</sub> = 3 m/s (right).....	16
Figure 8. Radial mixture fraction profiles at the height of the flame base for U <sub>ox</sub> = 1 m/s (left) and U <sub>ox</sub> = 3 m/s (right).....	16
Figure 9. a) Exemplary OH* chemiluminescence images for flame height measurements at Re = 10000, b) measured flame heights of premixed H <sub>2</sub> main flames at Re = 7000 and 10000.....	17
Figure 10. Schematic of the pilot and main flame tube setup of the jet burner before (left) and after modifications for the lift of the honeycomb (right).....	17
Figure 11. Temporal evolution (left to right) of spherically expanding lean H <sub>2</sub> and CH <sub>4</sub> flames for an unburnt gas temperature of 373 K [40,41]. The time scales strongly deviate between the two fuels, and hydrogen shows intrinsic flame instabilities for the later time.....	19
Figure 12. Left: DNS of planar premixed turbulent hydrogen/air jet flame at $\phi = 0.4$ and ambient conditions, jet Reynolds number Re = 11000. Right: Same DNS, but with the assumption of unity Lewis numbers for all species. Significant differences are visible in flame length, local wrinkling, and super-equilibrium progress-variable values CH <sub>2O</sub> reflecting locally richer conditions caused by thermodiffusive instabilities [7]......	19
Figure 13. Water source term comparison for a 1D simulation with $\phi = 0.4$ .....	24
Figure 14. Example of the initialization of the 2D laminar simulations.....	24
Figure 15. Water mass fraction field from the detailed chemistry simulation (left) and from the simulation using Model A (right). .....	25
Figure 16. Consumption speed comparison for the 2D planar flame simulations. From left to right Y <sub>O2,2</sub> = 0.23, Y <sub>O2,2</sub> = 0.3, and Y <sub>O2,2</sub> = 0.5. DC: detailed chemistry simulation, Model A: simulation using model A.....	25
Figure 17. Joint distribution of the progress variable source term and normalized progress variable. From top to bottom: Y <sub>O2,2</sub> = 0.23, Y <sub>O2,2</sub> = 0.3, and Y <sub>O2,2</sub> = 0.5. Left: detailed chemistry simulation, right: Model A. ....	26
Figure 18. Flame speed s <sub>L</sub> and thermal flame thickness l <sub>F</sub> comparison between Cantera (solid and dashed lines respectively) and Alya FGM (circle and square markers respectively) for one-dimensional adiabatic hydrogen/air flames at atmospheric pressure and unburnt gas temperature of 298.15 K. ....	31

## D2.3 - Report on simulation framework for H<sub>2</sub>/O<sub>2</sub> and H<sub>2</sub>/air combustion

Figure 19. Normalized profiles of hydrogen mass fraction, mixture fraction, temperature, and heat release for a lean, stoichiometric, and rich mixture. Results for Cantera and Alya. ....	32
Figure 20. Contour plots of heat release for the different mixing lengths. The top half corresponds to finite rate chemistry solution while the bottom half to tabulated chemistry. The blue dotted lines indicate the size of the domain in the transversal direction. All flames are centered for visualization. ....	32
Figure 21. Values of temperature, heat release, and hydroxide mass fraction vs mixture fraction along the isolines for progress variable $Y_c = 0.1$ (light blue), $0.2$ (blue), and $0.245$ (dark blue) for finite rate model (lines), and tabulated chemistry (empty markers) for flame III. ....	33
Figure 22. Values of temperature, heat release, and hydroxide mass fraction vs progress variable along the isolines for mixture fraction $Z = 0.015$ (light orange), $Z_{st} = 0.0285$ (orange), $0.06$ (dark red), and $0.12$ (black) for finite rate model (lines), and tabulated chemistry (empty markers) for flame III. ....	33
Figure 23. Comparison of the progress variable (left), mixture fraction (center left), enthalpy (center right), and temperature (right) for tabulated chemistry (left side), and finite rate chemistry (right side). ....	33
Figure 24. Results for $Y_{O_2} = 0.23$ and $T_{inlet} = 298$ K. Left panel: snapshots of the flame front for the finite rate chemistry (left) and tabulated chemistry (right). Right panel: temporal evolution for the consumption speed (left), flame surface area (center), and the reactivity ratio (right) for both models. ....	34
Figure 25. Results for $Y_{O_2} = 0.3$ and $T_{inlet} = 298$ K. Left panel: snapshots of the flame front for the finite rate chemistry (left) and tabulated chemistry (right). Right panel: temporal evolution for the consumption speed (left), flame surface area (center), and the reactivity ratio (right) for both models. ....	35
Figure 26. Results for $Y_{O_2} = 0.5$ and $T_{inlet} = 298$ K. Left panel: snapshots of the flame front for the finite rate chemistry (left) and tabulated chemistry (right). Right panel: temporal evolution for the consumption speed (left), flame surface area (center), and the reactivity ratio (right) for both models. ....	35
Figure 27. Results for $Y_{O_2} = 0.5$ and $T_{inlet} = 700$ K. Left panel: snapshots of the flame front for the finite rate chemistry (left) and tabulated chemistry (right). Right panel: temporal evolution for the consumption speed (left), flame surface area (center), and reactivity ratio (right) for both models. ....	35
Figure 28. Instantaneous snapshots of the mixture fraction (a), temperature (b), and heat release rate (c) for the DNS and the LES with resolution M4 (left and right plots of each panel respectively). ....	38
Figure 29. Temporally and spatially averaged temperature field for the DNS and the LES for the four meshes. The dashed white line corresponds to the iso-contour corresponding to a normalized temperature of $0.95$ . ....	38
Figure 30. Instantaneous temperature fields for the six considered cases for unity Lewis (top) and mixture-averaged (bottom). ....	40
Figure 31. Instantaneous mixture fraction fields for the six considered cases for unity Lewis (top) and mixture-averaged (bottom). ....	40
Figure 32. Comparison of laminar flame speeds for Lewis unity (blue) and mixture-averaged diffusion model (red). The vertical black line marks the global equivalence ratio of the LES in each case. ....	41
Figure 33. Maps of the progress variable source term ( $kg/m^3/s$ ) as a function of the mixture fraction (abscissa) and the normalized progress variable (ordinate) for $X_{CH_4} = 0.2$ and $X_{H_2} = 0.8$ . Left: $Le = 1$ , right: mixture-averaged model. ....	41
Figure 34. Temporal evolution of the flame length for $Le=1$ (blue) and mixture-averaged (red) for the cases $X_{CH_4} = 1$ (left column), $X_{CH_4} = 0.6$ , and $X_{H_2} = 0.4$ (central column) and $X_{CH_4} = 0.2$ and $X_{H_2} = 0.8$ (right column). Top row: flame length defined with the 20% of the peak heat release. Bottom row: idem with 50% of the peak heat release. ....	42
Figure 35. Instantaneous of the mixture fraction (top) and water mass fraction (bottom) contour plots. From left to right: DNS, LES with finer grid, and LES with coarser grid. ....	43
Figure 36. Averaged fields comparison. Top: Temperature. Bottom: axial velocity. From left to right: DNS, LES with finer grid and LES with coarser grid. Here the coordinates are normalized by the slot width. ....	44
Figure 37. Comparison of averaged water mass fraction (left), axial velocity (middle), and temperature (right) at different axial quotas. Here the coordinates are normalized by the slot width. ....	44
Figure 38. Normalized axial water flux for the slot burner configuration. ....	45
Figure 39. Normalized axial water flux for the round burner configuration. ....	45
Figure 40. Instantaneous progress variable contour plot of the round-jet turbulent lifted flame configuration. ....	46
Figure 41. The numerical domain of the 1D-free flame in Fluent. ....	48

## D2.3 - Report on simulation framework for H<sub>2</sub>/O<sub>2</sub> and H<sub>2</sub>/air combustion

Figure 42. Laminar flame speed and thermal flame thickness.....	49
Figure 43. Profiles of equivalence ratio, temperature, and H <sub>2</sub> mole fraction across the 1D free-flame. The position x equal to zero is located at the point of temperature rise.....	49
Figure 44. DNS instantaneous temperature and equivalence ratio for (a) the round jet flame and (b) the slot jet flame.....	50
Figure 45. Example of the numerical domain for the RANS simulations. Dimensions in mm.....	51
Figure 46. Central jet velocity profile for (a) the round jet flame and (b) the slot jet flame.....	51
Figure 47. Contours of heat release rate, hydrogen mass fraction, equivalence ratio, and temperature for the round jet flame from the DNS Favre-averaged data and the RANS data.....	52
Figure 48. Profiles of temperature, equivalence ratio, heat release rate, and axial velocity for the round jet flame DNS Favre-averaged data and the RANS data.....	52
Figure 49. Contours of heat release rate, temperature, and equivalence ratio for the round jet flame from (a) the DNS Favre-averaged data and (b) the RANS with preferential diffusion in the flamelets and transport equations, (c) the RANS with preferential diffusion only in the flamelets, and (d) the RANS with unity Lewis assumption.....	53
Figure 50. Contours of heat release rate, hydrogen mass fraction, equivalence ratio, and temperature for the slot jet flame from the DNS Favre-averaged data and the RANS data.....	54
Figure 51. Profiles of temperature, equivalence ratio, heat release rate, and axial velocity for the slot jet flame DNS Favre-averaged data and the RANS data.....	54
Figure 52. Contours of temperature and OH mole fraction for the diffusion jet flame with Re= 14000, obtained from RANS simulations comparing tabulated chemistry with Unity Lewis and preferential diffusion (FGM-PD).....	55
Figure 53. Mixture fraction profiles along the flame central axis (left column) and along the radial direction at experimental liftoff length (right column).....	56

## List of abbreviations

Abbreviations	Explanation
LIBS	Laser induced breakdown spectroscopy
LES	Large eddy simulations
RANS	Reynolds-averaged Navier-Stokes
WP	Work packages
FPVA	Flamelet progress-variable approach
PDF	Probability density function
JPDF	Joint-probability density function
TD	Thermo-diffusive
TCI	Turbulence-chemistry interaction
FGM	Flamelet generated manifold
UDF	User-defined function
CFD	Computational fluid dynamics
PD	Preferential diffusion
UDS	User-defined scalars

# 1 Introduction

This report presents the development of a hierarchical modeling framework designed to predict the effects of thermo-diffusive instabilities in turbulent H<sub>2</sub>/O<sub>2</sub> flames and H<sub>2</sub>/air flames. It serves as a summary of the activities conducted within Task 2.3 of the HyInHeat project. Thermo-diffusive instabilities are a critical challenge in hydrogen flames, significantly influencing combustion performance by increasing the risk of blow-off and flashback while also increasing pollutant emissions. Accurate predictive modeling is, therefore, essential for the design and the retrofitting of combustion systems that operate with H<sub>2</sub>.

The modeling framework developed in this task is designed for integration into full furnace simulations, including both large-eddy simulations (LES) and Reynolds-averaged Navier-Stokes (RANS) simulations, which are planned for Work Packages (WP) 5 and 6. The framework relies on the kinetic mechanisms provided in WP 1.3 for both model development and validation.

Task 2.3 is a collaborative effort involving the following partners: RWTH-ITV, RWTH-IOB, and BSC.

## 1.1 Objective and structure

Task 2.3 is divided into four distinct sub-tasks, each led by specific partners as highlighted in parentheses in the bullet points list below. This report is structured to reflect this division, with Chapters 2 to 5 dedicated to each sub-task. The final chapter provides a summary of the publications and conference presentations from the participating partners.

The key objectives of Task 2.3 and their corresponding sub-tasks are as follows:

- Provide experimental data for model validation (RWTH-ITV).
- Extend tabulated chemistry models for predictive modeling of thermo-diffusive instabilities (RWTH-ITV & BSC).
- Perform high-fidelity LES to develop and calibrate improved combustion models (RWTH-ITV & BSC).
- Incorporate the newly developed combustion models into the framework for RANS simulations suitable for industrial applications (RWTH-IOB).

## 2 Turbulent H<sub>2</sub> jet flame experiments

A turbulent round jet burner configuration was chosen to obtain experimental data on turbulent diffusion and premixed flames. The data was employed to analyze the effects of fuel composition and oxygen content in the oxidizer on selected flames as reported in Sections 2.2 and 2.3. Additionally, the experimental measurements serve as validation data for the modeling framework.

### 2.1 Description of the experimental setup and techniques

The experimental setup adopted for the WP 2 schematically shown in Figure 1, includes a concentric flow round jet burner (left panel), an OH\* chemiluminescence imaging system (left panel), and a laser diagnostic system for laser-induced breakdown spectroscopy (LIBS) (right panel).

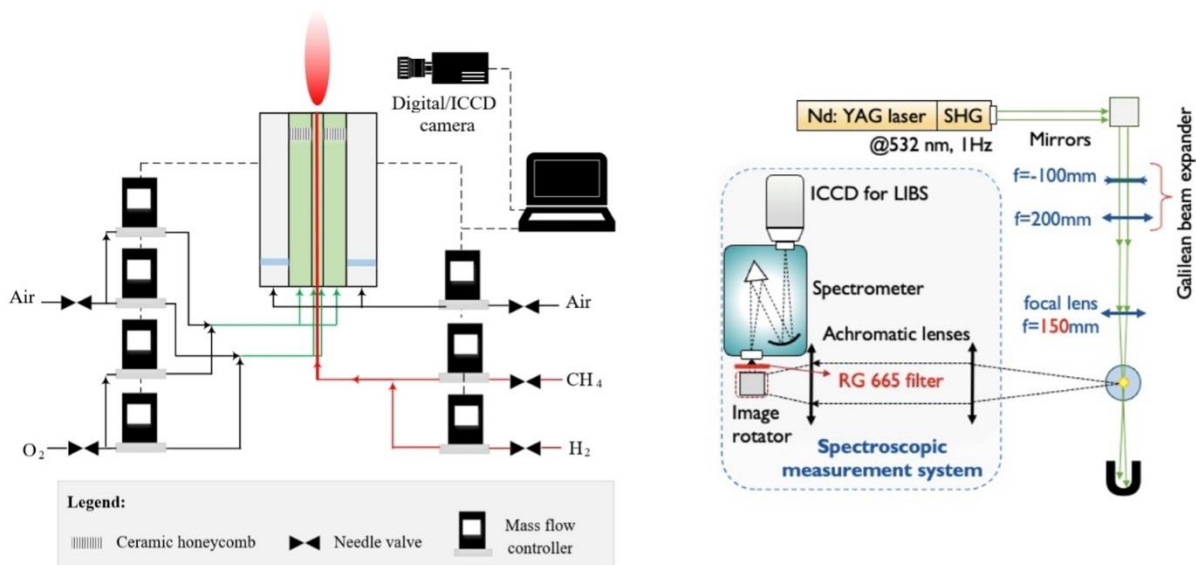


Figure 1. Schematic of the burner setup with a chemiluminescence imaging system (left panel) and laser diagnostic measurement system for LIBS measurements (right panel).

#### 2.1.1 Jet burner configuration

The jet burner consists of four concentric tubes: the fuel supply tube ( $D_{fuel,in} = 2.5$  mm), the primary oxidizer tube ( $D_{ox1,in} = 9$  mm), the premixed pilot flame or secondary oxidizer tube ( $D_{pilot,in} = D_{ox2,in} = 32$  mm) and a shielding coflow ( $D_{coflow,in} = 140$  mm). Since the vertical positioning of the fuel tube is adjustable independently from the rest of the burner, the burner can either operate in diffusion mode, with the fuel tube at the same height as other tubes, or in premixed mode, with the fuel tube lowered to allow mixing with air. In the diffusion configuration, the mass composition and outlet velocity of the secondary oxidizer were unchanged with respect to those of the primary oxidizer. On the other hand, in the premixed configuration, a premixed CH<sub>4</sub>-air pilot flame was used instead of the secondary oxidizer to stabilize the main flame. Moreover, the shielding air coflow ensures fixed boundary conditions, which are essential for improving the accuracy and reliability of the planned LES and RANS simulations.

To control the volume flow rates of the gases, mass flow controllers from Alicat (accuracy of 0.32% of the set point and 0.02% of the full scale) and Omega (accuracy of 0.5% of the set point and 0.1% of the full scale) were used. Additionally, the burner setup is mounted on a vertical and horizontal movement system, allowing accurate positioning of the burner relative to the measurement systems to enable measurements at different flame locations.

## D2.3 - Report on simulation framework for H<sub>2</sub>/O<sub>2</sub> and H<sub>2</sub>/air combustion

### 2.1.2 OH\* chemiluminescence setup

OH\* chemiluminescence was used to analyze the structure of the flames and measure quantities such as flame liftoff height, flame base diameter (for diffusion flames), and flame length (for premixed flames).

The OH\* chemiluminescence signal is obtained from the chemically excited OH\* as it transitions to the ground state, emitting radiation. Since radiation from other species is negligible at around 310 nm, a bandpass filter centered around 310 nm is used to separate the OH\* signal from the luminosity of other species. The signal is captured using an ICCD camera (Andor, iStar DH334T) with a gate width of 5 ms. To obtain mean values of the measured quantities, 200 single images with a spatial resolution of 0.036 mm were averaged for each condition.

### 2.1.3 LIBS setup

The LIBS measurement technique utilizes a pulsed laser beam from a Nd:YAG laser at 532 nm to locally excite the present element species (C, H, N, and O) to a plasma state. After the laser pulse, the excited species return to the ground state, emitting element-specific radiation. This radiation is analyzed using a spectrometer (Princeton Instruments, ISOPLANE SCT 320). The resulting spectrum, which contains signal intensities as a function of the signal wavelength is extracted. After applying a spectral correction, as seen in Figure 2, the elemental mass fractions are determined by applying a fitting procedure. This procedure employs Voigt functions to calculate the peak areas for each element. The ratios of these areas represent the elemental mass fractions, that are then used to obtain the local mixture fraction according to Bilger's definition [1].

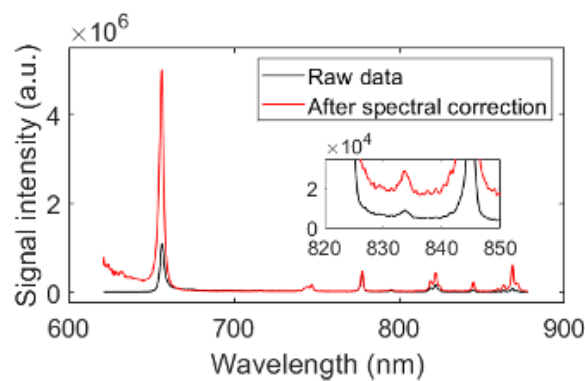


Figure 2. Exemplary LIBS spectrum of a CH<sub>4</sub>-air flame before (raw data) and after spectral correction showing peaks of C (I), H, O, and N.

To improve the signal in the turbulent flame, the resulting quantities from 500 laser pulses were averaged for each measurement point.

## 2.2 Diffusion flame measurements

The OH\* chemiluminescence measurements were conducted in the diffusion flames to investigate the influence of key operation parameters, such as the fuel Reynolds number,  $Re$ , the oxidizer coflow velocity,  $U_{ox}$ , the hydrogen content in the fuel flow,  $X_{H_2}$ , and the oxygen content of the oxidizer flow,  $X_{O_2}$  on the flame stability and the liftoff height,  $H_{lf}$ . Understanding these characteristics is essential to ensure safe and efficient operability of diffusion burner configurations while minimizing material damage due to thermal stresses. This is particularly relevant for H<sub>2</sub> and H<sub>2</sub>-enriched flames with O<sub>2</sub>-enriched oxidizers due to the high reactivity and burning velocity compared to traditional fuels like CH<sub>4</sub>. In addition to providing valuable validation data for the developed modeling framework, varying the aforementioned parameters aids in identifying stable conditions for the diffusion flames and developing strategies for controlling flame liftoff behavior.

From the OH\* chemiluminescence measurements, the  $H_{lf}$  of the investigated flames, as shown in Table 1, was determined as the axial distance between the flame front edge and the tip of the burner nozzle. The flame

## D2.3 - Report on simulation framework for H<sub>2</sub>/O<sub>2</sub> and H<sub>2</sub>/air combustion

front edge was identified under the assumption of an OH\* intensity of 10 % or more of the maximum OH\* intensity.

The effect of  $U_{ox}$  on the liftoff behavior is displayed in Figure 3, which generally results in an increase of  $H_{lf}$  with increasing  $U_{ox}$ . For low velocities ( $U_{ox} = 0$  and 1 m/s), a liftoff behavior was observed only for  $Re = 10000$  or higher, as flames remained attached for lower  $Re$  values. Under these conditions,  $H_{lf}$  increased with increasing  $Re$  values. In contrast, at higher velocities ( $U_{ox} = 3$  and 4 m/s),  $H_{lf}$  decreased as  $Re$  increased. At  $U_{ox} = 2$  m/s, a non-monotonic trend in  $H_{lf}$  with respect to a  $Re$  variation was observed. Similar shifts in the trend of  $H_{lf}$  as a function of  $Re$  were observed for variations in  $X_{H2}$  and  $X_{O2}$ , as depicted in Figure 4 and Figure 5, respectively. These trends indicate a negative correlation for  $X_{H2} < 0.9$  and  $X_{O2} < 0.25$  for the respective conditions. This dependence of  $H_{lf}$  on oxidizer coflow velocity has been documented in prior work by Brown et al. [2] and Guiberti et al. [3]. They also proposed a stabilization mechanism for turbulent lifted CH<sub>4</sub> flames, which supports the observed trends of  $H_{lf}$  as a function of  $U_{ox}$  and fuel composition.

Investigated variation	Fuel flow		Oxidizer flow	
	X <sub>H2</sub> (CH <sub>4</sub> to balance)	Re	X <sub>O2</sub>	U <sub>ox</sub>
U <sub>ox</sub>	0.8	4000 - 14000	0.21	0 - 4 m/s
X <sub>H2</sub>	0.6 - 1	4000 - 14000	0.21	3 m/s
X <sub>O2</sub>	0.8	4000 - 15000	0.21 - 0.3	3 m/s

Table 1. Investigated flame conditions for liftoff height measurements in diffusion flames.

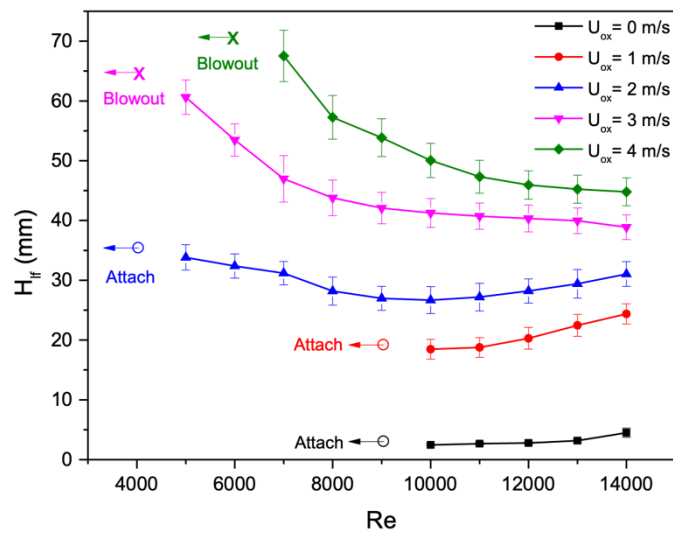


Figure 3.  $H_{lf}$  for variation of  $U_{ox}$  in the range of 0 to 4 m/s and  $Re$  up to 14000.  $X_{H2} = 0.8$  and  $X_{O2} = 0.21$  are constant for the presented measurements.

## D2.3 - Report on simulation framework for H<sub>2</sub>/O<sub>2</sub> and H<sub>2</sub>/air combustion

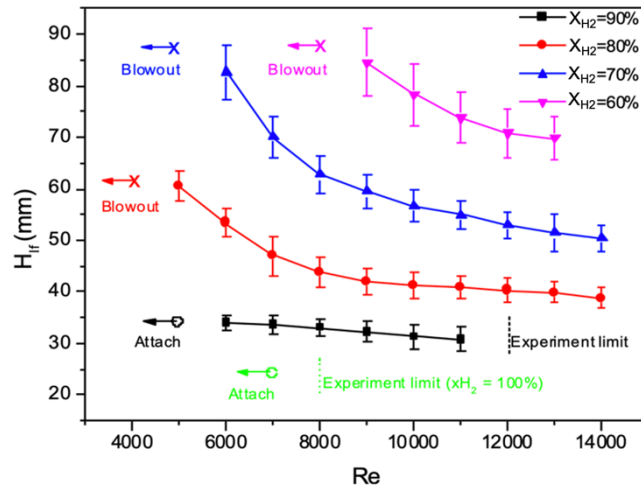


Figure 4.  $H_{lf}$  for variation of  $X_{H_2}$  in the range of 0.6 to 0.9 and  $Re$  up to 14000.  $U_{ox} = 3$  m/s and  $X_{O_2} = 0.21$  are constant for the presented measurements.

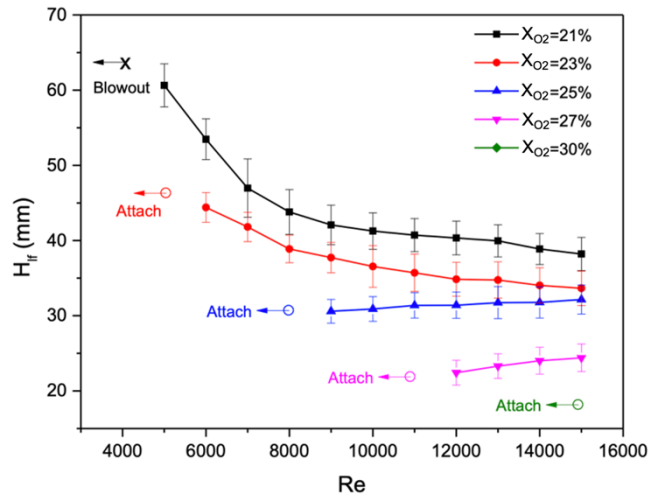


Figure 5.  $H_{lf}$  for variation of  $X_{O_2} = 0.21 - 0.3$  and  $Re$  up to 14000.  $U_{ox} = 3$  m/s and  $X_{H_2} = 0.8$  are constant for the presented measurements.

To understand the flow dynamics and the stabilization mechanism underlying the observed trends in  $H_{lf}$  variation with respect to  $Re$ , the flame base diameter,  $D_{fb}$ , was determined under specified conditions. Figure 6 shows the relationship between  $H_{lf}$  and  $D_{fb}$  for different oxidizer coflow velocities. At higher  $U_{ox}$ , the increased mixing of fuel and oxidizer expands the combustible region spatially, resulting in a larger  $D_{fb}$ . Conversely, increases in  $X_{H_2}$  and  $X_{O_2}$  are attributed to the enhancement of the reactivity and the removal of species that do not contribute to the reactivity, causing the ignitable mixture range to broaden towards lower degrees of mixing.

## D2.3 - Report on simulation framework for H<sub>2</sub>/O<sub>2</sub> and H<sub>2</sub>/air combustion

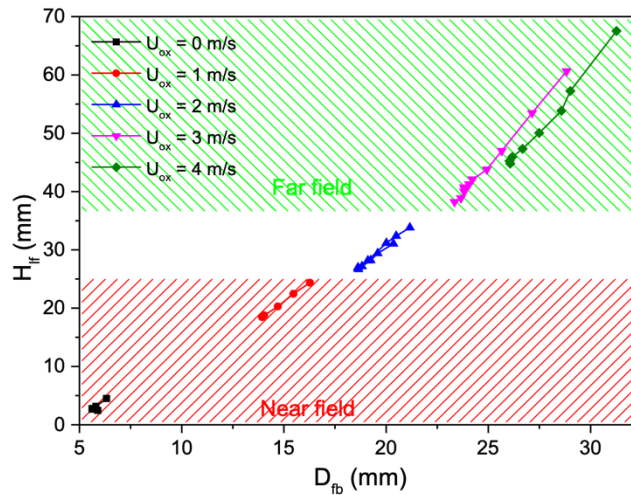


Figure 6. Lift-off height as a function of the flame base diameter for different oxidizer coflow velocities and  $X_{H_2} = 0.8$ .

Based on prior works by Cessou et al. [4] and Jeon et al. [5], the location of the flame base relative to the potential cores of the flow is a critical factor of the lift-off trend. In the following, the potential cores of the fuel flow and the oxidizer coflow are referred to as the inner and outer potential cores, respectively. Since in this work high coflow velocities were set, the initial flow region does not solely depend on the inner potential core with the core length  $L_{p,in}$ , but also on the outer potential core with the core length  $L_{p,out}$  if the magnitude rises above a certain threshold. For the cases of low  $U_{ox}$ , which result in a low  $L_{p,out}$ , and  $H_{lf}$  below  $L_{p,out}$ , the burning velocity at the leading edge is in the order of the laminar flame speed  $S_L$ . This conditional range is referred to as "near-field". Depending on the velocity field of the fuel flow, the flame will stabilize at a point where the local flow velocity equals  $S_L$  as soon as an ignitable mixture is present. Increasing  $Re$  will, therefore, shift the stabilizing point further away from the burner nozzle. For the cases of flame stabilization above the potential core, however, the burning velocity is in the order of the turbulent flame speed  $S_T$ , following studies of Guiberti et al. [3] and Brown et al. [2]. Increasing  $Re$  in these cases will further increase  $S_T$ , leading to a stabilization of the flame closer to the burner nozzle, causing a negative slope of  $H_{lf}$  as a function of  $Re$ .

For a few selected conditions with  $X_{H_2} = 0.8$  and  $U_{ox} = 1$  and 3 m/s, depicted in Figure 7, LIBS measurements were performed axially in the vicinity of the flame base. For all the investigated conditions, the value of the mixture fraction  $Z$  decreases with increasing  $H_{lf}$ , indicating higher entrainment of air into the central axis of the flow. This behavior is observed regardless of the  $H_{lf}$  trend. However, the radial  $Z$ -profiles at the flame base show larger differences in the slope of the decreasing  $Z$ . In summary, in the far field at higher  $U_{ox}$ , the decline in  $Z$  is low compared to the increase of the local flame speed, resulting in a shift of the leading edge toward the burner nozzle. In contrast, for lower  $U_{ox}$  in the near field, the drop of  $Z$  is steeper with respect to the distance from the centerline of the burner. This results in a greater decrease in the local flame speed compared to the far-field case, which is not balanced by enhanced mixing for higher  $Re$ .

## D2.3 - Report on simulation framework for H<sub>2</sub>/O<sub>2</sub> and H<sub>2</sub>/air combustion

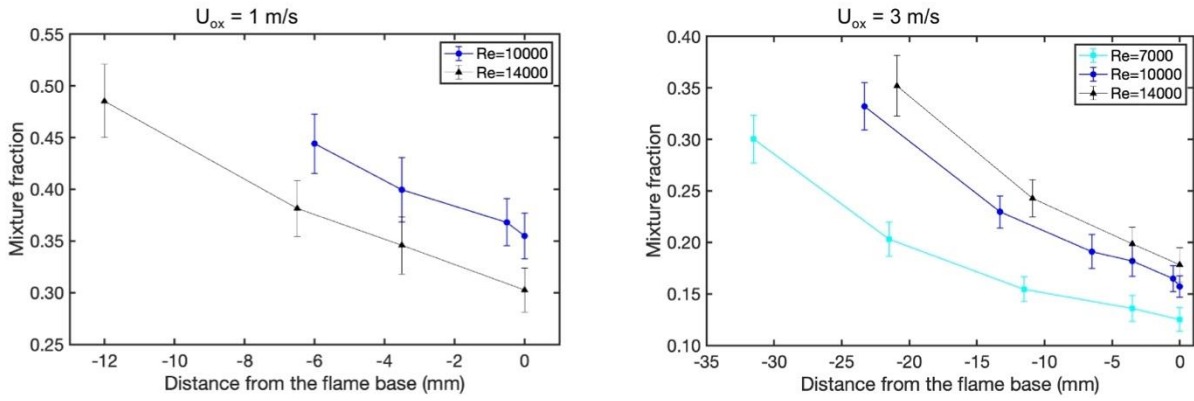


Figure 7. Vertical mixture fraction profiles along the burner centerline from the burner nozzle up to the flame base for  $U_{ox} = 1$  m/s (left) and  $U_{ox} = 3$  m/s (right).

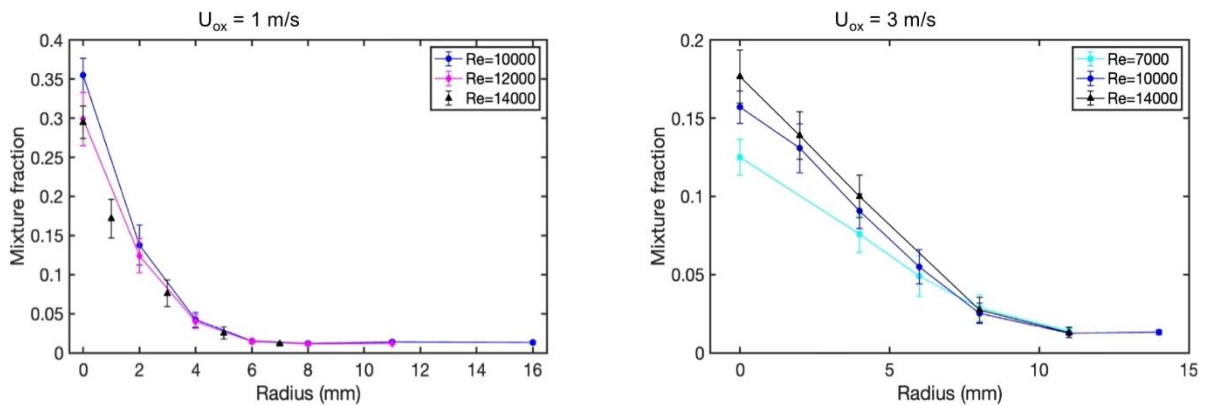


Figure 8. Radial mixture fraction profiles at the height of the flame base for  $U_{ox} = 1$  m/s (left) and  $U_{ox} = 3$  m/s (right).

## 2.3 Premixed flame measurements

To evaluate the influence of O<sub>2</sub> content in the oxidizer stream of premixed H<sub>2</sub> flames, OH\* chemiluminescence images were captured. The equivalence ratio  $\phi$  was set to 0.4 and a pilot flame fueled by a CH<sub>4</sub> with  $\phi = 0.8$  was used for stabilization. For  $Re = 7000$  and  $10000$ , three oxidizer contents in the oxidizer stream of  $X_{O_2} = 0.21, 0.25,$  and  $0.30$  were tested.

Figure 9(a) displays OH\* chemiluminescence images at  $Re = 10000$ , qualitatively indicating a linear decrease in the flame heights at the increase of  $X_{O_2}$ . Figure 9(b) illustrates quantitatively the flame height decrease with increasing  $X_{O_2}$ . The reasons for this trend are twofold. First, increasing the oxygen content reduces the concentration of the inert N<sub>2</sub> species, which in turn increases the flame temperature since the heat losses to the N<sub>2</sub> are reduced. Second, increasing  $X_{O_2}$  up to 0.3 while keeping  $\phi$  constant results in a higher total mass fraction of H<sub>2</sub>. This enhances the flame speed, thereby reducing the flame height.

## D2.3 - Report on simulation framework for H<sub>2</sub>/O<sub>2</sub> and H<sub>2</sub>/air combustion

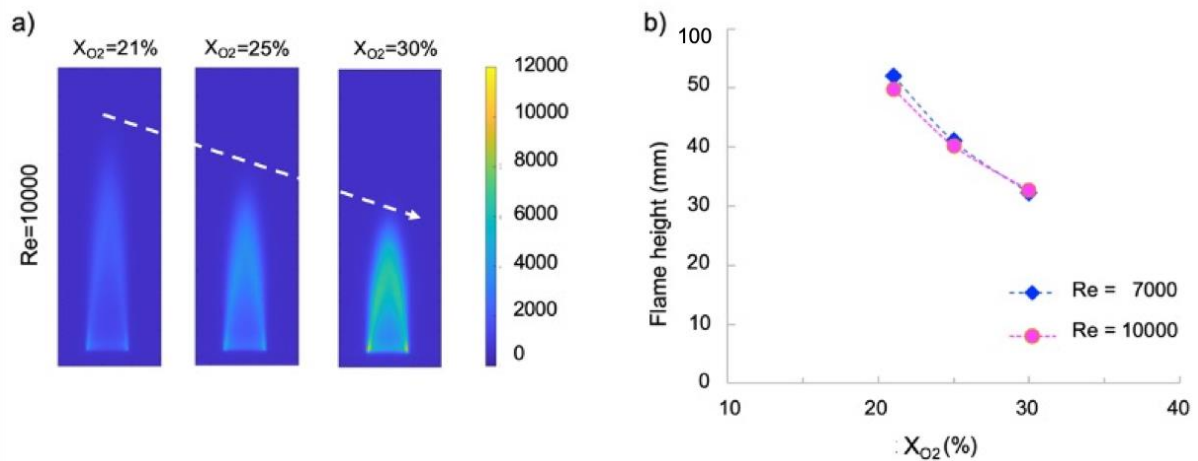


Figure 9. a) Exemplary OH\* chemiluminescence images for flame height measurements at  $Re = 10000$ , b) measured flame heights of premixed H<sub>2</sub> main flames at  $Re = 7000$  and  $10000$ .

With the current setup, a further increase of  $X_{O_2}$  led to flashbacks even in cases where the  $Re$  number was set at the upper limit of the test bench. To address this issue, a critical evaluation and optimization of the burner setup were conducted. The honeycomb structure of the pilot flame, previously located 7mm below the upper edge of the main flame tube, was likely preheating the main nozzle. To reduce this effect, a modification of the burner configuration was realized by raising the honeycomb structure, as shown in Figure 10. Although these modifications required time for evaluation, a detailed characterization of the selected premixed flames using LIBS is ongoing and will be addressed in future investigations.

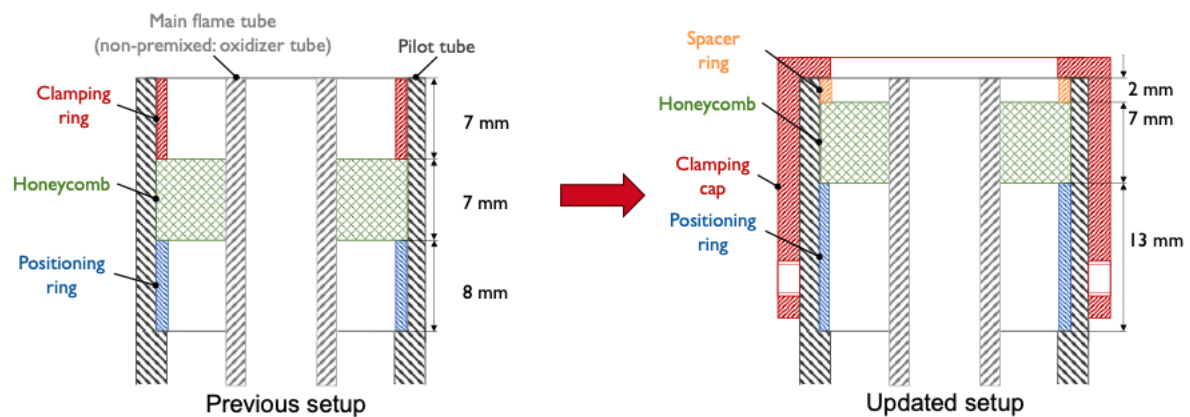


Figure 10. Schematic of the pilot and main flame tube setup of the jet burner before (left) and after modifications for the lift of the honeycomb (right).

### 3 Tabulated models for thermo-diffusive instabilities

This chapter provides a summary of the activities carried out within the second sub-task of WP2.3, focusing on developing and extending available reduced-order tabulated chemistry combustion models for predicting the effects of thermo-diffusive (TD) instabilities. The activities under this sub-task were jointly conducted by RWTH-ITV and BSC.

As part of this effort, two newly developed tabulated chemistry combustion models were designed and tested to accurately account for the dual interaction of TD instabilities and turbulence in hydrogen-premixed combustion, which is critical to ensure reliable investigations of hydrogen-fuel-based combustion systems.

The chapter is structured as follows:

1. An introduction and a comprehensive literature review of TD instabilities, including an overview of existing tabulated chemistry models.
2. A detailed description and validation of the model developed by RWTH-ITV (Model A).
3. An illustration of the model developed by BSC (Model B), along with its validation process.

#### 3.1 Introduction

The use of hydrogen as a fuel presents a promising pathway for decarbonizing thermochemical energy conversion processes. However, existing combustion devices require significant adjustments to operate efficiently and safely with hydrogen. The design and retrofitting of hydrogen-compatible combustion systems rely heavily on high-fidelity reactive flow simulations. Given the inherent high computational cost of performing such numerical simulations of turbulent reacting flows, particularly when including detailed chemical and transport processes, there is a need for the development of reduced-order models.

Hydrogen's unique combustion properties present several challenges. Unlike traditional fuels, hydrogen exhibits different physical, thermodynamic, and combustion characteristics. One key property is its low molecular weight, which results in a much higher molecular diffusivity compared to most other species and that of thermal energy. This difference can be expressed using the Lewis number  $Le_i = \lambda / (\rho c_p D_i)$  where  $\lambda$  is the heat conductivity,  $c_p$  the heat capacity at constant pressure,  $\rho$  the density, and  $D_i$  the mixture-averaged diffusivity of species  $i$ . For hydrogen, the Lewis number is approximately 0.3, about three times lower than that of methane [6].

This leads to an imbalance in the species' mass fluxes and thermal energy fluxes, referred to as differential diffusion, and also to an imbalance between the hydrogen mass flux and the other species' mass fluxes, commonly known as preferential diffusion. Preferential and differential diffusion effects can either stabilize an initial flame perturbation or lead to the occurrence of the so-called TD instabilities, which can increase the consumption speeds of hydrogen flames significantly. For instance, if one considers an initially flat hydrogen flame with small perturbations, in the zones convex towards the unburnt gases (leading points on the flame front), the focusing flux of the hydrogen's chemical energy is faster than heat loss towards unburnt gases. This leads to a local temperature increase, resulting in a higher flame speed. Conversely, in the zones convex towards the burnt gases (trailing points on the flame front), the defocusing flux of the hydrogen's chemical energy is faster than the focusing heat flux leading to a reduction of the flame speed. As a result, an initial perturbation will grow and can destabilize the flame [6].

The technical significance of these intrinsic flame instabilities cannot be overstated, as they strongly influence turbulent burning velocities. This is illustrated in Figure 11, which compares the temporal evolution of spherical hydrogen and methane flames under similar thermodynamic conditions. As shown, it takes approximately five times longer for a methane/air flame to reach the same radius as a leaner hydrogen/air flame with the same unstretched laminar flame speed.

## D2.3 - Report on simulation framework for H<sub>2</sub>/O<sub>2</sub> and H<sub>2</sub>/air combustion

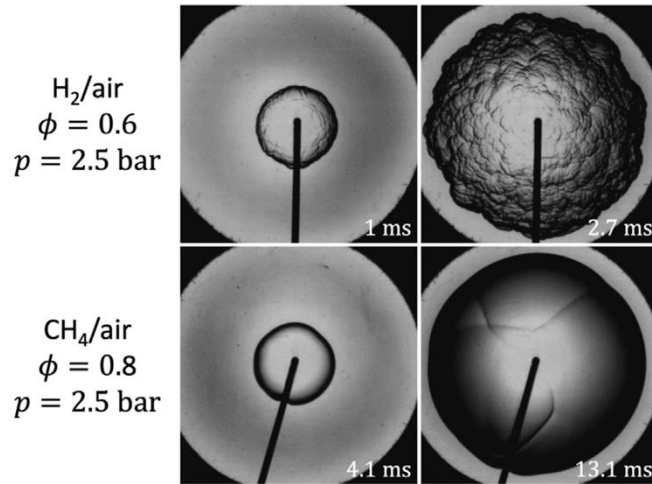


Figure 11. Temporal evolution (left to right) of spherically expanding lean H<sub>2</sub> and CH<sub>4</sub> flames for an unburnt gas temperature of 373 K [40,41]. The time scales strongly deviate between the two fuels, and hydrogen shows intrinsic flame instabilities for the later time.

In contrast to traditional fuels, molecular transport plays a significant role in the turbulent combustion of hydrogen flames due to the amplification of TD instabilities effects, which is often considered negligible for traditional fuels, as the rate of mixing is dominated by turbulent advection. As reported by Berger et al. [7], the overall consumption speed of hydrogen flames is about three times faster compared to the same flame where the effects of TD instabilities have been artificially suppressed, as shown in Figure 12. This 300% increase in turbulent flame speed caused by the TD instabilities is probably unexpected but is particularly relevant for technical applications. Furthermore, due to TD instabilities, regions with super-adiabatic temperatures—reaching up to 1820 K compared to an adiabatic temperature of 1420 K—appear in positive-curvature regions.

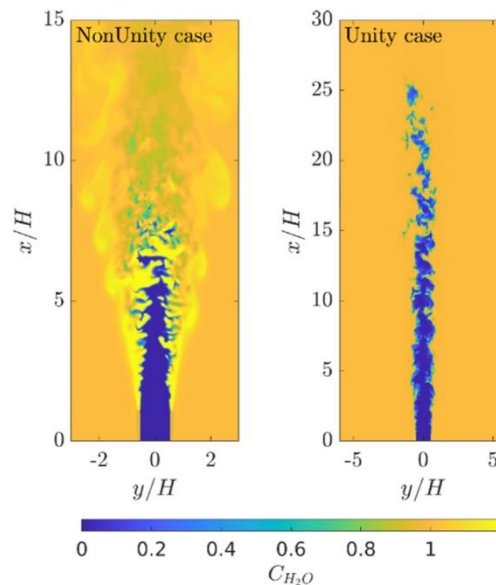


Figure 12. Left: DNS of planar premixed turbulent hydrogen/air jet flame at  $\phi = 0.4$  and ambient conditions, jet Reynolds number  $Re = 11000$ . Right: Same DNS, but with the assumption of unity Lewis numbers for all species. Significant differences are visible in flame length, local wrinkling, and super-equilibrium progress-variable values  $C_{H_2O}$  reflecting locally richer conditions caused by thermodiffusive instabilities [7].

When simulating combustion in complex systems, it is often unfeasible to resolve all flow scales. Instead, reduced-order approximations based on averaged or filtered transport equations are employed, typically

## D2.3 - Report on simulation framework for H<sub>2</sub>/O<sub>2</sub> and H<sub>2</sub>/air combustion

within the framework of either RANS simulations or LES, respectively. This allows solving only the mean values of the quantities in the RANS framework, or the fluctuations associated with the larger and intermediate scales in LES. However, this reduced information comes at the price of modeling the unclosed terms appearing in both LES and RANS equations. This challenge becomes particularly intricate when tackling the modeling of TD instabilities, primarily due to three key reasons:

- TD instabilities exhibit a highly complex and non-linear nature.
- TD instabilities can interact in a synergistic way with turbulence.
- TD instabilities originate from small scales and yet affect scales at different ranges in space and time.

It is important to note that turbulence is not the only phenomenon occurring on a subgrid-scale when dealing with TD instabilities. A certain amount of subgrid-scale wrinkling has to be expected as the characteristic dimension of small-scale structures of hydrogen/air flames due to TD instabilities falls below the computational RANS/LES grid resolution. In addition, molecular transport, which is the leading cause of TD instabilities, is typically not resolved on the computational grid employed by such reduced approaches. These two aspects pose an additional challenge when dealing with the modeling of TD instabilities.

### 3.2 LES combustion model for preferential diffusion

The standard LES tabulated modeling approach for premixed flames, such as the flamelet generated manifolds (FGM) [8] consists of solving a transport equation for an appropriately defined progress variable  $C$ , which is used to represent the entire flame state.

The combustion of fuels with close to unity Lewis number has been successfully modeled using a progress variable  $C$  based on temperature, reactants and product mass fractions, or their combination [9]. The transport equation for the progress variable is usually expressed as:

$$\frac{\partial(\rho C)}{\partial t} + \nabla \cdot (\rho \mathbf{u} C) = \nabla \cdot (\rho D_c \nabla C) + \dot{\omega}_c,$$

where  $D_c$  and  $\dot{\omega}_c$  are the progress variable diffusion coefficient and source term, respectively, and  $\rho$  is the density. A flamelet database is generated before the actual simulation by solving one-dimensional flamelets with detailed chemistry and transport. The flamelet table is then built using the progress variable  $C$  as a control variable and used to compute  $D_c$  and  $\dot{\omega}_c$ .

However, when dealing with TD instabilities, relying on a single parameter for chemistry tabulation is not sufficient. To adequately capture preferential diffusion effects (flame stretch, curvature effects, and local equivalence ratio fluctuations), multiple parameters are required [10, 11, 12]. Additionally, the chemistry tabulation must be chosen in a way that it can uniquely represent all chemical states and includes non-unity Lewis number effects.

One of the earliest efforts to account for differential diffusion effects and thermo-diffusive (TD) instabilities in premixed hydrogen flames is due to Bastiaans et al. [13], who introduced transport equations for temperature and hydrogen-based progress variables. Donini et al. [14] incorporated differential and preferential diffusion effects into the FGM model by adding extra terms to the transport equations for progress variable, enthalpy, and mixture fraction. Their approach relied on the assumption that the gradients of the progress variable were significantly larger than those of other control variables. When applied to laminar stratified methane/air flames, where differential diffusion effects are relatively weak, the model demonstrated good agreement with detailed chemistry simulations. Later, Mukundakumar et al. [15] extended Donini's method by relaxing the assumption about the dominance of progress variable gradients.

Regele et al. [16] employed some simplifying assumptions, such as the one-step irreversible chemical reaction and the unity Lewis numbers for all species except the fuel, and derived the following transport equation for the mixture fraction  $Z$ :

## D2.3 - Report on simulation framework for H<sub>2</sub>/O<sub>2</sub> and H<sub>2</sub>/air combustion

$$\frac{\partial(\rho Z)}{\partial t} + \nabla \cdot (\rho \mathbf{u} Z) = \nabla \cdot (\rho D_Z \nabla C) - \nabla \cdot (\rho D_Z^* \nabla C).$$

As a result of the differential diffusion effect, the mixture fraction is no longer a conserved scalar, and the corresponding transport equation includes a non-standard diffusion coefficient  $D_Z$ . The inclusion of a source term in the mixture fraction equation ( $-\nabla \cdot (\rho D_Z^* \nabla C)$ ) effectively emulates equivalence ratio fluctuations due to preferential diffusion.

The notable advantage of this method is that only the progress variable source term requires modeling, as the mixture fraction source term is in a closed form. The flame state is then tabulated using the progress variable and the mixture fraction as  $\Psi = \Psi(C, Z)$ , with  $\Psi$  being a generic thermochemical variable.

The two transport equations for  $C$  and  $Z$  coupled with flamelet tables built using a set of 1D premixed unstretched flames with different overall equivalence ratios have proven to be effective in modeling laminar lean hydrogen-air flames [16]. In particular, not only global quantities such as burning velocity, flame thickness, and mixture fraction variation were correctly recovered, but also stable and unstable multidimensional flame propagation was properly predicted.

The model developed by Regele et al. was later extended by Schlup and coauthors [17] to also incorporate thermal diffusion, known as the Soret effect, and varying Lewis number effects. This extension resulted in a slightly different transport equation for mixture fraction with an additional term, which accounts for the Soret effect, and different definitions of the diffusion coefficients,  $D_Z$  and  $D_Z^*$ . However, the procedure for generating the flamelet tables remained mostly unchanged. The one-dimensional unstretched flames were generated using a mixture-averaged diffusion model and the Soret effect was accounted for. The extended model demonstrated higher accuracy in predicting laminar flame speed in 1D cylindrical-propagating flame configuration, highlighting the importance of thermal diffusion and preferential diffusion effects in curved propagating flame front.

Recently, Berger et al. [18] investigated in a systematic way the optimal number of parameters to be used to map the progress variable source term in a lean premixed turbulent hydrogen flame. For an accurate parametrization of the progress variable source term, at least three parameters need to be used.

In contrast to premixed flames, TD instabilities have a reduced impact on diffusion flames. As will be shown in Section 4.5, standard LES tabulated models for diffusion flames like the flamelet progress-variable approach (FPVA) [19] succeed in accurately predicting the most important combustion quantities.

### 3.3 Model A description

Model A has been developed by RWTH-ITV and extends the existing approach mainly based on Schlup et al. [17] and recently investigated by Berger [12]. This includes the interaction between turbulence and thermo-diffusive instabilities in premixed flame configurations.

The newly developed model consists of a flamelet database generated by solving one-dimensional unstretched flames with varying equivalence ratios and with detailed chemistry and transport, thereby accounting for flame structure. The model is coupled with two scalar transport equations for the progress variable and the mixture fraction. As previously discussed, due to TD instabilities, the mixture fraction is no longer a conserved scalar, and the corresponding transport equation incorporates a modified diffusion coefficient. This model is currently implemented in RWTH-ITV's in-house software, CIAO, and BSC's in-house software, Alya.

The tables are built using the optimal set of parameters identified by Berger et al. [7] *i.e.*, the Favre-filtered (introduced in Eq. 1) mixture fraction  $\tilde{Z}$ , the progress variable  $\tilde{C}$ , and the subgrid progress variable variance  $\tilde{C}''^2$ . While the progress variable can be defined based on either the hydrogen or water mass fractions, the water mass fraction,  $Y_{H_2O}$ , is preferred here due to its ability to better capture super-adiabatic zones [12]. The two transport equations for the progress variable  $\tilde{C}$  and the mixture fraction  $\tilde{Z}$  reads:

### D2.3 - Report on simulation framework for H<sub>2</sub>/O<sub>2</sub> and H<sub>2</sub>/air combustion

$$\frac{\partial(\bar{\rho}\tilde{C})}{\partial t} + \nabla \cdot (\bar{\rho}\tilde{\mathbf{u}}\tilde{C}) = \nabla \cdot (\bar{\rho}\tilde{D}_c\nabla\tilde{C}) + \nabla \cdot \left( \bar{\rho}\tilde{D}_c^T \frac{\nabla\tilde{T}}{\tilde{T}} \right) + \bar{\omega}_c + \nabla \cdot \mathbf{q}_c,$$

$$\frac{\partial(\bar{\rho}\tilde{Z})}{\partial t} + \nabla \cdot (\bar{\rho}\tilde{\mathbf{u}}\tilde{Z}) = \nabla \cdot (\bar{\rho}\tilde{D}_Z\nabla\tilde{Z}) + \nabla \cdot \left( \bar{\rho}\tilde{D}_Z^T \frac{\nabla\tilde{T}}{\tilde{T}} \right) - \nabla \cdot (\bar{\rho}\tilde{D}_Z^*\nabla\tilde{C}) + \nabla \cdot \mathbf{q}_Z,$$

where  $D_c$  and  $D_c^T$  are the water mass diffusion coefficient and thermal diffusion coefficient respectively,  $\omega_c$  is the water source term, and  $D_Z$ ,  $D_Z^T$  and  $D_Z^*$  are defined as follows:

$$D_Z = \frac{\nu D_{H_2} + Y_{O_2,ox} D_{O_2}}{\nu + Y_{O_2,ox}},$$

$$D_Z^* = \left( \frac{\nu}{\nu + 1} \right) \left( \frac{D_{H_2} - D_{O_2}}{\nu + Y_{O_2,ox}} \right),$$

$$D_Z^T = \left( \frac{1}{\rho T} \right) \left( \frac{\nu D_{H_2}^T - D_{O_2}^T}{\nu + Y_{O_2,ox}} \right).$$

Here  $Y_{O_2,ox}$  is the oxygen mass fraction in the oxidizer,  $\nu$  is the stoichiometric oxidizer-to-fuel ratio, and  $D_i$  and  $D_i^T$  are the mass diffusion coefficient and thermal diffusion coefficient of species  $i$  respectively.

The two equations represent the filtered version of the transport equations derived from Schlup et al [17]. To ensure that the filtering process does not alter the form of the conservation equations, the Favre (density-weighted) average has been used. The Favre average is denoted by a tilde symbol and is defined as:

$$\tilde{\phi} = \frac{\overline{\rho\phi}}{\bar{\rho}}, \quad (1)$$

with  $\phi$  being a generic quantity and the overbar indicating the grid-filtering operation. The terms  $\mathbf{q}_k$  represent the residual flux  $\nabla \cdot (\bar{\rho}\tilde{\mathbf{u}}\tilde{\phi}_k - \bar{\rho}\tilde{\mathbf{u}}\tilde{\phi}_k)$  of the scalar  $\phi_k$  and are modeled using the dynamic approach of Moin et al. [20].

The subgrid progress variable variance  $\tilde{C}^{\prime\prime 2}$  is computed using the algebraic model from Pierce and Moin [21]:

$$\tilde{C}^{\prime\prime 2} = K_c \Delta^2 |\nabla\tilde{C}|^2,$$

where the coefficient  $K_c$  is evaluated using a dynamic approach, similar to the one employed for scalar flux, and  $\Delta$  is the grid filter width.

To account for turbulence, a presumed probability density function (PDF) approach is used for the progress variable source term, such as

$$\bar{\omega}_c = \int P(\tilde{C}, \tilde{Z}) \cdot \omega_c(\tilde{C}, \tilde{Z}) d\tilde{C} d\tilde{Z}.$$

As  $\tilde{C}$  and  $\tilde{Z}$  are not independent, a flamelet index  $\phi^{FL}$  defined as the global equivalence for each unstretched flamelet is used in place of the filtered mixture fraction. Assuming a  $\beta$ -PDF for the filtered progress variable and a  $\delta$ -PDF for the flamelet index, the combined PDF of the source term reads:

$$P(C, \phi^{FL}) = \beta(C; \tilde{C}, \tilde{C}^{\prime\prime 2}) \delta(\phi^{FL} - \tilde{\phi}^{FL}),$$

leading to:

$$\bar{\omega}_c = \int \beta(C; \tilde{C}, \tilde{C}^{\prime\prime 2}) \cdot \omega_c(\tilde{C}, \tilde{\phi}^{FL}) dC.$$

The filtered source term can now be computed for each flamelet and different values of  $\tilde{C}$  and  $\tilde{C}^{\prime\prime 2}$ . Using the following relation to compute the filtered mixture fraction:

## D2.3 - Report on simulation framework for H<sub>2</sub>/O<sub>2</sub> and H<sub>2</sub>/air combustion

$$\tilde{Z} = \int \beta(c; \tilde{c}, \tilde{c}''^2) \cdot Z(\tilde{c}, \tilde{\phi}^{FL}) dC,$$

the filtered source term can now be tabulated as a function of  $\tilde{Z}$ ,  $\tilde{c}$ , and  $\tilde{c}''^2$ .

The same procedure is also applied to the mass diffusion coefficients, the thermal diffusion coefficients, the viscosity coefficients, the density, and the temperature values in a way that the entire chemical state is mapped as a function of the three optimal parameters  $\tilde{Z}$ ,  $\tilde{c}$ , and  $\tilde{c}''^2$ .

### 3.4 Model A validation

To validate and evaluate the performance of Model A, a comprehensive simulation framework was established. This framework includes a series of detailed chemistry simulations of varying complexity, serving as reference data for model validation, in conjunction with experimental results outlined in Chapter 2. All the detailed chemistry simulations in this framework employ the newly developed kinetic mechanism from WP 1.4. The simulation database includes H<sub>2</sub>/air flames and H<sub>2</sub> flames in oxygen-enriched conditions with the following test cases:

- 1D unstretched flames
- 2D planar laminar flames
- 3D turbulent jet flames

This section discusses only laminar simulations, while the description of turbulent simulations is reported in Chapter 4. Moreover, the majority of the simulations target lean premixed flames, as these conditions are expected to exhibit pronounced effects of TD instabilities. The framework includes only one simulation of H<sub>2</sub> diffusion flames, in 3D turbulent jet configuration, which is discussed alongside other turbulent simulations in Chapter 4.

Model performance is quantified using key combustion metrics, such as consumption speed, flame length, and average temperature fields. Overall, Model A demonstrates good agreement with the corresponding predictions from detailed chemistry simulations across these metrics.

The first subset of simulations consists of 1D unstretched premixed flames with varying equivalence ratios ( $\phi \in [0.4, 0.6, 0.8, 1.0]$ ) and four oxidizer compositions ( $Y_{O_2,2} \in [0.21, 0.3, 0.5, 0.8]$ ), as shown in Table 2. The simulations were performed using RWTH-ITV's in-house software, CIAO. To adequately resolve the flame structure, the grid resolution was chosen to include at least 10 points within the flame zone.

Figure 13 compares the water source term as a function of the progress variable derived from three sources: a detailed chemistry simulation run with CIAO (CIAO-DC), the FlameMaster software used to generate the flamelet table (FlameMaster) [22], and Model A (CIAO-Model A). The results presented in Figure 13 correspond to the 1D flame with an equivalence ratio of 0.4 and  $Y_{O_2,2} = 0.21$ . However, similar trends are observed across different equivalence ratios and oxidizer compositions. The comparison reveals no discernible differences in the water source term, demonstrating the model's ability to correctly predict 1D flame features.

## D2.3 - Report on simulation framework for H<sub>2</sub>/O<sub>2</sub> and H<sub>2</sub>/air combustion

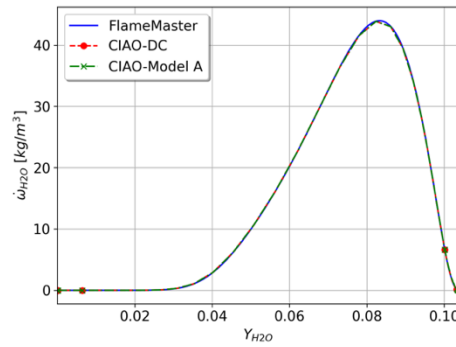


Figure 13. Water source term comparison for a 1D simulation with  $\phi = 0.4$ .

One of the key parameters to assess the model's performance is the consumption speed, defined as follows [23]:

$$s_c = \frac{1}{\rho_u Y_{H_2O,b}} \int_L \dot{\omega}_{H_2O} dx,$$

where  $\rho_u$  is the density of the unburned gases,  $Y_{H_2O,b}$  the water mass fraction in the burned gases, and  $L$  the length of the computational domain. Table 2 compares the consumption speed predictions from Model A with those obtained from detailed chemistry simulations under all tested conditions. The predictions from Model A remain within a 3% error margin for all cases, demonstrating excellent accuracy.

$\phi$	$Y_{O_2,2}$	$s_c$ FlameMaster [cm/s]	$s_c$ Model A [cm/s]
0.4	0.21	18.89	18.86
0.6	0.21	83.82	86.53
0.8	0.21	169.21	168.69
1.0	0.21	246.01	238.43
0.4	0.30	59.53	61.61
0.4	0.50	230.55	233.88
0.4	0.80	541.88	545.05

Table 2. Consumption speed prediction comparison for 1D simulations using different modeling approaches.

The second set of simulations involves 2D planar premixed flames. The flame layer is initialized using a sum of harmonic perturbations to induce the development of TD instabilities, as illustrated in Figure 14. The equivalence ratio  $\phi$  is set to 0.4 and three oxidizer compositions ( $Y_{O_2,2} = 0.21, 0.3, \text{ and } 0.5$ ) are considered.

Following the recommendations of Berger et al. [24], the domain size length was set to 100 times the laminar flame thickness to ensure that the consumption speed is not affected by the domain size and to avoid constraining the large-scale flame front corrugations. The flame zone was resolved with ten grid points per laminar flame thickness. The unburned mixture enters the domain from the left at ambient pressure and temperature and exits from the right, with periodic boundary conditions applied in the transverse ( $y$ ) direction.

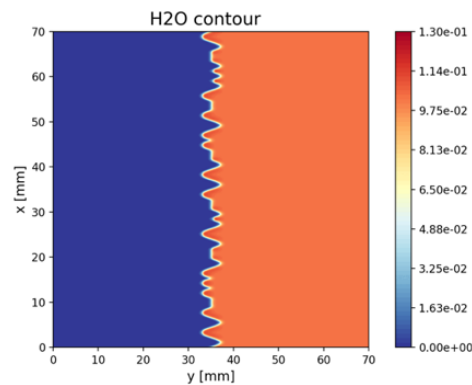


Figure 14. Example of the initialization of the 2D laminar simulations.

## D2.3 - Report on simulation framework for H<sub>2</sub>/O<sub>2</sub> and H<sub>2</sub>/air combustion

A snapshot of the progress variable field from the detailed chemistry simulation for  $\phi = 0.4$  and air as oxidizer is compared with the corresponding field from the simulation using Model A in Figure 15.

As shown in Figure 15, Model A successfully captures the formation and complex dynamics of the cellular structures that characterize TD instabilities. Furthermore, the figure highlights super-adiabatic zones, which are a characteristic indicator of TD instabilities. Just behind the flame front, the water mass fraction peaks at 0.13, significantly higher than the burned water mass fraction ( $Y_{O_2,b} = 0.10$  in this case). Despite the complexity, Model A accurately predicts the location and the size of these super-adiabatic zones.

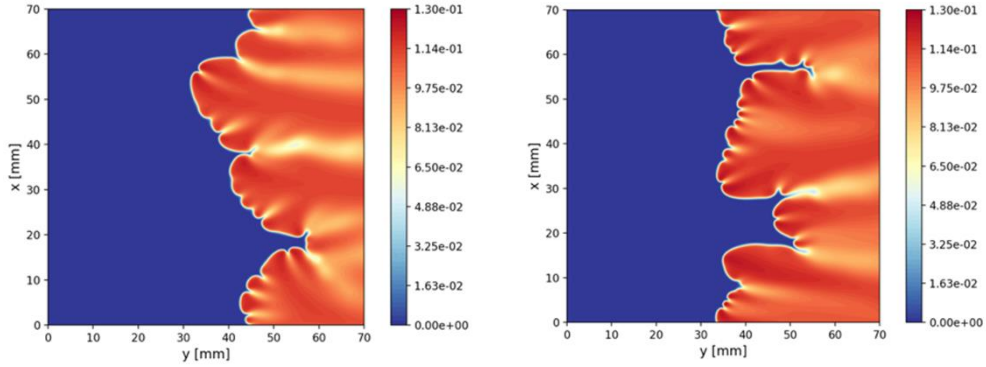


Figure 15. Water mass fraction field from the detailed chemistry simulation (left) and from the simulation using Model A (right).

A more qualitative evaluation of the model performances is given by comparing the consumption speed computed as,

$$s_c = \frac{1}{\rho_u Y_{H_2O,b} L} \int_A \dot{\omega}_{H_2O} dA,$$

where  $A$  is the surface of the computational domain and  $L$  the length of the inlet section. The time evolution of the consumption speed for different oxidizer compositions is shown in Figure 16. The time has been scaled using the flow-through time  $\tau = L/u_{in}$  where  $u_{in}$  is the inlet velocity.

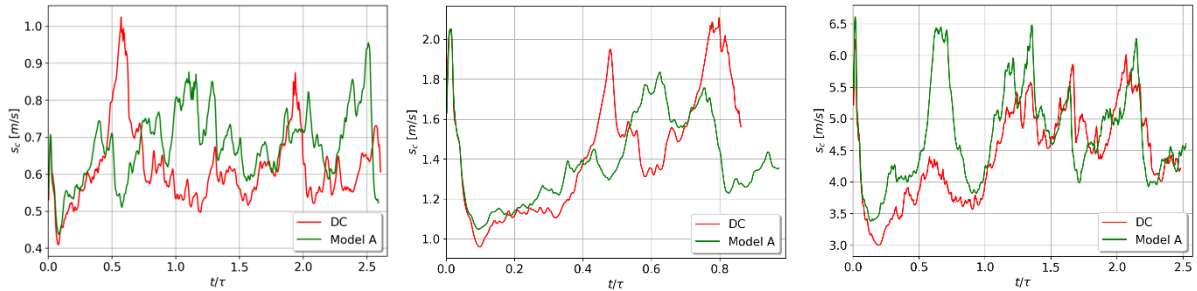


Figure 16. Consumption speed comparison for the 2D planar flame simulations. From left to right  $Y_{O_2,2} = 0.23$ ,  $Y_{O_2,2} = 0.3$ , and  $Y_{O_2,2} = 0.5$ . DC: detailed chemistry simulation, Model A: simulation using model A.

Additionally, the joint PDF (jPDF) distributions of the progress variable source term and the normalized progress variable provide further insights into the model's behavior. The joint distributions for the same different oxidizer compositions are presented in Figure 17 where the green lines represent the conditional average of the water source term.

## D2.3 - Report on simulation framework for H<sub>2</sub>/O<sub>2</sub> and H<sub>2</sub>/air combustion

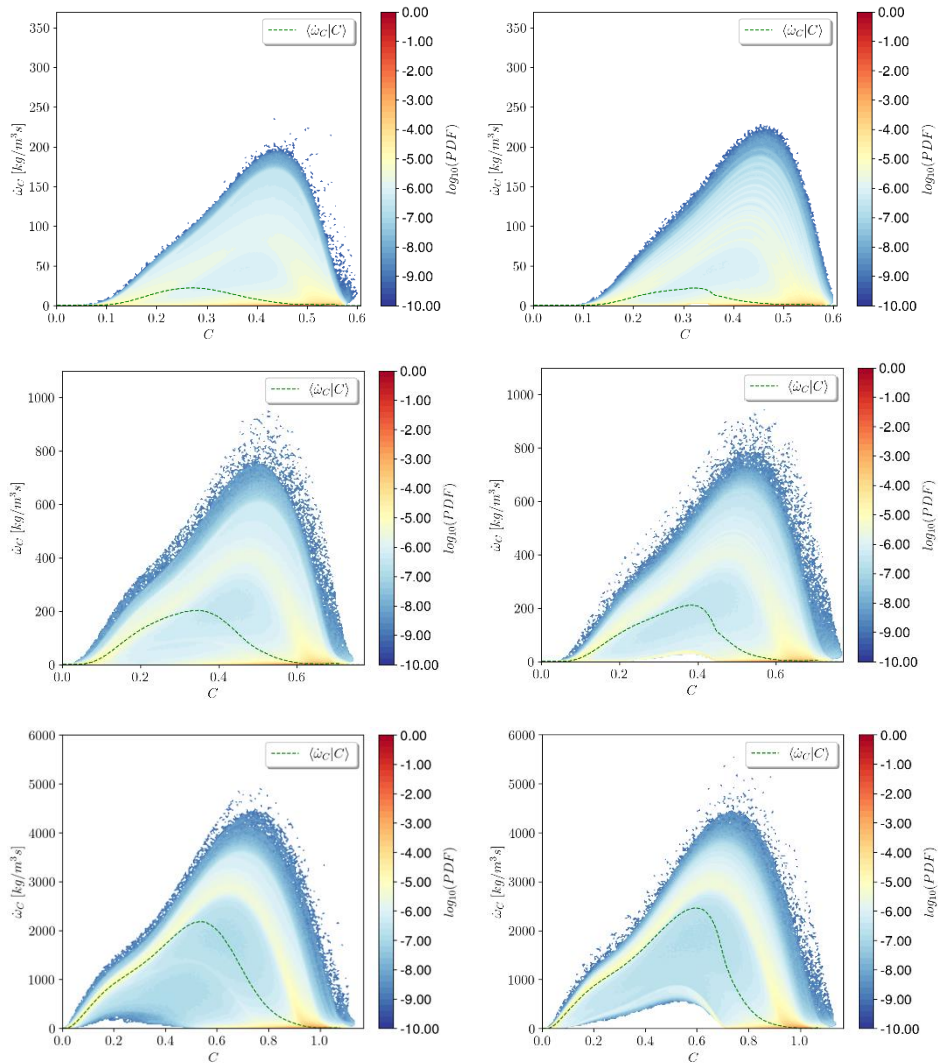


Figure 17. Joint distribution of the progress variable source term and normalized progress variable. From top to bottom:  $Y_{O_2,2} = 0.23$ ,  $Y_{O_2,2} = 0.3$ , and  $Y_{O_2,2} = 0.5$ . Left: detailed chemistry simulation, right: Model A.

The predicted consumption speed and joint distribution from Model A align closely with the reference results from detailed chemistry simulations, demonstrating the model's robustness under these conditions.

This analysis concludes the validation of Model A under laminar conditions, confirming its ability to accurately predict key combustion quantities, including consumption speed and the dynamics of TD instabilities. These results highlight the suitable model strategy for accounting to TD and strengthen confidence in the model's applicability to more complex turbulent scenarios discussed in Chapter 4.

### 3.5 Model B description in the frame of laminar combustion

Model B is developed in the frame of tabulated chemistry, where the thermochemical states are tabulated as a function of some flow variables (named controlling variables), and it is based on the developments introduced by Donini et al. [14] and de Swaart et al. [10]. Unlike these approaches, model B incorporates a complete mixture-averaged diffusion model with the Soret effect to model species diffusion. A mixture-averaged diffusion model was chosen since it does not require any adjustment of the Lewis numbers. Moreover, the Soret effect, which consists of a mass flux due to the temperature gradient, can have a strong impact when the flame curvature becomes dominant [25].

## D2.3 - Report on simulation framework for H<sub>2</sub>/O<sub>2</sub> and H<sub>2</sub>/air combustion

The second distinguishing aspect of model B is that no restriction is imposed on the alignment of the gradients of the controlling variables (w.r.t. the preferential diffusion contributions see de Swaart et al. [10]), thus allowing greater flexibility for the controlling variables to adapt to the local flow conditions. A comprehensive description of the method can be found in Pérez-Sánchez et al. [26].

According to the mixture-averaged diffusion model, the species' molar diffusion fluxes can be approximated as

$$V_k X_k = -D_k \nabla X_k, \quad (1)$$

where  $D_k$  is

$$D_k = \frac{1-Y_k}{\sum_{j \neq k}^{N_s} X_j D'_{jk}} \quad k = 1, \dots, N_s. \quad (2)$$

$V_k$ ,  $Y_k$ ,  $X_k$  and  $D_k$  denote the diffusion velocity, the mass and molar fractions, and the diffusion coefficient for the  $k$ -th species, respectively.  $D'_{jk}$  is the binary diffusion coefficient between the  $j$ -th and  $k$ -th species and  $N_s$  is the species number. To obtain the mass species flux, it is convenient to rewrite Eq. 1 as a function of the mass fractions. The diffusion flux contributions are completed by considering the Soret effect. Moreover, as the whole set of contributions may not conserve mass, a velocity correction is added. With these adjustments, the final mass flux for the  $k$ -th species,  $j_k$ , takes the form:

$$-D_k \nabla Y_k - D_k Y_k \frac{\nabla W}{W} + Y_k \sum_{j=1}^{N_s} D_j \nabla Y_j + \frac{\nabla W}{W} Y_k \sum_{j=1}^{N_s} D_j Y_j - \frac{D_k^T}{T} \nabla T + Y_k \sum_{j=1}^{N_s} \frac{D_j^T}{T} \nabla T. \quad (3)$$

According to tabulated chemistry methods, the thermochemical states of the flame can be represented as a function of a reduced set of flow variables,  $\phi_i$ , reducing, thus, the computational complexity of the system. These variables, which represent the degrees of freedom of the system and are referred as controlling variables, allow to write the rest of the system variables as

$$\Psi = \Psi(\phi_1, \dots, \phi_{N_c}), \quad (4)$$

where  $N_c$  is the number of control variables. This means that a mapping from the thermochemical states into the controlling variables is established. The choice of the controlling variables is case-dependent, and it is most of the time dictated by physical considerations. A lack of the representativeness of these variables to describe the states of the system may negatively affect the accuracy of the results. Therefore, their proper choice is a crucial step. In this work, the simulations have been conducted using the progress variable and mixture fraction for the laminar cases [27] [28] and their filtered values and variances for the RANS and LES [18].

Based on equation (4), after applying the chain rule, the flux  $j_k$  can be rewritten as

$$j_k = - \sum_{i=1}^{N_c} \left( D_k \frac{\partial Y_k}{\partial \phi_i} + \frac{D_k Y_k}{W} \frac{\partial W}{\partial \phi_i} - Y_k \sum_{j=1}^{N_s} D_j \frac{\partial Y_j}{\partial \phi_i} - \frac{Y_k}{W} \frac{\partial W}{\partial \phi_i} \sum_{j=1}^{N_s} D_j Y_j + \frac{D_k^T}{T} \frac{\partial T}{\partial \phi_i} - \frac{Y_k}{T} \frac{\partial T}{\partial \phi_i} \sum_{j=1}^{N_s} D_j^T \right) \nabla \phi_i \quad (5)$$

$$= - \sum_{i=1}^{N_c} \Lambda_{Y_k, \phi_i} \nabla \phi_i.$$

After applying the chain rule, it is observed that the mass diffusive flux can be written as a sum of contributions related to each of the controlling variables. Each contribution is composed of two parts: the first one, which corresponds to the coefficient  $\Lambda_{Y_k, \phi_i}$ , is related to the internal flame structure and only involves thermochemical and transport variables and derivatives in the phase space defined by the controlling

## D2.3 - Report on simulation framework for H<sub>2</sub>/O<sub>2</sub> and H<sub>2</sub>/air combustion

variables. On the contrary, the second part corresponds to the gradients in the physical space of the controlling variables which can be computed from the controlling variable fields solved in the CFD.

With these considerations, the transport equations for the controlling variables accounting for the preferential and differential diffusion effects can be easily obtained. The transport equation of the  $k$ -th species reads

$$\rho \frac{\partial Y_k}{\partial t} + \rho \mathbf{u} \cdot \nabla Y_k + \nabla \cdot (\rho \mathbf{j}_k) = \dot{\omega}_k, \quad (6)$$

where  $\rho$  and  $\mathbf{u}$  denote the flow density and velocity, respectively, and  $\dot{\omega}_k$  the chemical source term for the  $k$ -th species. The species transport equations can be linearly combined in turn to obtain transport equations for the controlling variables. Making use of the relationship established in Eq. 5 between the flux  $\mathbf{j}_k$  and the control variables, the following equation is finally obtained

$$\rho \frac{\partial \phi_i}{\partial t} + \rho \mathbf{u} \cdot \nabla \phi_i = \sum_{j=1}^{N_c} \nabla \cdot (\rho \Gamma_{\phi_i, \phi_j} \nabla \phi_j) + \dot{\omega}_{\phi_i}, \quad (7)$$

where  $\Gamma_{\phi_i, \phi_j}$  represents the coefficient related to the contribution of the  $j$ -th control variable in the transport equation for the  $i$ -th control variable and  $\dot{\omega}_{\phi_i}$  is the chemical source term for the  $i$ -th control variable. Coefficients  $\Gamma_{\phi_i, \phi_j}$  are obtained from the linear combination of coefficients  $\Lambda_{Y_k, \phi_i}$  based on the definition of the  $i$ -th control variable. Notice that due to the preferential/differential diffusion effects not only the coefficient  $\Gamma_{\phi_i, \phi_i}$  may differ from the thermal diffusivity but also cross terms  $\nabla \cdot (\rho \Gamma_{\phi_i, \phi_j} \nabla \phi_j)$  with  $i \neq j$  arise. This is a fundamental difference with the unity Lewis number case since there is no contribution in the controlling variable transport equation from the rest of the controlling variables. Therefore, the cross terms act as sources and sink terms that deviate the flame evolution from the one predicted by assuming unity Lewis number.

Of particular interest is applying Eq. 7 to the progress variable ( $Y_c$ ) and the mixture fraction ( $Z$ ) when solving adiabatic flames, i.e., without heat losses. Conceptually,  $Y_c$  measures the degree of advancement of the combustion with regard to some states of reference corresponding to the initial and final states of the evolution, while  $Z$  is a measure of the amount of mass coming from the fuel. Differently from the progress variable, the mixture fraction is conserved in a premixed flame if no preferential/differential diffusion effects are considered. Bilger's definition allows the mixture fraction to be written as a weighted sum of the species mass fractions, where the weights are the species and elements molecular weights and the number of atoms of each element composing the species. Based on this, Eq. 7 is particularized for both the progress variable and the mixture fraction:

$$\rho \frac{\partial Y_c}{\partial t} + \rho \mathbf{u} \cdot \nabla Y_c = \nabla \cdot (\rho \Gamma_{Y_c, Y_c} \nabla Y_c + \rho \Gamma_{Y_c, Z} \nabla Z) + \dot{\omega}_{Y_c}, \quad (8)$$

$$\rho \frac{\partial Z}{\partial t} + \rho \mathbf{u} \cdot \nabla Z = \nabla \cdot (\rho \Gamma_{Z, Y_c} \nabla Y_c + \rho \Gamma_{Z, Z} \nabla Z). \quad (9)$$

For a more detailed description of the specific form of the coefficients and other aspects of the formulation, the reader is referred to Pérez-Sánchez et al. [26].

When considering heat losses, it is necessary to transport the enthalpy  $h$ , whose transport equation, after neglecting the dissipation due to viscous forces, pressure term, and body force reads:

$$\rho \frac{\partial h}{\partial t} + \rho \mathbf{u} \cdot \nabla h + \nabla \cdot (\rho \mathbf{j}_h) = 0. \quad (10)$$

The diffusion flux  $\mathbf{j}_h$  corresponds to

### D2.3 - Report on simulation framework for H<sub>2</sub>/O<sub>2</sub> and H<sub>2</sub>/air combustion

$$j_h = -\frac{\lambda}{\rho} \nabla T + \sum_{k=1}^{N_s} (V_k + V_c) Y_k h_k, \quad (11)$$

being the first term the Fourier's law and the second one the transport of enthalpy due to species gradients. The chain rule is applied again to obtain

$$j_h = \sum_{i=1}^{N_c} \Gamma_{h,\phi_i} \nabla \phi_i, \quad (12)$$

being

$$\Gamma_{h,\phi_i} = \frac{\lambda}{\rho} \frac{\partial T}{\partial \phi_i} + \sum_{k=1}^{N_s} \Lambda_{Y_k,\phi_i} h_k. \quad (13)$$

In this case, the effect of the enthalpy is translated into new cross terms in the equations for the mixture fraction and progress variable, finally leading to

$$\rho \frac{\partial Y_c}{\partial t} + \rho u \cdot \nabla Y_c = \nabla \cdot (\rho \Gamma_{Y_c,Y_c} \nabla Y_c + \rho \Gamma_{Y_c,Z} \nabla Z + \rho \Gamma_{Y_c,h} \nabla h) + \rho \dot{\omega}_{Y_c}, \quad (14)$$

$$\rho \frac{\partial Z}{\partial t} + \rho u \cdot \nabla Z = \nabla \cdot (\rho \Gamma_{Z,Y_c} \nabla Y_c + \rho \Gamma_{Z,Z} \nabla Z + \rho \Gamma_{Z,h} \nabla h), \quad (15)$$

$$\rho \frac{\partial h}{\partial t} + \rho u \cdot \nabla h = \nabla \cdot (\rho \Gamma_{h,Y_c} \nabla Y_c + \rho \Gamma_{h,Z} \nabla Z + \rho \Gamma_{h,h} \nabla h). \quad (16)$$

These equations have to be solved in conjunction with the continuity and momentum equations to allow for a complete description of the flow.

Another aspect of interest is the accurate calculation of the derivatives in the form  $\frac{\partial \psi}{\partial \phi_i}$  appearing in coefficients. Such derivatives are computed considering that only  $\phi_i$  changes, keeping the rest of the controlling variables constant. When dealing with preferential/differential diffusion two problems arise. First, the manifold is typically constructed from one-dimensional flames, and differently from the  $Le = 1$  case, no control variable remains constant along the flame trajectory. This means that the computation of the derivatives involves considering states coming from different flames. Therefore, the calculation of the derivatives implies interpolation from an original set of discrete data, which does not lie on any orthogonal mesh, into a more convenient mesh. In this process, there may be losses of accuracy which may produce some noisy values for the derivatives. The second problem is that the flames are usually saved in manifolds that depend on the normalized controlling variables instead of the controlling variables themselves. In general, such normalization introduces an artificial curvature in the hyper-surfaces  $\Psi = \Psi(\phi_1, \dots, \phi_{N_c})$ .

To avoid these issues, the derivatives  $\frac{\partial \Psi}{\partial \phi_i}$  are rewritten in terms of the normalized controlling variables after applying the chain rule and considering the specific form of the normalization. This implies a previous interpolation step to transfer the information into an orthogonal mesh in the normalized controlling variable space. A complete description of the algorithm used, for the case where the progress variable and mixture fraction are the control variables, is given in Pérez-Sánchez et al. [26].

### 3.6 Model B description in the frame of turbulent combustion

As previously explained, when dealing with turbulent combustion the disparity of flow temporal and spatial scales is so large that it becomes unfeasible to solve the instantaneous equations (Direct Numerical Simulations). RANS and LES become a competitive solution being the adequacy of each approach depending on the computational cost and the nature of the phenomena to be studied. While in the RANS the instantaneous equations are averaged and the effect of all the scales has to be condensed in the turbulent transport terms, in the LES the equations are filtered and only the sub-grid effects have to be modeled. From a formal point of view, the procedure to obtain the averaged/filtered equations is similar. In the following, equations are given for the LES framework while the specific form for RANS simulations is presented in Chapter 5.

Extending the ideas related to tabulated chemistry to turbulent combustion, the averaged/filtered thermochemical states can be described again as a function of  $N'_c$  averaged/filtered controlling variables  $\tilde{\Psi} = \tilde{\Psi}(\tilde{\phi}_1, \dots, \tilde{\phi}_{N'_c})$ . Such controlling variables usually correspond to the averaged/filtered control variables as well as their variances.

The calculation of the turbulent manifold starts, first, by considering the laminar manifold and, second, by giving a statistical treatment to the manifold based on a joint-Probability Density Function (jPDF) of the controlling variables. In this manner, the Turbulence-Chemistry Interaction (TCI) is accounted for. For  $Le = 1$ , on many occasions, statistical independence is assumed for the controlling variables, simplifying the formulation of the jPDF to a product of the PDFs of each controlling variable. Such PDFs are parametrized as a function of the first moments of the turbulent field. To reduce the computational load many times, these are described based only on the averaged/filtered value of the specific controlling variable and its variance. In this manner, both of them are solved or transported in the flow giving a good trade-off between cost and accuracy.

When considering preferential diffusion effects, the assumption of statistical independence may not be valid as for the unity Lewis number case. However, it is argued that variances for most of the flow regions are, in general, very small (especially in LES) and, hence, the shape of the jPDF is not that critical [29]. Therefore, the errors introduced by this assumption are expected to be limited. This is considered, however, a subject of study for future works. In the current implementation, beta functions are considered for the single PDFs.

When considering adiabatic combustion, where the progress variable and mixture fraction are the controlling variables, the averaged/filtered values for the thermochemical variables take the form:

$$\tilde{\Psi} = \int_0^1 \int_0^1 \Psi(c, Z) P(c, Z; \tilde{c}, c_v, \tilde{Z}, Z_v) dc dZ = \int_0^1 \int_0^1 \Psi(c, Z) P_c(c; \tilde{c}, c_v) P_Z(Z; \tilde{Z}, Z_v) dc dZ, \quad (17)$$

where  $c$  denotes the normalized progress variable and the Favre averaging is denoted with tildes. Transport equations for the averaged/filtered controlling variables and their variances are essentially identical in RANS and LES showing some differences in the modeling of the dissipation term of the variance transport equations.

- a. Averaged/filtered progress variable and mixture fraction:

$$\bar{\rho} \frac{\partial \tilde{Y}_c}{\partial t} + \bar{\rho} \tilde{u} \cdot \nabla \tilde{Y}_c = \nabla \cdot \left( \bar{\rho} \left( \overline{\Gamma_{Y_c, Y_c}} + \frac{\nu_t}{Sc_t} \right) \nabla \tilde{Y}_c + \overline{\rho \Gamma_{Y_c, Z}} \nabla \tilde{Z} \right) + \bar{\omega}_{Y_c}, \quad (18)$$

$$\bar{\rho} \frac{\partial \tilde{Z}}{\partial t} + \bar{\rho} \tilde{u} \cdot \nabla \tilde{Z} = \nabla \cdot \left( \overline{\rho \Gamma_{Z, Y_c}} \nabla \tilde{Y}_c + \bar{\rho} \left( \overline{\Gamma_{Z, Z}} + \frac{\nu_t}{Sc_t} \right) \nabla \tilde{Z} \right). \quad (19)$$

- b. Averaged/filtered variances for the progress variable and mixture fraction:

### D2.3 - Report on simulation framework for H<sub>2</sub>/O<sub>2</sub> and H<sub>2</sub>/air combustion

$$\begin{aligned} \bar{\rho} \frac{\partial Y_{c,v}}{\partial t} + \rho \tilde{u} \cdot \nabla Y_{c,v} & \quad (20) \\ & = \nabla \cdot \left( \rho \left[ \Gamma_{Y_c, Y_c} + \frac{\nu_t}{S_{C_t}} \right] \nabla Y_{c,v} \right) + 2 \bar{\rho} \frac{\nu_t}{S_{C_t}} \nabla \tilde{Y}_c \cdot \nabla \tilde{Y}_c - \bar{\rho} C_{Y_c} \frac{\nu_t}{S_{C_t}} \frac{Y_{c,v}}{\Delta^2} \\ & \quad + 2 \left( \overline{Y_c \omega_{Y_c}} - \overline{Y_c} \overline{\omega_{Y_c}} \right), \end{aligned}$$

$$\bar{\rho} \frac{\partial Z_v}{\partial t} + \bar{\rho} \tilde{u} \cdot \nabla Z_v = \nabla \cdot \left( \bar{\rho} \left[ \Gamma_{Z,Z} + \frac{\nu_t}{S_{C_t}} \right] \nabla Z_v \right) + 2 \bar{\rho} \frac{\nu_t}{S_{C_t}} \nabla \tilde{Z} \cdot \nabla \tilde{Z} - \bar{\rho} C_Z \frac{\nu_t}{S_{C_t}} \frac{Z_v}{\Delta^2}. \quad (21)$$

Extending the formulation to heat losses is straightforward.

### 3.7 Model B validation in 1D and 2D configurations

In the following, a validation of the model is presented, first for one-dimensional flames and then, for two-dimensional configurations. The results correspond to the implementation carried out with the in-house multiphysics code, Alya, [30] developed at BSC. An explicit Runge-Kutta 3rd-order scheme is used for the temporal integration while a second-order discretization is employed in space. The manifold is constructed from a set of unstretched adiabatic one-dimensional premixed flames computed with Cantera. Results from Cantera calculations are interpolated into an orthogonal mesh in the space of the normalized controlling variables. The coefficients  $\Gamma_{x,y}$  are computed and stored in the look-up tables. In all the cases water mass fraction is used as progress variable ( $Y_c = Y_{H_2O}$ ). For this validation, Boivin et al. mechanism has been used [31].

First, the flame speed,  $s_L$ , and flame thickness,  $l_F$ , for a wide range of equivalence ratios are presented in Figure 18. Results correspond to unstretched adiabatic one-dimensional premixed flames at atmospheric pressure and fresh gases temperature of 298.15 K computed with both Cantera and Alya. To test the capabilities of the model more realistically, both the mixture fraction and the progress variable are transported even, due to the one-dimensionality of the problem, it could be solved uniquely by transporting the progress variable.

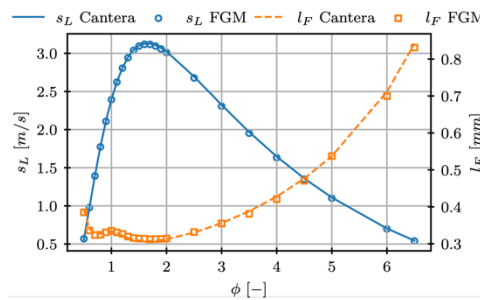


Figure 18. Flame speed  $s_L$  and thermal flame thickness  $l_F$  comparison between Cantera (solid and dashed lines respectively) and Alya FGM (circle and square markers respectively) for one-dimensional adiabatic hydrogen/air flames at atmospheric pressure and unburnt gas temperature of 298.15 K.

Figure 18 shows that an excellent agreement exists between the values computed using Cantera and those obtained from the tabulated chemistry model, with the errors limited to 1.5% and 2.3% for the flame speed and the flame thickness, respectively. Moreover in Figure 19, the flame structure is compared with those solutions from Cantera by representing different variables of interest as a function of the progress variable for lean, stoichiometric, and rich mixture fractions. For representation purposes, the variables are normalized.

## D2.3 - Report on simulation framework for H<sub>2</sub>/O<sub>2</sub> and H<sub>2</sub>/air combustion

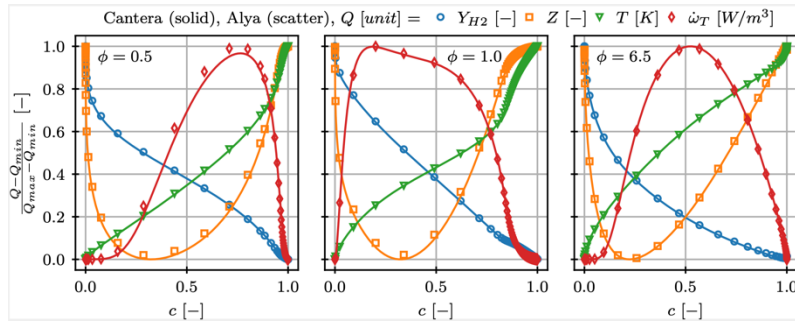


Figure 19. Normalized profiles of hydrogen mass fraction, mixture fraction, temperature, and heat release for a lean, stoichiometric, and rich mixture. Results for Cantera and Alya.

The agreement between the tabulated chemistry model and the reference Cantera is remarkable, showing that the model integrally recovers the one-dimensional flames.

The validation continues with the comparison of the results for three triple flames obtained with tabulated chemistry with differential and preferential diffusion effects and with finite rate chemistry, computed again with Alya. This configuration is challenging since it presents a stratification of the mixture fraction which covers the whole range of the flammability limit. Therefore, a non-uniform profile for the mixture fraction is imposed at the inlet. The profile varies monotonically inside a given interval, whose size defines the mixing length, while it is constant outside it. The stratification, induces the formation of two premixed flames at the sides, one lean and the other rich, and a diffusion flame in the inner region limited by the premixed flames where the products of these flames are finally oxidized. A total of three flames with different stratification levels are considered: 3.02 (I), 6.05 (II), and 9.7 (III), where the values denote the ratio between the mixing length and the one-dimensional flame thickness. Flames are at atmospheric pressure while the inlet temperature is uniform and equal to 298 K.

First, a qualitative comparison of the heat release fields is shown in Figure 20 for tabulated chemistry and finite-rate chemistry for the different mixing lengths.

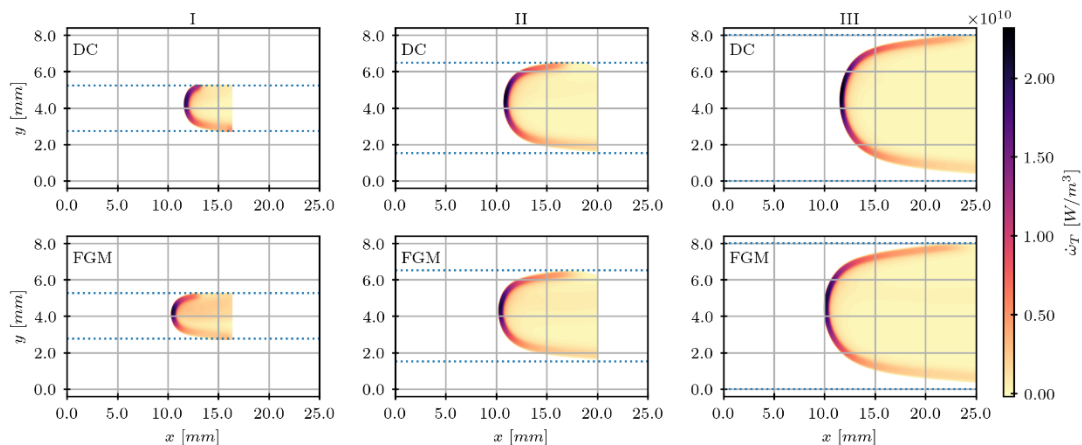


Figure 20. Contour plots of heat release for the different mixing lengths. The top half corresponds to finite rate chemistry solution while the bottom half to tabulated chemistry. The blue dotted lines indicate the size of the domain in the transversal direction. All flames are centered for visualization.

It is observed that, in general, there exists a good qualitative agreement between the models for all the cases. A reduction of the mixing length, that is, increasing the gradient in mixture fraction, tends to deteriorate the prediction of the flame shape. This is attributed to the strong gradients misaligned with the normal to the flame, that tend to alter the flame structure gathered in the manifold.

A more quantitative comparison is carried out by comparing how the different scalars evolve along level curves for the progress variable and mixture fraction. Results are shown for case III (highest mixing length) for finite rate chemistry and tabulated chemistry in Figure 21 and Figure 22.

## D2.3 - Report on simulation framework for H<sub>2</sub>/O<sub>2</sub> and H<sub>2</sub>/air combustion

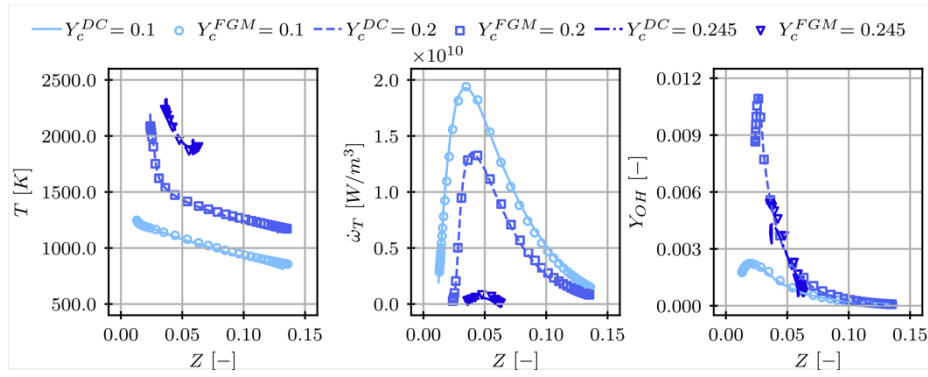


Figure 21. Values of temperature, heat release, and hydroxide mass fraction vs mixture fraction along the isolines for progress variable  $Y_c = 0.1$  (light blue),  $0.2$  (blue), and  $0.245$  (dark blue) for finite rate model (lines), and tabulated chemistry (empty markers) for flame III.

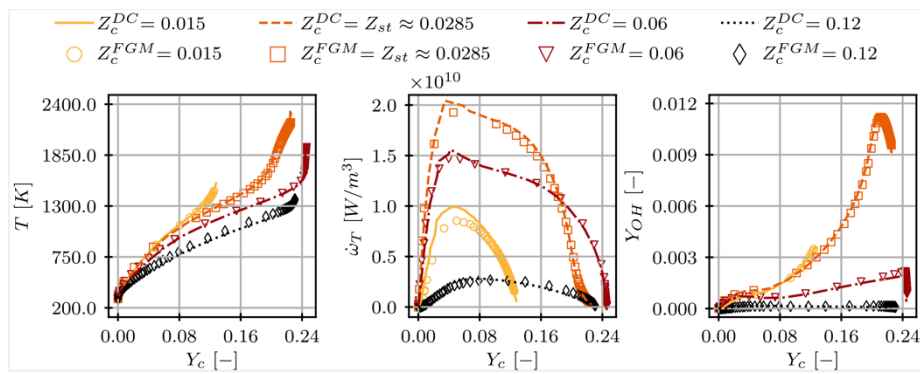


Figure 22. Values of temperature, heat release, and hydroxide mass fraction vs progress variable along the isolines for mixture fraction  $Z = 0.015$  (light orange),  $Z_{st} = 0.0285$  (orange),  $0.06$  (dark red), and  $0.12$  (black) for finite rate model (lines), and tabulated chemistry (empty markers) for flame III.

As observed, there exists an excellent agreement for all the variables with minor discrepancies for heat release at very lean mixtures. For a broader description of the conditions and an exhaustive comparison between models, the reader is referred to Pérez-Sánchez et al. [26].

The validation for two-dimensional flames is assessed with the comparison of the predictions between finite rate chemistry and tabulated chemistry for a slit flame with heat losses. A premixed mixture of hydrogen and air at ambient temperature and an equivalence ratio of 0.5 is injected at a velocity of 0.565 m/s. Walls are kept at 300 K. Pressure is atmospheric. The width of the slit is 0.8 mm and the mesh is structured with a uniform cell size of 0.01 mm.

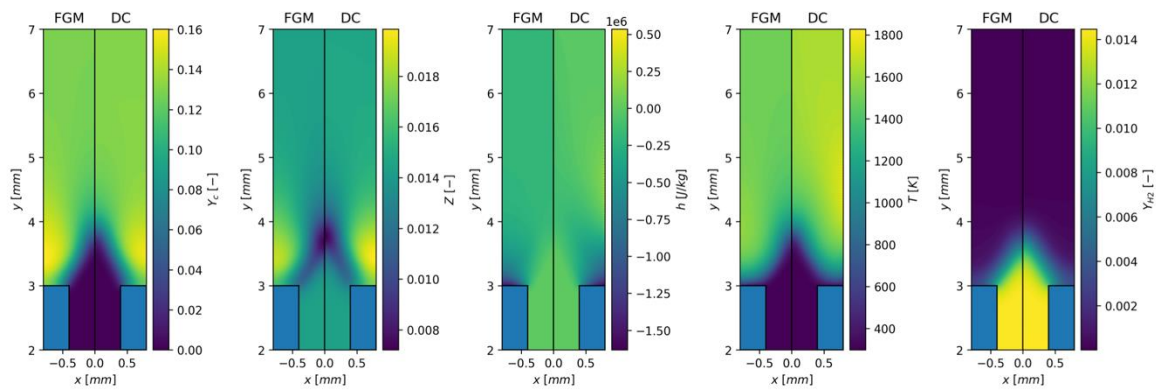


Figure 23. Comparison of the progress variable (left), mixture fraction (center left), enthalpy (center right), and temperature (right) for tabulated chemistry (left side), and finite rate chemistry (right side).

Results in Figure 23 show that there exists a good agreement between models for the different fields. In the case of the mixture fraction, the leaning of the mixture along the flame and especially at the tip is captured by

## D2.3 - Report on simulation framework for H<sub>2</sub>/O<sub>2</sub> and H<sub>2</sub>/air combustion

the tabulated chemistry. The lateral enrichment in the burnt gases side is well-described even the peak mixture fraction is slightly underpredicted by the tabulated chemistry model.

The good agreement obtained so far for the validation of the model encourages its application in challenging configurations where the dynamic effects play a dominant role.

### 3.8 Model B application: analysis of the freely propagating flames for different boundary conditions in the non-linear regime

In the following, model B is applied to a set of two-dimensional premixed freely propagating flames for different inlet temperatures and oxygen content in air at atmospheric pressure. The description is limited to the non-linear regime, that is after the very initial perturbation develops. Simulations are also performed with finite-rate chemistry in order to have reference data for the tabulated chemistry results. All the cases are simulated with Alya. The chemical mechanism employed in these simulations is the one developed in Task 1.4 of the project. Table 3 shows the cases simulated.

		Y <sub>O2</sub>		
		0.23	0.3	0.5
Inlet temperature	298 K	X	X	X
	700 K			X

Table 3. Description of the simulated cases.

For all the cases the equivalence ratio is set equal to 0.5. Square domains of  $200 l_f \times 200 l_f$ , where  $l_f$  is the flame thickness of the one-dimensional adiabatic flame for each case, are meshed uniformly with squares of size one-tenth of the flame thickness. Three flame descriptors are analyzed:

- Consumption speed: to characterize the flame front burning velocity:

$$s_c = -\frac{1}{\rho_u Y_{H_2, u} L_x} \int \dot{\omega}_{H_2} dx dy. \quad (22)$$

- Flame surface area: the measure of the flame front length:

$$l = \int |\nabla c| dx dy. \quad (23)$$

- Reactivity ratio: to quantify the deviation of the two-dimensional flame from that of the unstretched one-dimensional flame:

$$I_0 = \frac{s_c L_x}{s_L l}. \quad (24)$$

The simulations were run during at least  $100 \tau$ , where  $\tau = \frac{l_F}{s_L}$ .

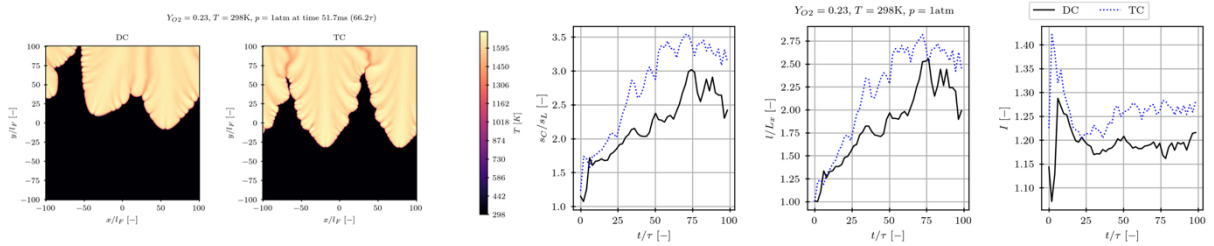


Figure 24. Results for  $Y_{O_2} = 0.23$  and  $T_{inlet} = 298 K$ . Left panel: snapshots of the flame front for the finite rate chemistry (left) and tabulated chemistry (right). Right panel: temporal evolution for the consumption speed (left), flame surface area (center), and the reactivity ratio (right) for both models.

## D2.3 - Report on simulation framework for H<sub>2</sub>/O<sub>2</sub> and H<sub>2</sub>/air combustion

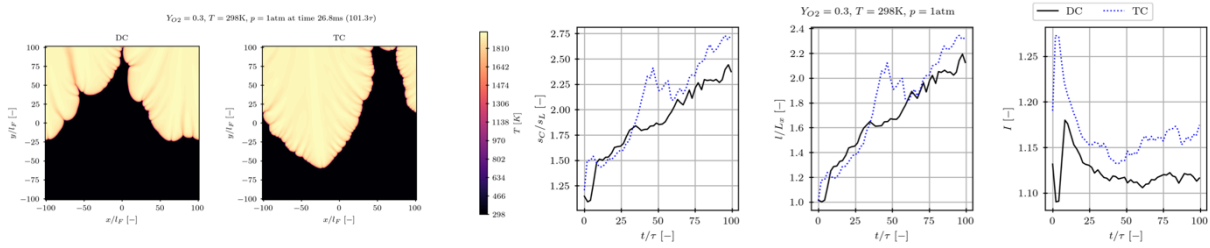


Figure 25. Results for  $Y_{O_2} = 0.3$  and  $T_{inlet} = 298\text{K}$ . Left panel: snapshots of the flame front for the finite rate chemistry (left) and tabulated chemistry (right). Right panel: temporal evolution for the consumption speed (left), flame surface area (center), and the reactivity ratio (right) for both models.

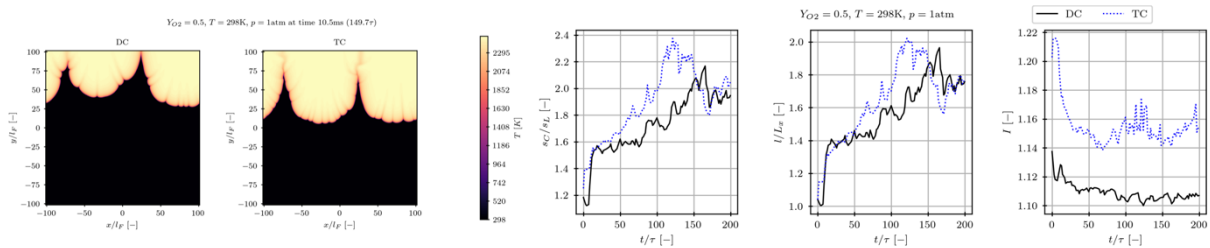


Figure 26. Results for  $Y_{O_2} = 0.5$  and  $T_{inlet} = 298\text{K}$ . Left panel: snapshots of the flame front for the finite rate chemistry (left) and tabulated chemistry (right). Right panel: temporal evolution for the consumption speed (left), flame surface area (center), and the reactivity ratio (right) for both models.

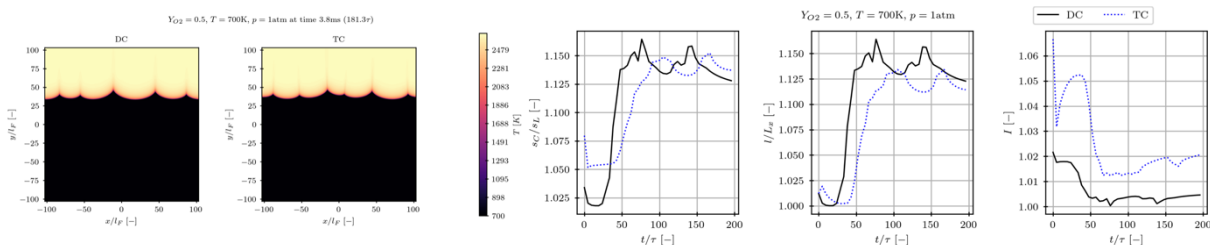


Figure 27. Results for  $Y_{O_2} = 0.5$  and  $T_{inlet} = 700\text{K}$ . Left panel: snapshots of the flame front for the finite rate chemistry (left) and tabulated chemistry (right). Right panel: temporal evolution for the consumption speed (left), flame surface area (center), and reactivity ratio (right) for both models.

A qualitative comparison of the results shows that the tabulated chemistry model captures the morphology of the flame. A large variety of wavelengths are detected in the flame front separated by sharp intrusions of the fresh gas into the burnt mixture. There exists a similarity in the finger-like structures predicted by both approaches. The low equivalence ratio (0.5) tends to trigger the thermo-diffusive instabilities which in turn affect the flame front by enhancing the number of small-scale structures. In the concave regions (seen from the fresh gases), the mixture fraction and, in turn, the temperature are reduced as a consequence of the differential diffusion effects, a feature that is captured by the tabulated chemistry model as demonstrates the fainter purple grooves emerging from the cusps of the structures. On the contrary, in the convex regions (seen from the fresh gases), the mixture fraction and the temperature tend to increase as can be seen from the whiter yellow color emerging from the lowest points of the flame front for the cases  $Y_{O_2} = 0.23$  (Figure 24) and  $Y_{O_2} = 0.3$  (Figure 25).

A more quantitative picture of the capabilities of the model is given by the comparison of the temporal evolution of the aforementioned flame descriptors. In general, the errors are limited and bounded by a peak value of 20% approximately. The greatest errors are observed for both the consumption speed and the flame surface area in contrast with the reactivity ratio for which discrepancies are more attenuated. In general, the

### D2.3 - Report on simulation framework for H<sub>2</sub>/O<sub>2</sub> and H<sub>2</sub>/air combustion

tabulated chemistry model tends to overpredict the flame descriptors. This is attributed to the fact that the internal flame structure is fixed for the tabulated chemistry. However, the agreement obtained for the flame descriptors shows that even though there are some deviations in finite rate chemistry, their effects are not dominant. In line with this, it is worth mentioning that when increasing the content of oxygen in air, there exists an improvement in the quality of the results, with a remarkable reduction of the errors. This is due to a reinforcement of the flamelet hypothesis as the flame thickness is reduced due to the enhanced reactivity (also reflected by the higher temperatures achieved in the domain). On the contrary, when increasing the temperature, the flame thickness is slightly augmented, but the destabilizing effects generated by the hydrodynamic and differential diffusion are moderated, leading to a less wrinkled flame front, that is, a flatter flame where the curvature effects are more limited. For a dedicated study of the capabilities of this tabulated chemistry model to reproduce the flame evolution in both the linear and the non-linear regimes, the reader is referred to Fortes et al. [32].

# 4 High-fidelity LES

## 4.1 Introduction

One of the most powerful aspects of the tabulated chemistry models is their ability to simulate turbulent flames in the frame of LES. Their accuracy (they allow to incorporate the TCI from the not solved scales), together with their low computational cost, make them a very popular approach. In Sections 3.3 and 3.6, the extension of models A and B, respectively, to turbulent combustion was given. In the next paragraphs, results for both approaches are provided for a set of representative turbulent flame configurations in the frame of LES leaving results related to RANS to Chapter 5.

## 4.2 Analysis of the planar turbulent jet flame with LES

In this section, a turbulent premixed planar hydrogen jet flame is simulated using LES and compared with DNS data generated from RWTH-ITV [7]. A brief description of the flame configuration is given below (a complete description can be found in Berger et al. [7]). The flame consists of a statistically planar jet injected at ambient temperature and a mixture of hydrogen/air at an equivalence ratio of 0.4 to promote thermodiffusive instabilities. The jet is injected at a velocity of 24 m/s while the distance between the slot walls is 8 mm, giving a Reynolds number of 11000. The jet is surrounded by a hot coflow which consists of the burnt gases of the premixed flame of the main injection. Therefore, in both streams, the mixture fraction is identical and the only variations in mixture fraction are caused by differential and preferential diffusion effects. The grid resolution is 0.07 mm and the pressure is atmospheric. Moreover, the flame is periodic in the spanwise direction.

Regarding the LESs, a total of four meshes are considered to quantify the effect of the mesh on results. Such assessment is of great importance since in real applications the typically high computational cost that would require fine meshes imposes serious restrictions on the mesh resolution. In this case, the four LES meshes are structured in two parts: an inner region that contains the core jet and the mixing layer, and an outer region. In the inner region, the cell aspect ratio is conserved, but cell dimensions are expanded in the downstream direction. Outside this inner region, the mesh is coarsened to reduce the computational cost. The four meshes are numbered M-X with X=1, 2, 3, and 4, where X denotes the number of cells along the wall slot thickness (0.4 mm). The number of elements for each mesh is 2M for M1, 9.5M for M2, 23M for M3, and 42M for M4. For the DNS mesh description, the reader is referred to [7]. Sub-grid viscosity is modeled with the Vreman model [33] and a turbulent Schmidt number of 0.7 was considered. For both DNS and LES, the Burke et al. mechanism was used [34].

Regarding the inlet conditions of both the LES and the DNS, the central jet velocities are obtained from an auxiliary fully developed turbulent channel flow simulation. On the other hand, laminar coflows are applied outside the central jet.

The turbulent combustion manifold is constructed according to Sections 3.5 and 3.6 and the equations for the filtered controlling variables are those given in Section 3.6. While in the case of the LES, the species diffusion fluxes are modeled using a mixture-averaged approach, in the case of the DNS, constant Lewis numbers are used. This is expected to introduce some minor deviations. Moreover, in the DNS, heat losses have been introduced by imposing the wall temperature equal to 298 K, while in the LES simulations, adiabatic wall conditions are used. This is supposed to have only some impact on the temperature fields close to the walls.

A qualitative comparison of the results is shown in Figure 28 by comparing the snapshots from both the DNS and the LES for M4 (finest mesh).

## D2.3 - Report on simulation framework for H<sub>2</sub>/O<sub>2</sub> and H<sub>2</sub>/air combustion

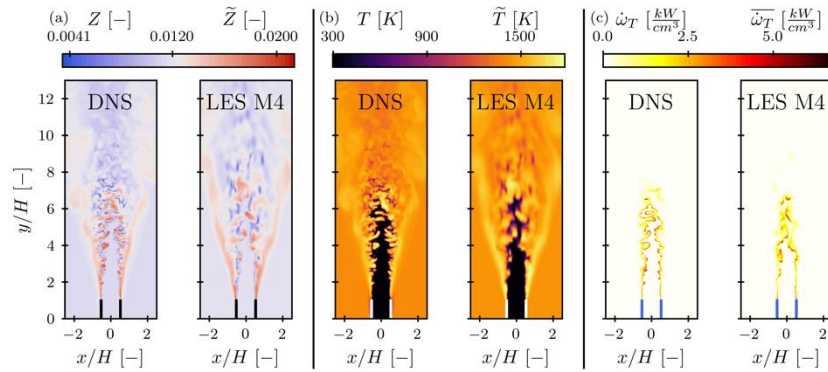


Figure 28. Instantaneous snapshots of the mixture fraction (a), temperature (b), and heat release rate (c) for the DNS and the LES with resolution M4 (left and right plots of each panel respectively).

It is observed that the flame morphology is well-captured by the tabulated chemistry model. The model is able to describe the fluctuations in mixture fraction that are produced around the zone of heat release, as a consequence of the joint effect of the turbulence and the thermodiffusive instabilities, which tend to increase the flame wrinkling. This is translated into remarkable fluctuations in temperature which may lead to super-adiabatic values in the convex parts of the flame front (mixture enrichment). As expected, the spatial variability of the mixture fraction is lower in the case of the LES compared to the DNS results due to the inherent filtering of the LES. Another possible cause is the capability of the model to reproduce mixture fractions fluctuations at the sub-grid level and how this impacts the filtered quantities (temperature and species mass fractions). This aspect will be further investigated.

Also, there is an increase in mixture fraction along two lateral branches at the sides of the jet which is well-reproduced by the tabulated chemistry model. Such an increase leads in turn to super-adiabatic temperatures. The heat release confirms the similarity of the flames, showing that the model accurately predicts the flame length.

The effect of the mesh resolution is shown in Figure 29 by comparing the temporally and spatially (in the span-wise direction) Reynolds averaged temperature field for the DNS and the LES for the different meshes (from coarser to finer mesh from left to right).

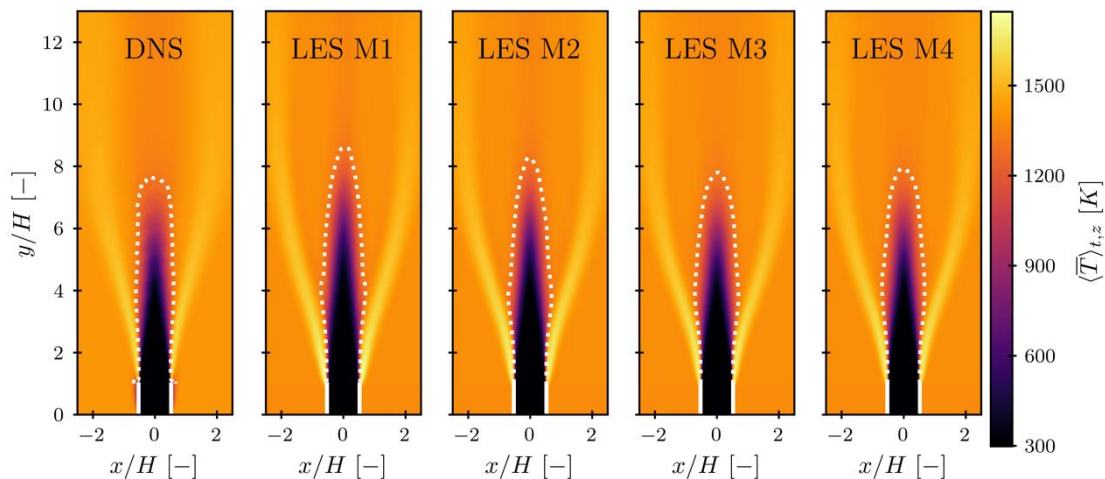


Figure 29. Temporally and spatially averaged temperature field for the DNS and the LES for the four meshes. The dashed white line corresponds to the iso-contour corresponding to a normalized temperature of 0.95.

Little dependence of the fields is observed on the mesh resolution, with a slight rounding of the flame tip and flame length reduction when refining the mesh. Compared with the DNS, the flame shape is similar even though the LES predicts a sharper flame head (based on the temperature level curve). Moreover, the spreading angle of the lateral branches is slightly overpredicted with the LES as well as the maximum temperature achieved in these regions. On the contrary, there exists an excellent agreement with the flame

## D2.3 - Report on simulation framework for H<sub>2</sub>/O<sub>2</sub> and H<sub>2</sub>/air combustion

length. Overall, it is deemed that the tabulated chemistry in the LES is able to capture the main flame characteristics and morphology of the fields.

To conclude this analysis, different flame descriptors are quantified for the different meshes: (i) the flame length,  $h_T$ , defined as the axial distance from the exit of the injection slot to a value of 0.95 of the normalized temperature on the axis and (ii) the consumption speed. Both flame length and consumption speed are normalized with the slot width  $H$  and the unstretched adiabatic one-dimensional flame speed  $s_L$ , respectively.

Case	$\frac{h_T}{H}$	$\frac{s_c}{s_L}$
DNS	7.62	8.37
LES M1	8.61	7.60
LES M2	8.29	8.09
LES M3	7.79	8.70
LES M4	7.92	8.60

Table 4. Flame length and consumption speed comparison for different LES resolutions.

As can be observed from Table 4, there exists some improvement in the flame descriptors when refining the mesh. Even for the LES M1, results are close to the DNS values with errors smaller than 10%. The results obtained so far are deemed to be a positive confirmation of the capabilities of this tabulated chemistry model for its application in the frame of LES. A more detailed analysis of these results has been carried out by Fortes et al. [35].

### 4.3 LES results of the IOB lab-scale furnace comparing $Le = 1$ and $Le \neq 1$

A second configuration where model B is applied is the simulation of a test rig from RWTH-IOB. It consists of a prototype high-velocity burner mounted inside a vertical lab-scale furnace with a cylindrical combustion chamber. There are two inlet streams: the primary stream consists of a partially premixed mixture of fuel, a methane and hydrogen blend, and air. The fuel is radially injected and mixes with the air which flows axially along an annular duct before reaching the entry to the combustion chamber. The secondary stream consists of pure air which is injected at high velocity to promote mixing. A set of methane-hydrogen mixtures have been tested, ranging from pure methane to pure hydrogen in intervals of 20% in volume. The equivalence ratio for all the mixtures is around 1.5 in the primary stream and 0.9 for both streams jointly.

Simulations were performed in the frame of LES with Alya. Moreover, these simulations have been performed including and neglecting differential and preferential diffusion effects ( $Le = 1$ ) to analyze their impact on the flame. The mesh is unstructured and composed of 15.5 M nodes and 90.4 M elements. Combustion is modeled in the frame of tabulated chemistry considering the mixture fraction, progress variable, and their variances as controlling variables. When generating the tables, the discretization in mixture fraction was adapted to each case as the stoichiometric mixture fraction changes with the volumetric percentage of fuels. However, for all the cases, the grid consisted of around 100 points with a refined discretization around the global mixture fraction, 101 uniformly distributed points for the normalized progress variable, and 11 points for the normalized variances of the mixture fraction and progress variable. The chemical mechanism used for these simulations is GRI3.0 [36]. Due to the presence of methane, the definition of the progress variable has been modified to better capture the flame's evolution. Therefore, except for pure hydrogen, for which  $Y_c = Y_{H_2O}$ , the progress variable is defined as  $Y_c = Y_{CO_2} * 4.0/44.0 + Y_{CO} * 1.0/28.0 + Y_{H_2O} * 2.0/18.0 + Y_{H_2} * 0.5/2.0$ .

Snapshots of temperature and mixture fraction are shown in Figure 30 and Figure 31 for all the cases modeled with the mixture-averaged diffusion model and Fick's law with unity Lewis number.

## D2.3 - Report on simulation framework for H<sub>2</sub>/O<sub>2</sub> and H<sub>2</sub>/air combustion

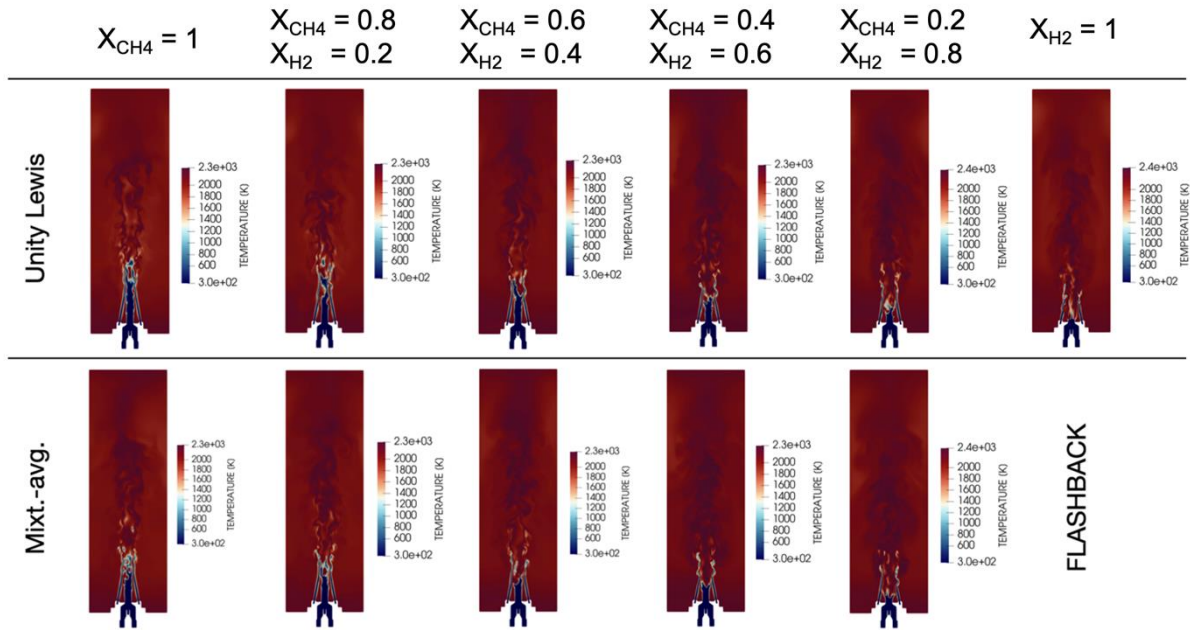


Figure 30. Instantaneous temperature fields for the six considered cases for unity Lewis (top) and mixture-averaged (bottom).

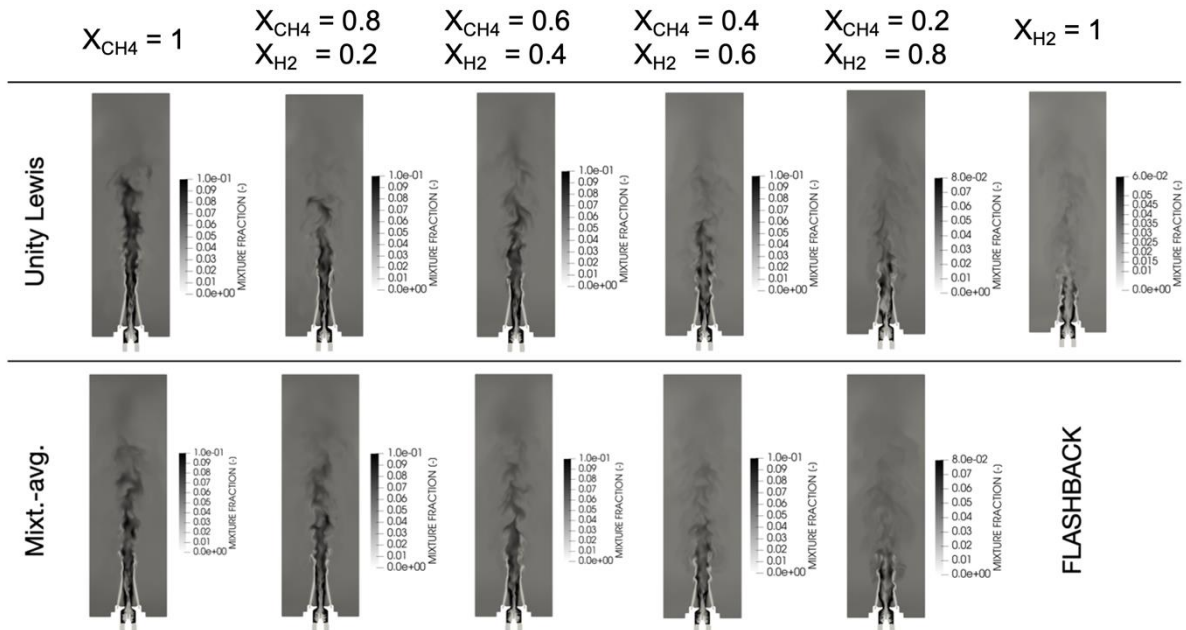


Figure 31. Instantaneous mixture fraction fields for the six considered cases for unity Lewis (top) and mixture-averaged (bottom).

The first aspect to mention is that the morphology of the flame dramatically changes when going from pure methane to pure hydrogen. This is attributed to the remarkably higher flame speeds that hydrogen features compared to methane as shown in Figure 32.

## D2.3 - Report on simulation framework for H<sub>2</sub>/O<sub>2</sub> and H<sub>2</sub>/air combustion

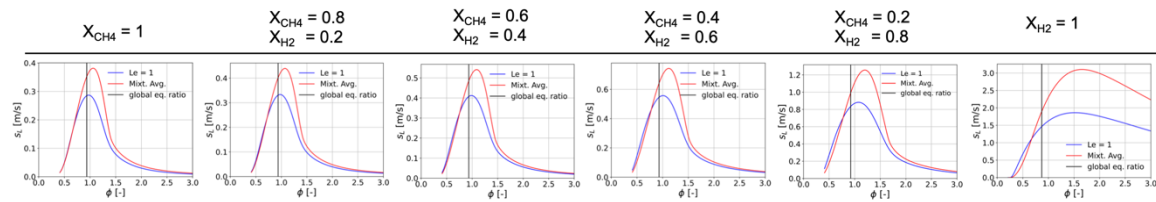


Figure 32. Comparison of laminar flame speeds for Lewis unity (blue) and mixture-averaged diffusion model (red). The vertical black line marks the global equivalence ratio of the LES in each case.

It is speculated that a possible secondary reason for the reduction of the flame length may be the heterogeneity of the inlet mixture entering into the combustion chamber, as can be observed from the mixture fraction field representation. When analyzing the mixture fraction field in the inlet tube it is observed that, due to the radial injection of the fuel and the relatively short tube distance, the fuel and the air do not properly mix and the heterogeneous mixture feeds the flame. This is translated into strong gradients of the mixture fraction field in the radial direction at the inlet plane: a very lean central core is observed while the periphery contrasts because of the highly rich mixtures. Downstream the injection the richness in the periphery tends to be reduced due to the mixing with the secondary air. As the content of hydrogen is increased, the stoichiometric mixture fraction is consequently decreased (for methane it equals 0.055 while for hydrogen 0.0285). Thus, the most reacting mixtures are confined to regions closer to the inlet. In other words, if the flame length was only based on the stoichiometric mixture, it would be shortened because of the mixing effects.

Comparing the predictions between models, it is observed that the mixture-averaged model systematically provides shorter flame lengths than the unity Lewis number. Indeed, for pure hydrogen, it is observed that for  $Le = 1$ , the flame reaches the inlet of the nozzle, while for mixture-averaged flashback arises. This generalized reduction of the flame length is attributed to the higher flame speeds with mixture-averaged compared to the  $Le = 1$  case which in turn are translated into higher molecular diffusivity and chemical source terms. A comparison of the chemical source term for the progress variable between unity Lewis number and mixture-averaged is shown in Figure 33 for the case  $X_{CH_4} = 0.2$  and  $X_{H_2} = 0.8$ .

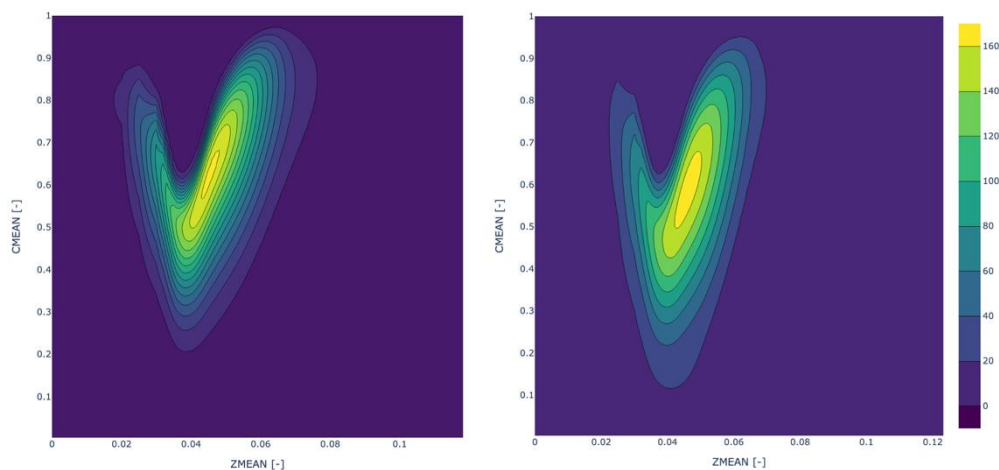


Figure 33. Maps of the progress variable source term ( $\text{kg}/\text{m}^3/\text{s}$ ) as a function of the mixture fraction (abscissa) and the normalized progress variable (ordinate) for  $X_{CH_4} = 0.2$  and  $X_{H_2} = 0.8$ . Left:  $Le = 1$ , right: mixture-averaged model.

It is observed that the peak value is slightly increased for the mixture-averaged diffusion model. More importantly, the region with representative values for the chemical source terms is enlarged, showing significant values at the lower progress variable. This is expected to influence the reactivity of the mixture.

Finally, the temporal evolution of the flame length is presented in Figure 34 to show that such reduction of the flame length does not occur sporadically but is sustained over time. As the instantaneous flame front features a complex shape, due to the interaction of both streams, the flame length is defined as the maximum

## D2.3 - Report on simulation framework for H<sub>2</sub>/O<sub>2</sub> and H<sub>2</sub>/air combustion

projected distance into the axis from the inlet to the downstream point which features a specific percentage of the peak heat release. Two percentage values are chosen, 20% and 50%, to avoid biased conclusions.

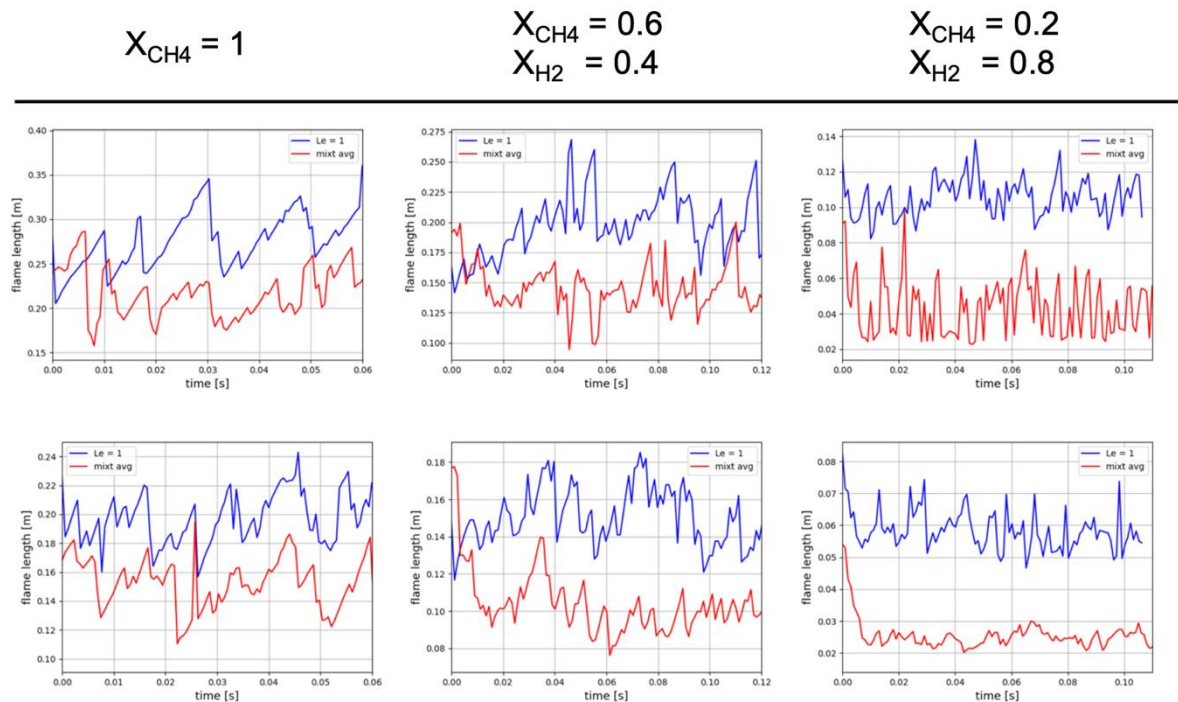


Figure 34. Temporal evolution of the flame length for  $Le = 1$  (blue) and mixture-averaged (red) for the cases  $X_{CH_4} = 1$  (left column),  $X_{CH_4} = 0.6$ , and  $X_{H_2} = 0.4$  (central column) and  $X_{CH_4} = 0.2$  and  $X_{H_2} = 0.8$  (right column). Top row: flame length defined with the 20% of the peak heat release. Bottom row: idem with 50% of the peak heat release.

It is observed that the  $Le = 1$  case systematically features greater flame lengths than the mixture-averaged regardless of the case and percentage. The signals become more noisy (higher frequency content) and with a smaller standard deviation when the flame length is reduced because of the increase in hydrogen content (notice that the scale of the figures is different for each case). This could be expected as the velocity fields experience similar behavior as a consequence of the reduction of velocities and the increase of the turbulent scales.

In summary, it can be stated that incorporating differential and preferential diffusion effects may introduce important changes in the flame morphology and, therefore, they should not be neglected.

## 4.4 LES of a turbulent jet premixed flame using Model A

The performance of Model A is evaluated in a three-dimensional turbulent scenario by a set of LESs obtained with RWTH-ITV's in-house software, CIAO. This software is a massive-parallel, higher-order semi-implicit finite difference code that solves the reacting Navier-Stokes equations in the low-Mach number limit. CIAO uses Crank-Nicolson time advancement and an iterative predictor corrector scheme. The momentum equation is discretized with a second-order scheme while a fifth-order WENO scheme [37] is used for the convective term of the scalar equations. Further details on the numerical framework can be found in Desjardins et al. [38].

For the subgrid stress tensor and scalar fluxes, the dynamic modeling approach proposed by Germano et al. [39] and Moin et al. [20] has been employed, respectively. Two different configurations are analyzed for which DNS data generated at RWTH-ITV are available. LESs were performed using two different grid resolutions: a finer grid ( $\Delta = 4dx$ ), four times coarser than the DNS resolution, and a coarser grid ( $\Delta = 8dx$ ), eight times

## D2.3 - Report on simulation framework for H<sub>2</sub>/O<sub>2</sub> and H<sub>2</sub>/air combustion

coarser. Both LESs and DNSs are performed using the same code and numerics, ensuring that the uncertainties arising from differing numerical methods or grid types are negligible.

The first configuration is analogous to the lean hydrogen/air jet flame, previously described in Section 4.2 and reported in [7]. The LES domain is periodic in the spanwise direction, open boundary conditions are applied at the outlet in the streamwise direction, and slip conditions are imposed at the boundaries in the crosswise direction. The central jet's inlet velocities were obtained from an auxiliary fully developed turbulent channel flow simulation, while a laminar coflow was applied outside the central jet.

The finer and the coarser LESs utilized approximately 21 million and 2.6 million grid points, respectively. Both simulations were run for a sufficient number of steps to ensure convergence of the time-averaged fields. A comparison of the instantaneous water mass fraction and mixture fraction contour plots obtained from the DNS and the two LESs at different resolutions is shown in Figure 35.

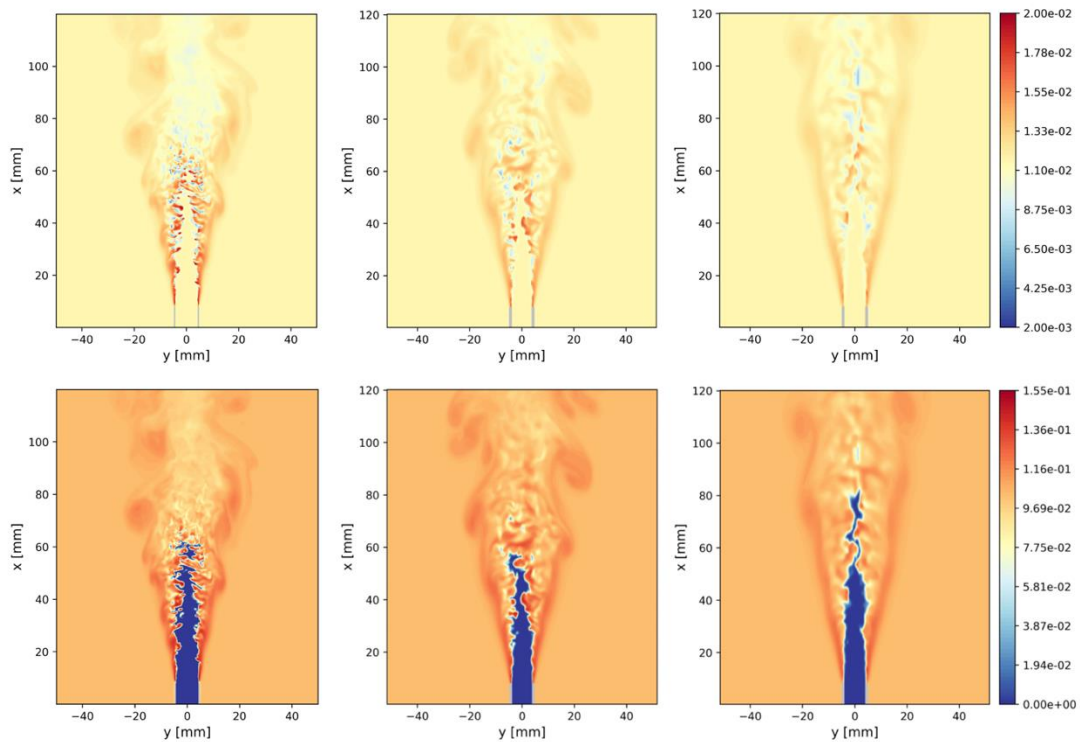


Figure 35. Instantaneous of the mixture fraction (top) and water mass fraction (bottom) contour plots. From left to right: DNS, LES with finer grid, and LES with coarser grid.

Model A successfully captures both mixture fraction fluctuations and the presence of super-adiabatic zones due to preferential diffusion. The general flame morphology is also well represented. As expected, the fluctuations range reduces as the grid resolution decreases.

A more quantitative comparison is provided in Figure 36 and Figure 37. Figure 36 shows the time-averaged temperature and water mass fraction contour plots while Figure 37 shows the mean water mass fraction, velocity, and temperature profile along the lateral direction  $y$  at different heights. For a consistent comparison, the DNS data were Favre-averaged using the definition given in Section 3.3. The results indicate an excellent agreement between LES and DNS for both LES grid resolutions across all quantities considered. The only noticeable discrepancy occurs near the flame tip, where the coarser LES ( $\Delta = 8dx$ ) predicts a slightly longer and less rounded flame. This observation is confirmed by analyzing the axial water flux along the streamwise direction, calculated as:

$$\mathcal{F} = \frac{1}{\mathcal{F}_{out}} \int \langle \rho u Y_{H_2O} \rangle dA,$$

## D2.3 - Report on simulation framework for H<sub>2</sub>/O<sub>2</sub> and H<sub>2</sub>/air combustion

where the operator  $\langle \dots \rangle$  represents averaging in time and  $\rho$ ,  $u$ , and  $Y_{H_2O}$  are the local density, axial velocity, and water mass fraction. The water flux is normalized by its value at the outlet  $\mathcal{F}_{out}$  and is presented in Figure 38.

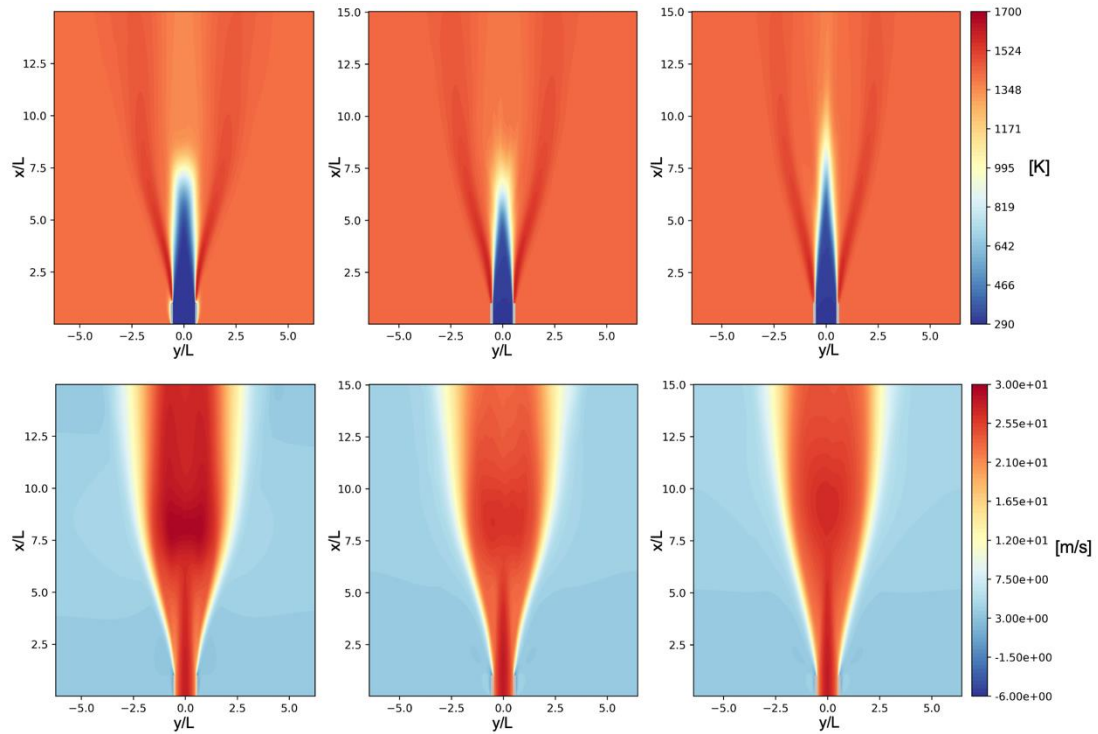


Figure 36. Averaged fields comparison. Top: Temperature. Bottom: axial velocity. From left to right: DNS, LES with finer grid and LES with coarser grid. Here the coordinates are normalized by the slot width.

The normalized flame length is then determined as the axial location where  $\mathcal{F} = 0.99$ , divided by the slot width  $L$ . The flame lengths  $L_f$  for the DNS and LESs are as follows:

- DNS:  $L_f = 8.89$
- LES ( $\Delta = 4dx$ ):  $L_f = 9.19$
- LES ( $\Delta = 8dx$ ):  $L_f = 10.67$

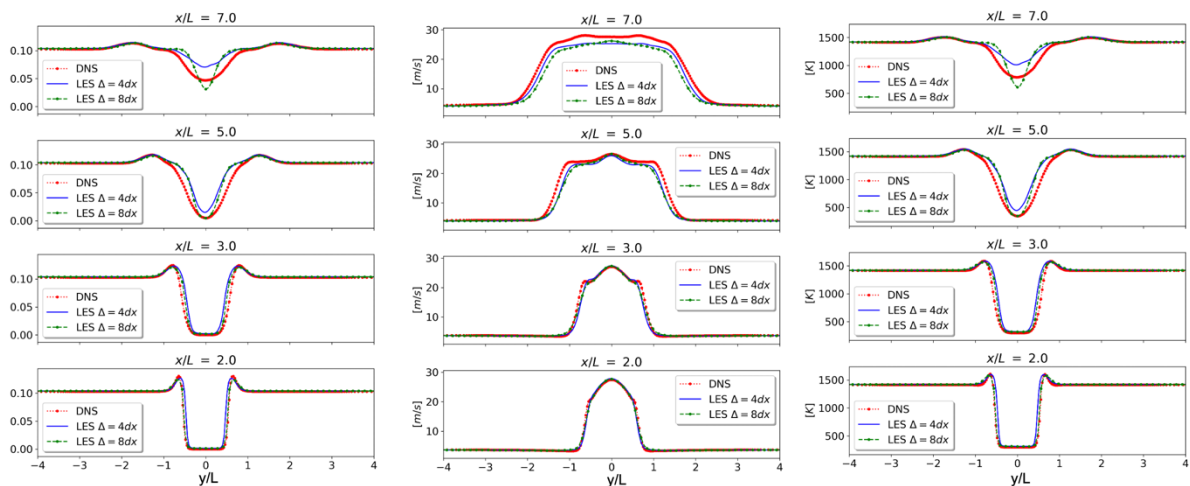


Figure 37. Comparison of averaged water mass fraction (left), axial velocity (middle), and temperature (right) at different axial quotas. Here the coordinates are normalized by the slot width.

The second configuration maintains the same Reynolds number and equivalence ratio as for the configuration above, with the only difference being a turbulent round-jet hydrogen flame. The premixed jet has a diameter

### D2.3 - Report on simulation framework for H<sub>2</sub>/O<sub>2</sub> and H<sub>2</sub>/air combustion

$L$  of 8 mm, with burned gases used as the coflow. Equivalent boundary conditions as the first configuration were applied.

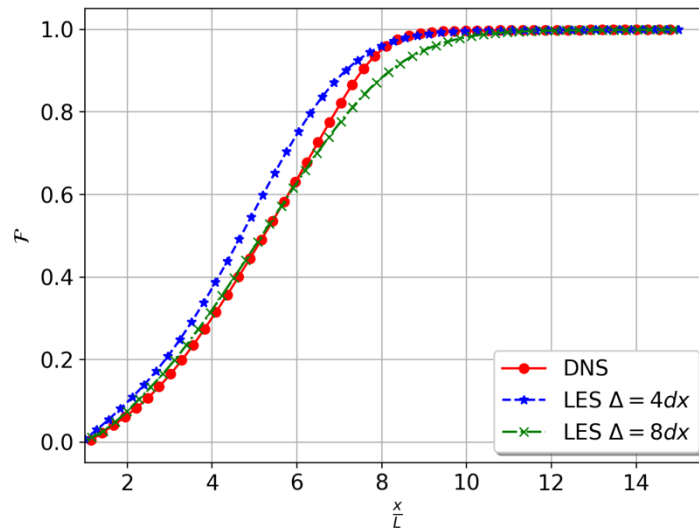


Figure 38. Normalized axial water flux for the slot burner configuration.

For this configuration, the finer and the coarser LESs employed approximately 16 million and 2 million grid points, respectively. Although the reference DNS is not fully converged, the available data is sufficient for assessing the axial water flux and estimating the flame length. The normalized axial water flux for the DNS and LESs is presented in Figure 39. The flame lengths, calculated as before, are:

- DNS:  $L_f = 7.29$
- LES ( $\Delta = 4dx$ ):  $L_f = 7.68$
- LES ( $\Delta = 8dx$ ):  $L_f = 8.99$

The results from both configurations demonstrate the capability of Model A to provide accurate predictions of key combustion metrics in turbulent settings. The LESs, even at coarser resolutions, capture critical features such as mixture fraction fluctuations, super-adiabatic zones, and flame morphology. The flame lengths predicted by Model A are in good agreement with DNS reference values, affirming the model's reliability and robustness for practical turbulent combustion scenarios. Additional analyses and Model A's performance at different Reynolds and Karlovitz numbers will be the subject of a journal publication currently in preparation.

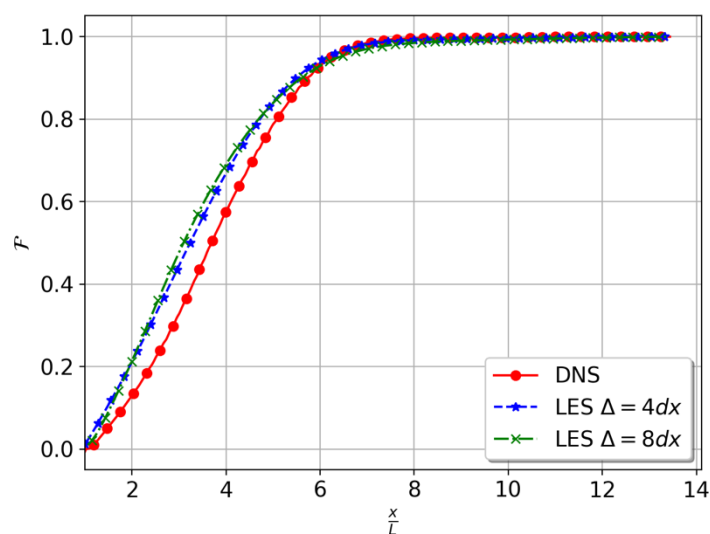


Figure 39. Normalized axial water flux for the round burner configuration.

### 4.5 LES of a turbulent jet diffusion flame using the FPVA

The performance of a state-of-the-art combustion model, namely the FPVA [19] is evaluated through an additional LES of a three-dimensional jet diffusion flame. Similarly to the previous configurations, the simulation utilized the RWTH-ITV's in-house software, CIAO, and the experimental data from Section 2.2 for validation. The setup consists of a round-jet turbulent methane/hydrogen lifted flame, simulated on a grid comprising 6 million points.

The fuel is injected through an inner nozzle with a diameter of 2.5 mm at a bulk velocity of 185 m/s, surrounded by an oxidizer coflow with a velocity of 3 m/s. The oxidizer is pure air and the Reynolds number is 11000. The combustion model employed is FPVA [19], where the progress variable is defined as the sum of the mass fractions of water, carbon dioxide, and carbon monoxide.

A key metric in this configuration is the flame lift-off height, experimentally measured as 42 mm from the nozzle edge (Figure 3). While the simulation is still ongoing, preliminary results indicate that the LES successfully predicts a lifted flame, as illustrated by the progress variable snapshot in Figure 40. This confirms that the FPVA model captures this critical flame dynamic.

Further analysis of the flame lift-off behavior, including additional comparisons between simulation and experimental data, is planned for a forthcoming journal publication, currently under preparation.

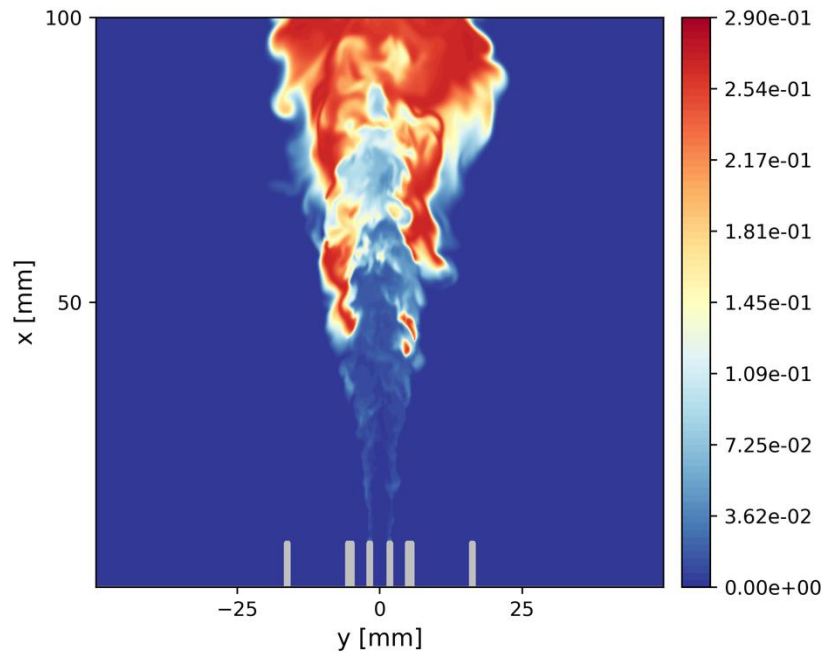


Figure 40. Instantaneous progress variable contour plot of the round-jet turbulent lifted flame configuration.

# 5 RANS simulations framework

As previously mentioned, tabulated chemistry combustion models are an excellent choice for simulating combustion systems due to their reduced computational cost. Combined with RANS turbulence modeling, they enable the simulation of complex industrial systems with multiple burners and large combustion chambers. The reduced computational cost is achieved through order reduction, wherein the combustion process is represented by a small number of control variables transported with the flow. This approach eliminates the need to transport multiple species and use complex chemical mechanisms during the simulation. Tabulated chemistry models, such as FPVA and FGM, were originally developed under the assumption of a unity Lewis number, implying that all chemical species were considered to have the same mass diffusion coefficient as the thermal diffusion coefficient [8] [19]. However, this simplified approach becomes inadequate for fuels with pronounced preferential diffusion effects, such as hydrogen, where species diffuse at significantly different rates than heat. To address this, several approaches have been developed to include preferential diffusion effects in tabulated chemistry models. These approaches involve introducing additional controlling variables, such as the mixture fraction, enthalpy, or curvature, to account for changes in local conditions caused by preferential diffusion effects, leading to the creation of multidimensional tables [14] [15] [40] [41]. Transport equations for the controlling variables must be derived, incorporating additional terms to address preferential diffusion. The literature explores various levels of complexity for this purpose, including effective Lewis numbers [42], constant non-unity species Lewis numbers [43] [44], and mixture-average diffusion [26], as in the models described in Chapter 3.

Within the framework of RANS turbulence modeling, limited research has investigated the use of tabulated chemistry combustion models that account for preferential diffusion [45] [46]. In this sub-task, the tabulated chemistry combustion models introduced in Chapter 3 are integrated into the RANS simulation framework to assess their performance and examine the impact of preferential diffusion on the modeling of hydrogen turbulent flames. This section focuses on the implementation and evaluation of Model B. Model A is still under implementation for RANS simulations, but similarly, promising results are expected based on its successful evaluation in LES.

## 5.1 Implementation of the tabulated-chemistry combustion model with preferential diffusion in commercial CFD software

In the HyInHeat project, the numerical simulations in the RANS framework are mainly performed employing the pressure-based solver of the commercial software ANSYS-Fluent [47]. The software ANSYS-Fluent provides various tabulated-chemistry combustion models based on the unity-Lewis assumption. The models considering preferential diffusion are implemented through user-defined functions (UDFs) code in C language [48].

As outlined in Chapter 3, tabulated chemistry combustion models involve two main steps. First, a set of flamelets is computed, and the thermo-chemical variables—such as temperature, species concentrations, and mixture properties—are tabulated in look-up tables as functions of the control variables. Second, transport equations for the control variables are derived and solved within the computational fluid dynamics (CFD) simulations, while the thermo-chemical states are retrieved from the look-up tables.

The flamelets are computed using one-dimensional, freely propagating (unstretched) flames with detailed chemistry, including preferential diffusion. For Model B, preferential diffusion effects are accounted for through mixture-averaged diffusion. The resulting tables are stored as plain `.dat` text files and loaded into Fluent via the UDF. The UDF reads the tables using multi-linear interpolation based on the local values of the control variables transported in the CFD simulation. The FGM model from the “Partially Premixed Combustion” package in Fluent serves as the base infrastructure for transporting control variables such as progress variable  $Y_c$ , mixture fraction  $Z$ , and enthalpy  $h$ , while the table look-up process is replaced by the UDF using the `DEFINE_PDF_TABLE` macro.

## D2.3 - Report on simulation framework for H<sub>2</sub>/O<sub>2</sub> and H<sub>2</sub>/air combustion

The transport equations for the control variables are modified to include additional diffusion terms arising from the inclusion of PD effects. These diffusion terms are computed by the UDF at the beginning of each numerical iteration using the `DEFINE_ADJUST` macro and they are incorporated as source terms in the transport equations via the `DEFINE_SOURCE` macro.

### 5.1.1 Laminar configuration

The adiabatic laminar version of the Model B is implemented and evaluated first. For this case, only two control variables are required: the progress variable  $Y_c$  and the mixture fraction  $Z$ . The transport equations for these control variables are summarized in Table 5 both for the unity-Lewis assumption and for the case that incorporates preferential diffusion with mixture-averaged diffusion. The difference in the transport equations lies in the diffusion terms. Under the unity-Lewis assumption, the diffusion of both control variables is proportional to a single diffusion coefficient, equal to the thermal diffusivity of the gas mixture. In contrast, preferential diffusion results in multiple diffusion coefficients, where the diffusion of one control variable is influenced by gradients of the other control variables. The diffusion coefficients  $\Gamma_{x,y}$  are computed from the flamelets and included in the tables as a function of the control variables.

Unity Lewis	Preferential diffusion
$\rho \frac{\partial Y_c}{\partial t} + \rho \vec{u} \cdot \nabla Y_c = \nabla \cdot (\rho D_{th} \nabla Y_c) + \rho \dot{\omega}_c$	$\rho \frac{\partial Y_c}{\partial t} + \rho \vec{u} \cdot \nabla Y_c = \nabla \cdot (\rho \Gamma_{Y_c, Y_c} \nabla Y_c + \rho \Gamma_{Y_c, Z} \nabla Z) + \rho \dot{\omega}_c$
$\rho \frac{\partial Z}{\partial t} + \rho \vec{u} \cdot \nabla Z = \nabla \cdot (\rho D_{th} \nabla Z)$	$\rho \frac{\partial Z}{\partial t} + \rho \vec{u} \cdot \nabla Z = \nabla \cdot (\rho \Gamma_{Z, Y_c} \nabla Y_c + \rho \Gamma_{Z, Z} \nabla Z)$

Table 5. Transport equations of control variables for adiabatic laminar flames.

A CFD simulation of the one-dimensional freely propagating flame (1D free-flame) is performed in Fluent using the tabulated chemistry combustion model with preferential diffusion. The numerical domain, 10 mm in length, is discretized into 800 elements along the streamwise direction, as illustrated in Figure 41. The numerical domain of the 1D-free flame in Fluent. A mixture of hydrogen and air enters through the inlet at a velocity dynamically adjusted to match the laminar flame speed, calculated as  $S_L = (u_b - u_u) / (\rho_u / \rho_b - 1)$ , where  $u$  and  $b$  represent the unburnt and burnt sides of the flame, respectively.

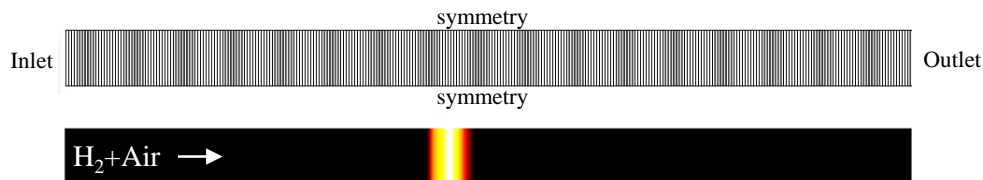


Figure 41. The numerical domain of the 1D-free flame in Fluent.

The results for the laminar flame speed and thermal flame thickness from the 1D free-flame simulation in Fluent are shown in Figure 42. These results are presented for both the tabulated chemistry combustion model with preferential diffusion (FGM – PD) and the unity Lewis number assumption (FGM – Unity Lewis). The results obtained using the chemical kinetics software Cantera with detailed chemistry and mixture-averaged diffusion (DC Mix) are included as a reference. The FGM – PD model accurately predicts both the laminar flame speed and flame thickness, whereas the unity Lewis assumption results in noticeable discrepancies. For the unity Lewis model, the laminar flame speed is underpredicted for mixtures with an equivalence ratio above 0.6 and slightly overpredicted for equivalence ratios below 0.6, while the flame thickness is consistently underpredicted across the entire range.

## D2.3 - Report on simulation framework for H<sub>2</sub>/O<sub>2</sub> and H<sub>2</sub>/air combustion

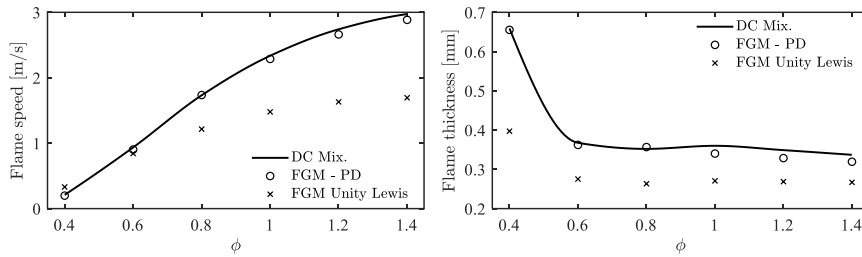


Figure 42. Laminar flame speed and thermal flame thickness.

The internal structure of the flame is also accurately predicted when preferential diffusion is accounted for using the FGM – PD model, as demonstrated by the profiles of equivalence ratio, temperature, and hydrogen mole fraction across the flame. The decrease in the equivalence ratio within the flame, caused by the differential diffusion of hydrogen and hydrogen-containing radicals, is successfully captured by the FGM – PD model. These results validate the implementation of the adiabatic laminar version of the tabulated chemistry model with preferential diffusion in Fluent.

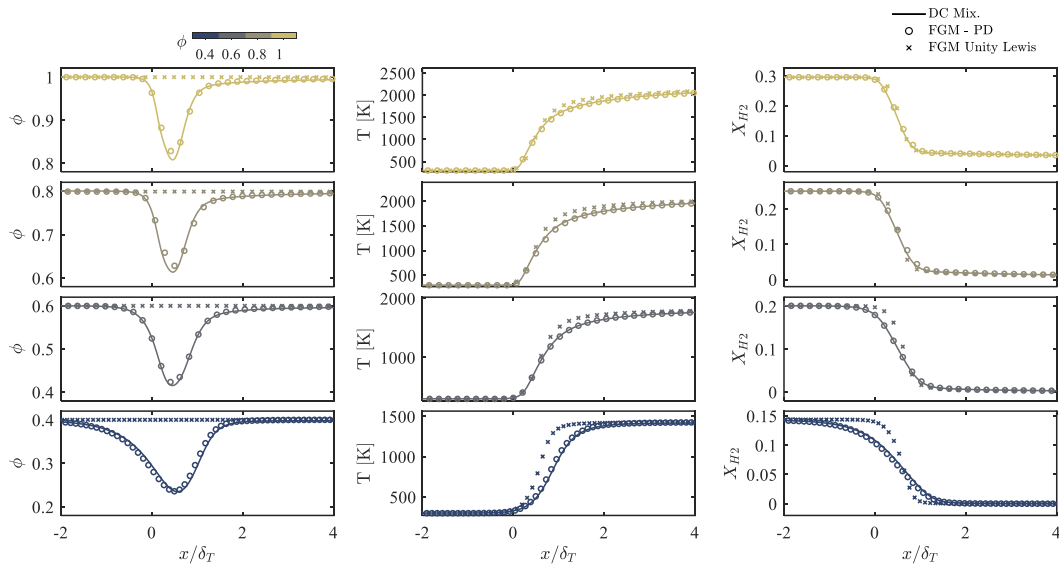


Figure 43. Profiles of equivalence ratio, temperature, and H<sub>2</sub> mole fraction across the 1D free-flame. The position  $x$  equal to zero is located at the point of temperature rise.

### 5.1.2 Turbulent configuration

As described in Section 3.6, two additional control variables are required to describe the turbulent combustion process, in the case of LES turbulent modeling: the variances of the progress variable ( $Y_{c,v}$ ) and the mixture fraction ( $Z_v$ ). The transport equations for all four control variables used in modeling an adiabatic turbulent flame within the RANS turbulent modeling framework are listed in Table 6, where the overbar represents the Favre average. Turbulent diffusion is modeled using a turbulent Schmidt number ( $Sc_t$ ) of 0.7, while the scalar dissipation rates of the control variable variances are assumed to be proportional to the ratio of the turbulent dissipation rate to the turbulent kinetic energy ( $\epsilon/\kappa$ ). The constant of proportionality  $C_d$  is set to 1 for the mixture fraction and 6 for the progress variable.

## D2.3 - Report on simulation framework for H<sub>2</sub>/O<sub>2</sub> and H<sub>2</sub>/air combustion

$\rho \frac{\partial \bar{Y}_c}{\partial t} + \rho \bar{\mathbf{u}} \cdot \nabla \bar{Y}_c = \nabla \cdot (\rho \Gamma_{Y_c, Y_c} \nabla \bar{Y}_c + \rho \Gamma_{Y_c, Z} \nabla \bar{Z}) + \rho \dot{\omega}_c$
$\rho \frac{\partial \bar{Z}}{\partial t} + \rho \bar{\mathbf{u}} \cdot \nabla \bar{Z} = \nabla \cdot (\rho \Gamma_{Z, Y_c} \nabla \bar{Y}_c + \rho \Gamma_{Z, Z} \nabla \bar{Z}) + \nabla \cdot \left( \rho \frac{\nu_t}{Sc_t} \nabla \bar{Z} \right)$
$\rho \frac{\partial Y_{c,v}}{\partial t} + \rho \bar{\mathbf{u}} \cdot \nabla Y_{c,v} = \nabla \cdot \left( \rho \Gamma_{Y_c, Y_c} + \rho \frac{\nu_t}{Sc_t} \right) \nabla Y_{c,v} + 2\rho \frac{\nu_t}{Sc_t} \nabla \bar{Y}_c \cdot \nabla \bar{Y}_c - 2\rho C_{d,c} \frac{\epsilon}{\kappa} Y_{c,v} + 2\rho (\bar{Y}_c \bar{\omega}_c - \bar{Y}_c \bar{\omega}_c)$
$\rho \frac{\partial Z_v}{\partial t} + \rho \bar{\mathbf{u}} \cdot \nabla Z_v = \nabla \cdot \left( \rho \Gamma_{Z, Z} + \rho \frac{\nu_t}{Sc_t} \right) \nabla Z_v + 2\rho \frac{\nu_t}{Sc_t} \nabla \bar{Z} \cdot \nabla \bar{Z} - 2\rho C_{d,z} \frac{\epsilon}{\kappa} Z_v$

Table 6. RANS transport equations of control variables for adiabatic turbulent flames.

The transport equations for  $Y_{c,v}$  and  $Z_v$  differ slightly from those solved natively in Fluent, so the transport equations have been implemented in the CFD solver using User-Defined Scalars (UDS). The corresponding laminar and turbulent diffusion coefficients were specified using the `DEFINE_DIFFUSIVITY` macro, while the respective source and dissipation terms were incorporated as source terms using the `DEFINE_SOURCE` macro.

As in the LES case, the turbulent-chemistry interaction is accounted for using a presumed PDF approach, assuming statistical independence between the progress variable and the mixture fraction. Every thermochemical state quantity, including the diffusion coefficients  $\Gamma_{x,y}$ , is stored in the look-up tables as a function of the four control variables:  $\bar{Z}$ ,  $Z_v$ ,  $\bar{Y}_c$ , and  $Y_{c,v}$ . These values are then read and interpolated by the UDF during the CFD simulation. The control variables are normalized, as described in Section 3.6, to create an orthogonal grid manifold ranging from 0 to 1 in all dimensions.

## 5.2 RANS simulations of H<sub>2</sub>-air lean premixed flame

The performance of the tabulated-chemistry combustion model with preferential diffusion in the RANS framework is first evaluated against the DNS of the turbulent fully premixed hydrogen-air flame as done for the LESs in Chapter 3. The analysis considers a round jet and slot jet flame with a Reynolds of 11000 and an equivalence ratio of 0.4 for both the round jet flame and the slot jet flame. The jet diameter and the slot width are equal to 8 mm. Figure 44 presents contours of the instantaneous temperature and equivalence ratio for both geometries.

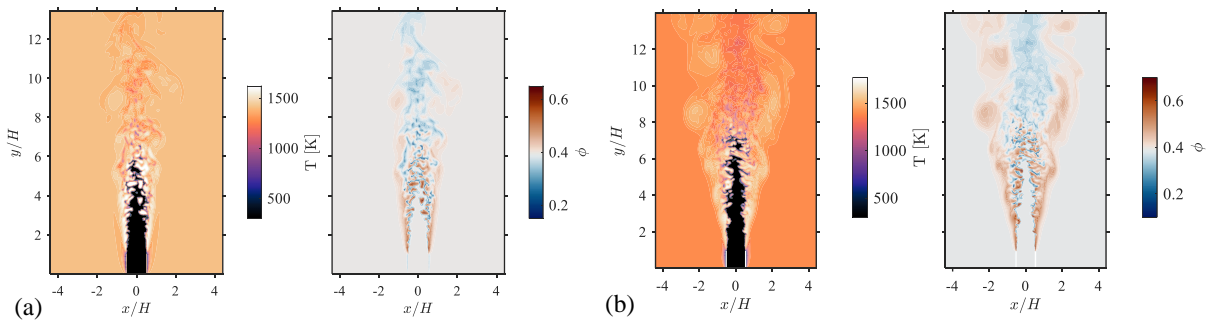


Figure 44. DNS instantaneous temperature and equivalence ratio for (a) the round jet flame and (b) the slot jet flame.

The RANS simulations are conducted using ANSYS Fluent version 2023-R1. The pseudo-time-stepping coupled scheme is employed for pressure-velocity coupling, with pressure interpolation handled using the PRESTO! algorithm [49]. A Second-Order Upwind spatial discretization scheme is applied for all transport equations. The Reynolds stress tensor in the RANS transport equations is calculated based on the Boussinesq hypothesis using the  $\kappa$ - $\omega$  turbulence model [50]. The round and slot jet flames are simulated using a two-dimensional domain, as illustrated in Figure 45, with the axisymmetric formulation applied for the round jet

## D2.3 - Report on simulation framework for H<sub>2</sub>/O<sub>2</sub> and H<sub>2</sub>/air combustion

flame. The domain is discretized using a structured mesh of quadrilateral elements, with element sizes ranging from 0.1 mm to 0.6 mm.

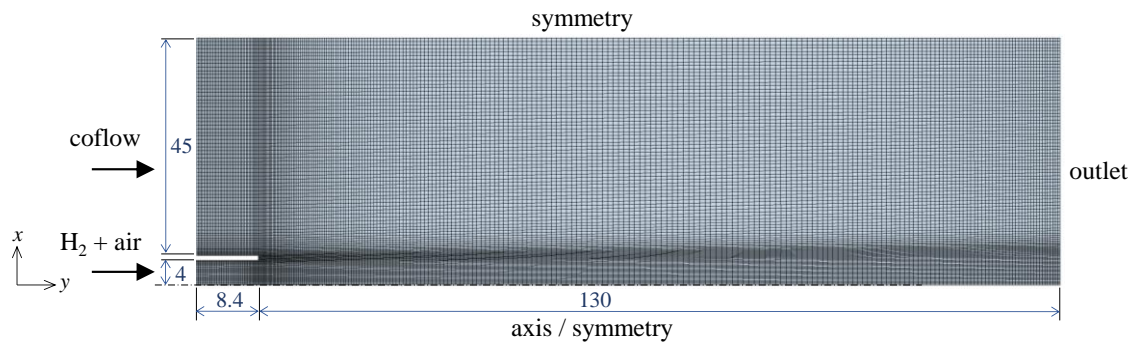


Figure 45. Example of the numerical domain for the RANS simulations. Dimensions in mm.

A fully premixed hydrogen-air mixture enters the central jet with a velocity profile fitted to the DNS time-averaged data using a power-law, as shown in Figure 46. Surrounding the central jet is a coflow of burnt gases from the same mixture, flowing at a velocity of 3.6 m/s. A turbulence intensity of 10% is imposed on the central jet inlet, and 0% at the coflow.

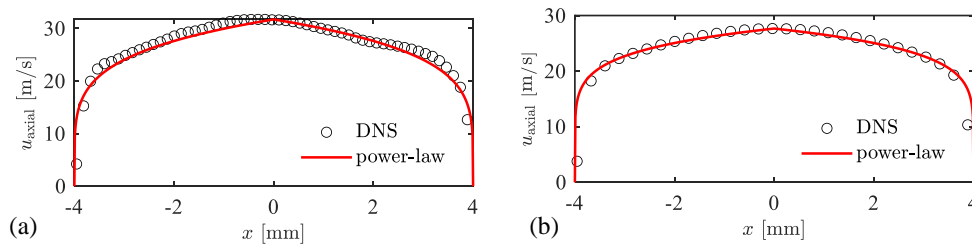


Figure 46. Central jet velocity profile for (a) the round jet flame and (b) the slot jet flame.

### 5.2.1 Hydrogen-air lean premixed round jet flame

The results of the RANS simulations for the round jet flame are presented in Figure 47, compared against the time-averaged fields from the DNS. The flame length predicted by the RANS simulations shows good agreement with the DNS, as evidenced by the contours of heat release rate and hydrogen mass fraction. The tabulated chemistry model with preferential diffusion successfully captures the increase in equivalence ratio at the shear layer of the round jet and its subsequent decrease downstream of the flame tip, attributed to the convection-diffusion balance under the influence of species differential diffusion. Additionally, the RANS simulations accurately predict the temperature distribution, including regions of super adiabatic temperature caused by the elevated flame temperature at the zones of richer equivalence ratios due to preferential diffusion.

## D2.3 - Report on simulation framework for H<sub>2</sub>/O<sub>2</sub> and H<sub>2</sub>/air combustion

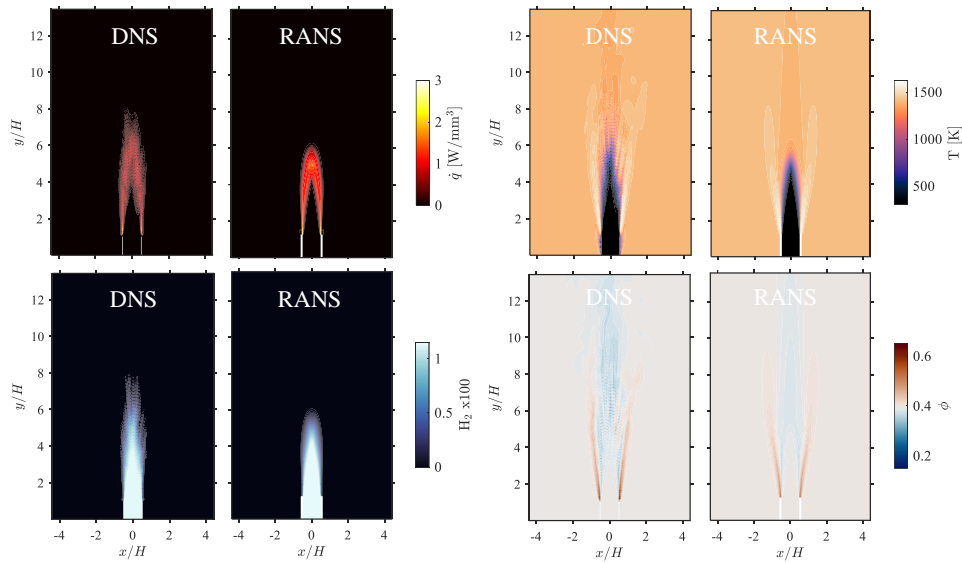


Figure 47. Contours of heat release rate, hydrogen mass fraction, equivalence ratio, and temperature for the round jet flame from the DNS Favre-averaged data and the RANS data.

Figure 48 presents the profiles of temperature, equivalence ratio, heat release rate, and axial velocity at various axial positions. The comparison between the RANS simulation results and DNS data shows good agreement. The peak values of temperature and equivalence ratio in the flame's shear layer, influenced by preferential diffusion, are accurately captured, despite the finer details of the flame not being fully resolved in the RANS simulations. The profiles of heat release rate and axial velocity effectively predict the flame length and jet spreading angle. These results demonstrate the potential of the tabulated chemistry model in the RANS framework to capture combustion key features of lean premixed hydrogen-air flames in a round jet configuration.

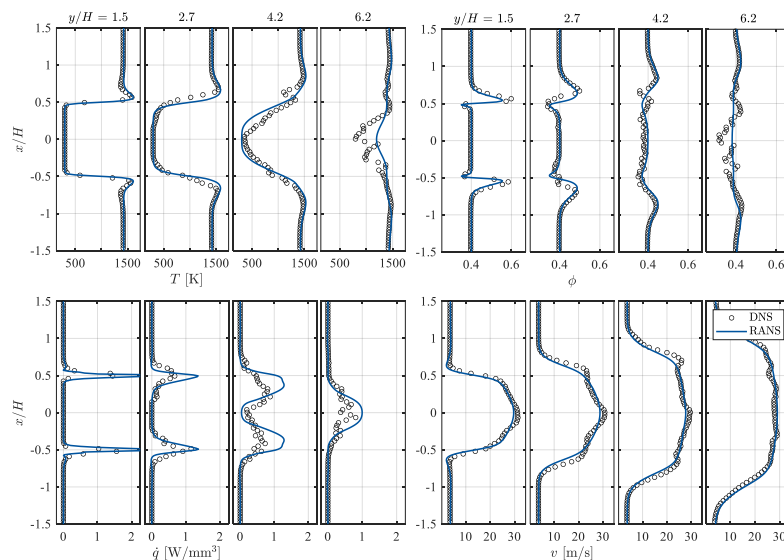


Figure 48. Profiles of temperature, equivalence ratio, heat release rate, and axial velocity for the round jet flame DNS Favre-averaged data and the RANS data.

To evaluate the impact of including preferential diffusion in the tabulated chemistry model within the RANS framework, the results of the RANS simulation using the unity Lewis assumption are presented in Figure 49(d). Compared to the DNS results and the RANS simulation with preferential diffusion, the flame length is approximately twice as long under the unity Lewis assumption. This discrepancy arises despite the good

## D2.3 - Report on simulation framework for H<sub>2</sub>/O<sub>2</sub> and H<sub>2</sub>/air combustion

prediction of the laminar flame speed for 1D flames under the unity Lewis assumption, as shown in Figure 42. The difference is likely attributed to the influence of preferential diffusion on the turbulence-chemistry interaction, modeled here using the presumed  $\beta$ -PDF.

An additional case is presented in Figure 49(c) where preferential diffusion is accounted for in the computation of the flamelets used to build the PDF tables but not in the transport equations of the control variables (i.e., the transport equations are the same as those under the unity Lewis assumption). In this case, the predicted flame length is closer to the DNS results compared to the value predicted under the unity Lewis assumption. However, since preferential diffusion is not included in the transport equations, the additional diffusion terms are absent, leading to inaccuracies in the predicted temperature and species fields, as demonstrated by the temperature and equivalence ratio contours.

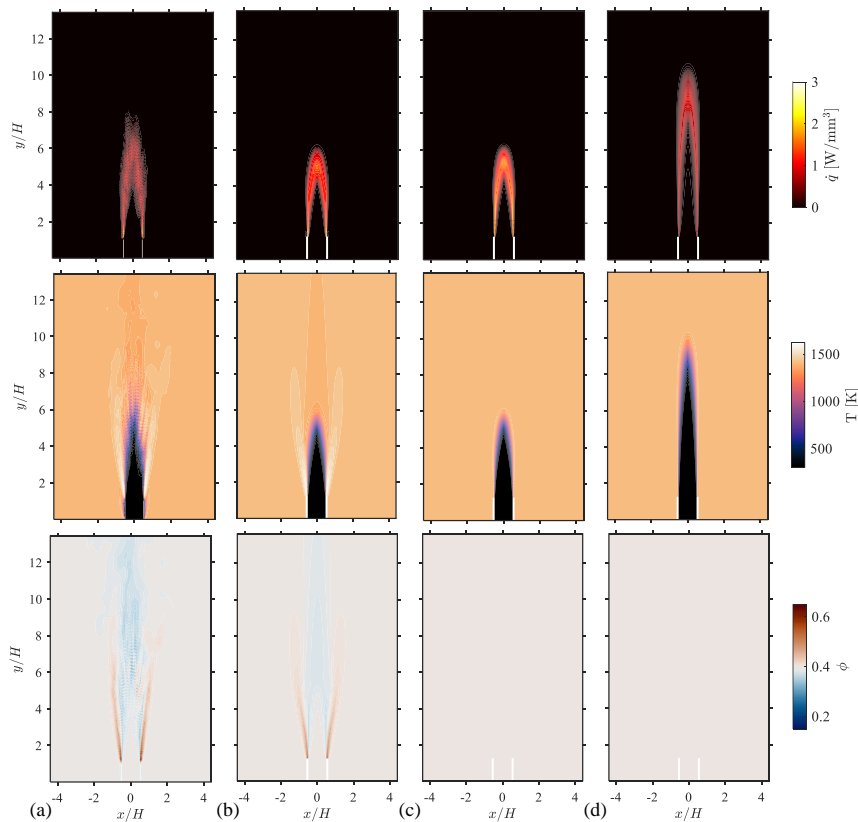


Figure 49. Contours of heat release rate, temperature, and equivalence ratio for the round jet flame from (a) the DNS Favre-averaged data and (b) the RANS with preferential diffusion in the flamelets and transport equations, (c) the RANS with preferential diffusion only in the flamelets, and (d) the RANS with unity Lewis assumption.

### 5.2.2 Hydrogen-air lean premixed slot jet flame

The results of the RANS simulations for the slot jet flame are presented in Figure 50. The flame is longer than the round jet flame for the same Reynolds number due to the absence of spreading in the out-of-plane direction. The RANS simulation predicts the flame shape reasonably well compared to the DNS. The increase

## D2.3 - Report on simulation framework for H<sub>2</sub>/O<sub>2</sub> and H<sub>2</sub>/air combustion

in equivalence ratio and temperature within the shear layer is more pronounced in the slot jet flame, and this behavior is captured by the RANS simulation using the tabulated chemistry model with preferential diffusion.

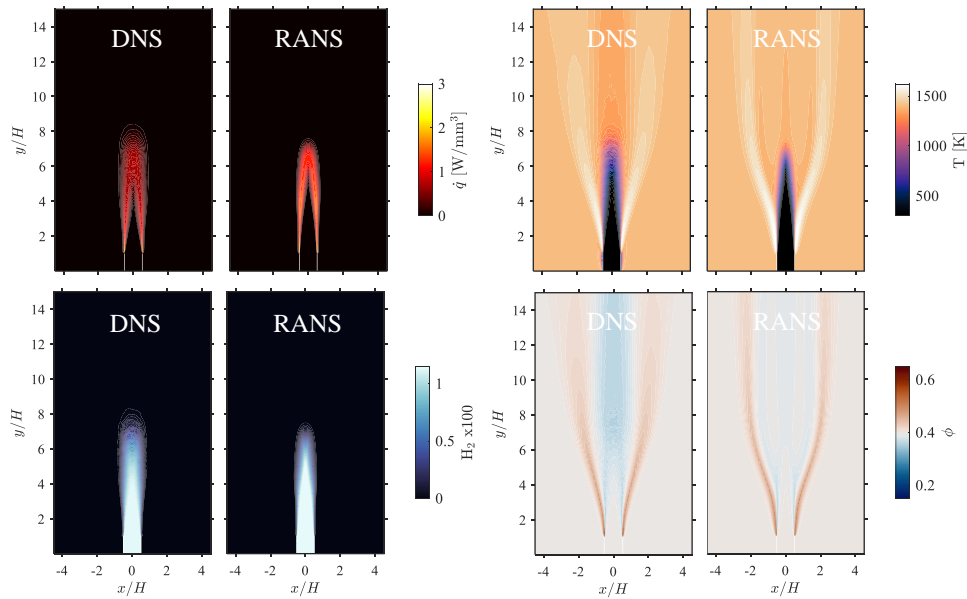


Figure 50. Contours of heat release rate, hydrogen mass fraction, equivalence ratio, and temperature for the slot jet flame from the DNS Favre-averaged data and the RANS data.

The quantitative comparison in Figure 51 indicates a slightly longer flame in the DNS, based on the heat release rate profiles. Nevertheless, the RANS results are in close agreement with the DNS. The minor discrepancy may stem from uncertainties in the turbulence modeling, particularly related to the turbulent round-jet/plane-jet anomaly, where the empirical constants of the model may not be universally applicable to all cases. Consequently, the results of the RANS simulations could potentially be improved by adjusting the turbulence model parameters. Nevertheless, the agreement between the RANS and DNS data is remarkable, highlighting the strengths of the developed tabulated chemistry combustion model.

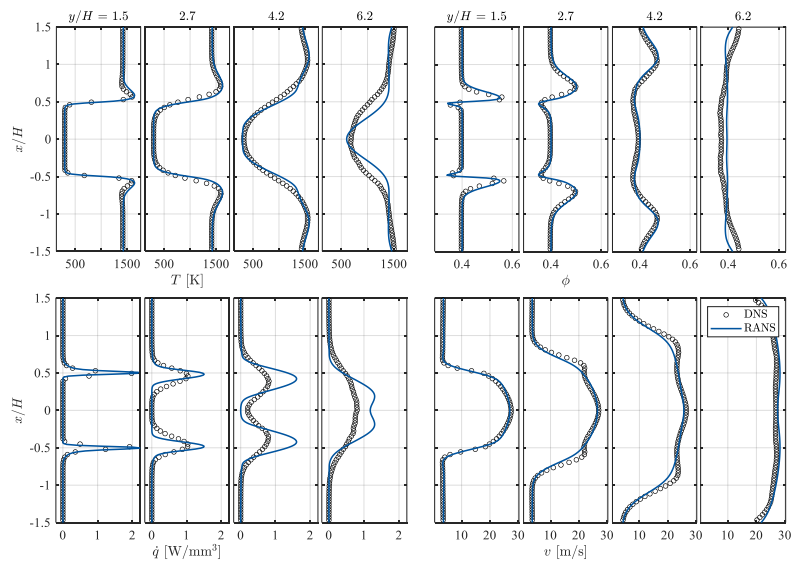


Figure 51. Profiles of temperature, equivalence ratio, heat release rate, and axial velocity for the slot jet flame DNS Favre-averaged data and the RANS data.

### 5.3 RANS simulations of non-premixed turbulent jet flame

Numerical simulations of the turbulent jet flame described in Chapter 2 are performed with the tabulated chemistry model in the RANS framework. The configuration corresponds to a diffusion flame, where the fuel is injected in a non-premixed manner and surrounded by two coflows of air at a speed of 3 m/s. Additionally, an outer shielding coflow flows at a speed of 0.1 m/s. The fuel consists of a CH<sub>4</sub>-H<sub>2</sub> mixture with 80% H<sub>2</sub> by volume. Two fuel flow rates are considered, corresponding to Reynolds numbers of 10000, and 14000. The numerical setup is the same as that described in Section 5.2 for the fully premixed turbulent flame. A two-dimensional axisymmetric domain is used, discretized with 97000 quadrilateral elements, featuring a characteristic element size of about 0.2 mm in the reaction zone.

As already discussed, preferential diffusion effects are particularly significant in lean premixed flames of low Lewis number fuels, such as hydrogen, where molecular diffusion strongly influences the flame structure and propagation. However, preferential diffusion effects are generally less dominant in non-premixed flames since combustion occurs in the mixing layer, where turbulent mixing plays a major role. Consequently, combustion models based on the unity Lewis number assumption have historically provided good agreement with experimental data in these configurations. Nevertheless, accounting for preferential diffusion effects may still impact the behavior of non-premixed flames. Since non-premixed combustion is primarily governed by the dynamics of the stoichiometric mixing layer, accurate diffusion modeling can affect mixing processes, thereby altering the species distribution and the precise location of the stoichiometric mixture fraction. This, in turn, can shift the flame position and influence localized phenomena such as extinction and reignition [51] [52].

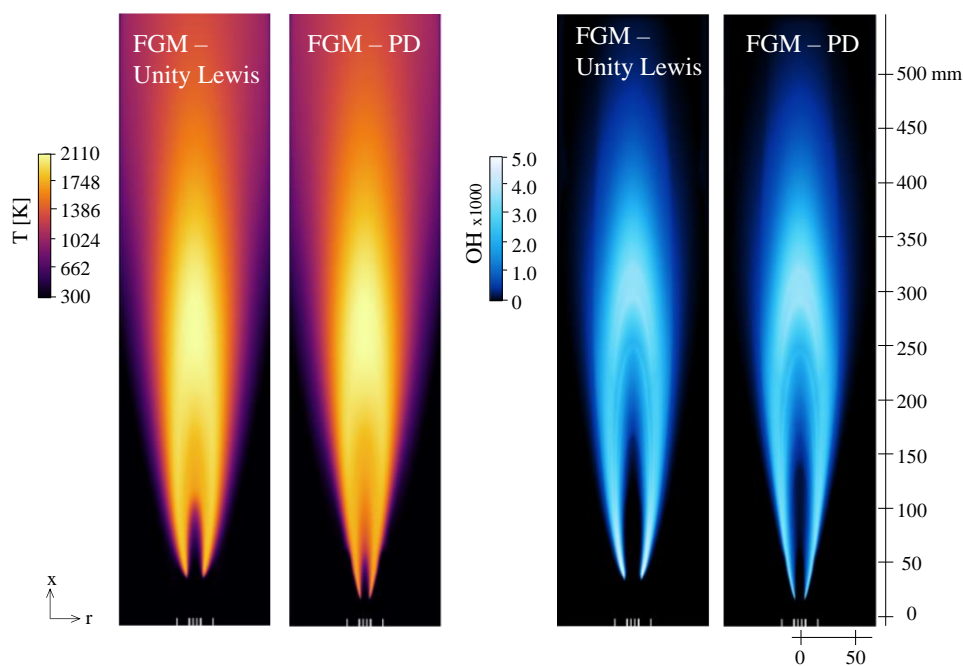


Figure 52. Contours of temperature and OH mole fraction for the diffusion jet flame with  $Re=14000$ , obtained from RANS simulations comparing tabulated chemistry with Unity Lewis and preferential diffusion (FGM-PD).

Figure 52 presents the temperature and OH mole fraction contours for the diffusion flame with a Reynolds number of 14000, comparing the flame structures predicted using the unity Lewis number assumption and preferential diffusion. The case with preferential diffusion shows a slightly upstream flame position, closer to the nozzle. This shift corresponds to the higher diffusivity of hydrogen relative to other reactant species, which causes a displacement of the reaction zone. Differential diffusion effects are more pronounced near the burner nozzle where the flow is less turbulent and molecular diffusion has a relatively higher impact. Further downstream, turbulence mixing becomes predominant in non-premixed flames, decreasing diffusion

## D2.3 - Report on simulation framework for H<sub>2</sub>/O<sub>2</sub> and H<sub>2</sub>/air combustion

effects. Consequently, the differences between the two flames are less pronounced compared to the premixed configuration.

Figure 53 shows the mixture fraction profiles along the flame central axis and radial axis at heights of 38.8 mm, 41.2 mm, and 46.9 mm for Reynolds numbers 7000, 10000, and 14000, respectively. The results from the RANS simulations are compared with experimental data. While the case accounting for preferential diffusion better captures the physics of hydrogen diffusion, it predicts a flame anchored further upstream and, therefore, underestimates radial mixing. In contrast, the unity Lewis assumption predicts a smaller lift-off height, aligning more closely with the measured profiles. This improved match does not suggest that hydrogen behaves as it had a unity Lewis number. Instead, it reflects the dominance of turbulent mixing in non-premixed flames and highlights how, in a RANS framework, simpler diffusion assumptions may sometimes compensate for other modeling uncertainties—such as those related to turbulence models or boundary conditions—leading to an apparent closer match with experimental data.

It is also important to note that an unstretched laminar premixed flame configuration was used to compute the flamelets for the manifolds in both versions of the FGM model (unity Lewis and preferential diffusion). However, it is preferable to use flamelets that closely resemble the flame being simulated—in this case, a non-premixed (diffusion) flame [53]. As such, the RANS simulation results for the non-premixed flame could likely be improved by computing the flamelets using a stretched counterflow diffusion flame. A complementary work will further evaluate the impact of the turbulence model and the type of flamelet used to construct the manifold on the RANS simulations of non-premixed hydrogen flames with preferential diffusion.

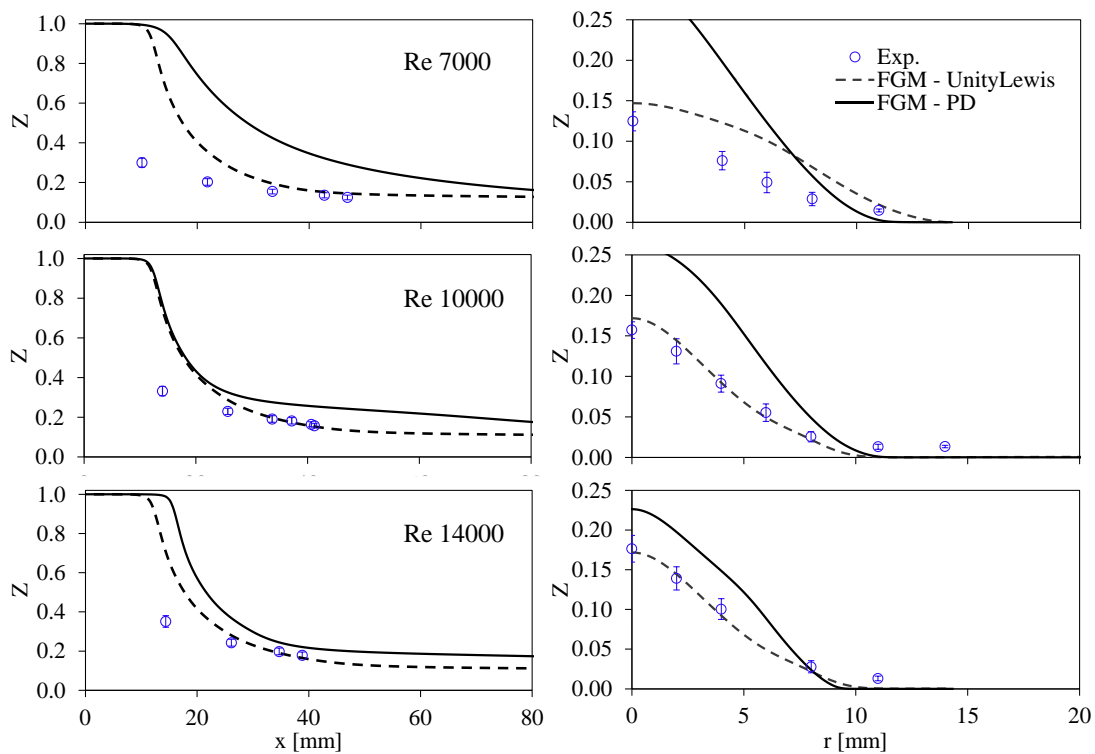


Figure 53. Mixture fraction profiles along the flame central axis (left column) and along the radial direction at experimental lift-off length (right column).

# 6 Publications & conference participation

In the following, the papers in preparation or published, fruit of the work carried out during the project, are listed:

E. Pérez-Sánchez, E. Fortes and D. Mira, "Assessment of the flamelet generated manifold method with preferential diffusion modelling for the prediction of partially premixed hydrogen flames," *Combustion and Flames*, vol. Submitted, arXiv preprint arXiv:2312.00929, 2023.

E. Fortes, E. Pérez-Sánchez, A. Both, T. Grenga and D. Mira, "Analysis of thermodiffusive instabilities in hydrogen premixed flames using a tabulated flamelet model," *International Journal of Hydrogen Energy*, vol. Submitted, arXiv preprint arXiv:2411.03526, 2024.

E. Fortes, E. Pérez-Sánchez, T. Grenga, M. Gauding, H. Pitsch and D. Mira, "Large-eddy simulations of a lean hydrogen premixed turbulent jet flame with tabulated chemistry," in *13th Mediterranean Combustion Symposium*, Submitted, 2024.

A. García, E. Fortes, E. Pérez-Sánchez, D. Mira, M. Vivenzo, M. Gauding, H. Pitsch, N. Schmitz, H. Pfeifer, "Evaluation of Preferential Diffusion in RANS Simulation of H<sub>2</sub>-Air Turbulent Flames with FGM Model" at 19th International Conference on Numerical Combustion – ICNC2024 (Kyoto, Japan), 7<sup>th</sup> – 10<sup>th</sup> May 2024.

E. Fortes, E. Pérez-Sánchez, T. Grenga, D. Mira, "Analysis of thermodiffusive fluxes in hydrogen premixed flames using flamelet generated manifolds" at 19th International Conference on Numerical Combustion – ICNC2024 (Kyoto, Japan), 7<sup>th</sup> – 10<sup>th</sup> May 2024.

E. Fortes, E. Pérez-Sánchez, A. Both, T. Grenga, D. Mira, "Tabulated chemistry analysis of thermodiffusive fluxes in premixed hydrogen flames" (poster presentation) at Combustion Institute 40th International Symposium (Milan, Italy), 21<sup>st</sup> – 26<sup>th</sup> July 2024.

E. Fortes, E. Pérez-Sánchez, D. Mira, T. Grenga, "Tabulated chemistry analysis of thermodiffusive fluxes in hydrogen premixed flames using tabulated chemistry" at the 2024 Meeting of the Spanish Section of the Combustion Institute (Madrid, Spain), 17<sup>th</sup> – 18<sup>th</sup> October 2024.

M. Vivenzo, M. Gauding, L. Berger, F. Loffredo, T. Grenga, H. Pitsch, "Analysis of an LES combustion model for lean premixed turbulent hydrogen/air flames at different Reynolds number", in preparation.

H. Xu, M. Cafiero, F. Cameron, A. Maffei, T. Howarth, M. Vivenzo, M. Gauding, J. Beeckmann, H. Pitsch, "Liftoff characteristics and stability mechanism of turbulent H<sub>2</sub>/CH<sub>4</sub> flames in air and O<sub>2</sub>-enriched coflow", in preparation.

# 7 Bibliography

- [1] R. Bilger, "The structure of diffusion flames," *Combustion Science and Technology*, vol. 13, no. 1-6, pp. 155-170, 1976.
- [2] C. Brown, K. Watson and K. Lyons, "Studies on lifted jet flames in coflow: The stabilization mechanism in the near- and far-fields," *Flow, Turbulence and Combustion*, vol. 62, p. 249–273, 1999.
- [3] T. Guiberti, W. Boyette, W. Roberts and A. Masri, "Pressure effects and transition in the stabilization mechanism of turbulent lifted flames," *Proceedings of the Combustion Institute*, vol. 37, no. 2, pp. 2167-2174, 2019.
- [4] A. Cessou, C. Maurey and D. Stepowski, "Parametric and statistical investigation of the behavior of a lifted flame over a turbulent free-jet structure," *Combustion and Flame*, vol. 137, no. 4, pp. 458-477, 2004.
- [5] D. Jeon, G. Hwang, H. Jang and N. Kim, "Lift-off characteristics of non-premixed jet flames in laminar/turbulent transition," *Combustion and Flame*, vol. 238, no. 111948, 2022.
- [6] H. Pitsch, "The transition to sustainable combustion: Hydrogen- and carbon-based future fuels and methods for dealing with their challenges," *Proceedings of the Combustion Institute*, vol. 40, 2024.
- [7] L. Berger, A. Attili and H. Pitsch, "Synergistic interactions of thermodiffusive instabilities and turbulence in lean hydrogen flames," *Combustion and Flame*, vol. 244, 2022.
- [8] J. van Oijen, F. Lammers and L. de Goey, "Modeling of complex premixed burner systems by using flamelet-generated manifolds," *Combustion and Flame*, vol. 127, no. 3, p. 2124–2134, 2001.
- [9] J. Van Oijen, A. Donini, R. Bastiaans, J. ten Thije Boonkkamp and L. De Goey, "State-of-the-art in premixed combustion modeling using flamelet generated manifolds," *Progress in Energy and Combustion Science*, vol. 57, p. 30–74, 2016.
- [10] J. de Swart, R. Bastiaans, J. van Oijen, L. de Goey and R. Cant, "Inclusion of preferential diffusion in simulations of premixed combustion of hydrogen/methane mixtures with flamelet generated manifolds," *Flow, Turbulence and Combustion*, vol. 85, p. 473–511, 2010.
- [11] P. Lapenna, R. Lamioni and F. Creta, "Subgrid modeling of intrinsic instabilities in premixed flame propagation," *Proceedings of the Combustion Institute*, vol. 38, no. 2, p. 2001–2011, 2021.
- [12] L. Berger, A. Attili, M. Gauding and H. Pitsch, "LES combustion model for hydrogen flames with thermodiffusive instabilities: A priori and a posteriori analysis," *Journal of Fluid Mechanics*, vol. Accepted for publication, 2024.
- [13] R. Bastiaans, A. Vreman and H. Pitsch, "DNS of lean hydrogen combustion with flamelet-generated manifolds," *CTR Annual Research Briefs*, p. 195–206, 2007.
- [14] A. Donini, R. Bastiaans, J. van Oijen and L. de Goey, "Differential diffusion effects inclusion with flamelet generated manifold for the modeling of stratified premixed cooled flames," *Proceedings of the Combustion Institute*, vol. 35, no. 1, p. 831–837, 2015.
- [15] N. Mukundakumar, D. Efimov, N. Beishuizen and J. van Oijen, "A new preferential diffusion model applied to FGM simulations of hydrogen flames," *Combustion Theory and Modelling*, vol. 25, no. 7, p. 1245–1267, 2021.

## D2.3 - Report on simulation framework for H<sub>2</sub>/O<sub>2</sub> and H<sub>2</sub>/air combustion

- [16] J. Regele, E. Knudsen, H. Pitsch and G. Blanquart, "A two-equation model for non-unity Lewis number differential diffusion in lean premixed laminar flames," *Combustion and Flame*, vol. 160, no. 2, p. 240–250, 2013.
- [17] J. Schlup and G. Blanquart, "Reproducing curvature effects due to differential diffusion in tabulated chemistry for premixed flames," *Proceedings of the Combustion Institute*, vol. 37, no. 2, p. 2511–2518, 2019.
- [18] L. Berger, A. Attili, J. Wang, K. Maeda and H. Pitsch, "Development of Large-Eddy Simulation Combustion Models for Thermodiffusive Instabilities in Turbulent Hydrogen Flames," *Proceeding of the Summer Program, Center for Turbulence Research*, 2022.
- [19] C. Pierce and P. Moin, "Progress-variable approach for large-eddy simulation of non-premixed turbulent combustion," *Journal of Fluid Mechanics*, vol. 504, p. 73–97, 2004.
- [20] P. Moin, K. Squires, W. Cabot and S. Lee, "A dynamic subgrid-scale model for compressible turbulence and scalar transport," *Physics of Fluids*, vol. 3, no. 11, pp. 2746-2757, 1991.
- [21] C. D. Pierce and P. Moin, "A dynamic model for subgrid-scale variance and dissipation rate of a conserved scalar," *Physics of Fluids*, vol. 10, no. 12, p. 3041–3044, 1998.
- [22] H. Pitsch, "A C++ program for package for 0D combustion and 1D laminar flames," 1998. [Online]. Available: <https://www.itv.rwth-aachen.de/downloads/flamemaster/>. [Accessed June 2024].
- [23] T. Poinot and D. Veynante, *Theoretical and Numerical Combustion*, RT Edwards, 2005.
- [24] L. Berger, K. Kleinheinz, A. Attili and H. Pitsch, "Characteristic patterns of thermodiffusively unstable premixed lean hydrogen flames," *Proceedings of the Combustion Institute*, vol. 37, no. 2, pp. 1879-1886, 2019.
- [25] Z. Zhou, F. E. Hernández-Pérez, Y. Shoshin, J. A. van Oijen and L. P. de Goey, "Effect of Soret diffusion on lean hydrogen/air flames at normal and elevated pressure and temperature," *Combustion Theory and Modelling*, vol. 21, no. 5, pp. 879-896, 2017.
- [26] E. Pérez-Sánchez, E. Fortes and D. Mira, "Assessment of the flamelet generated manifold method with preferential diffusion modelling for the prediction of partially premixed hydrogen flames," *Combustion and Flames*, vol. Submitted, 2023.
- [27] J. A. van Oijen and L. de Goey, "A numerical study of confined triple flames using a flamelet-generated manifold," *Combustion Theory and Modelling*, vol. 8, no. 1, pp. 141-163, 2004.
- [28] L. Berger, A. Attili and H. Pitsch, "Intrinsic instabilities in premixed hydrogen flames: parametric variation of pressure, equivalence ratio, and temperature. Part 2 – Non-linear regime and flame speed enhancement," *Combustion and Flame*, vol. 240, 2022.
- [29] H. Pitsch, "Large-Eddy Simulation of Turbulent Combustion," *Annual Review of Fluid Mechanics*, vol. 38, pp. 453-482, 2006.
- [30] M. Vázquez, G. Houzeaux, S. Koric, A. Artigues, J. Aguado-Sierra, R. Arís, D. Mira, H. Calmet, F. Cucchietti, H. Owen, A. Taha, E. Burness, J. Cela and M. Valero, "Alya: Multiphysics engineering simulation toward exascale," *Journal of Computational Science*, vol. 14, pp. 15-27, 2016.
- [31] P. Boivin, C. Jiménez, A. Sánchez and F. Williams, "An explicit reduced mechanism for  $\text{H}_2$ -air combustion," *Proceedings of the Combustion Institute*, vol. 33, no. 1, pp. 517-523, 2011.

## D2.3 - Report on simulation framework for H<sub>2</sub>/O<sub>2</sub> and H<sub>2</sub>/air combustion

- [32] E. Fortes, E. Pérez-Sánchez, A. Both, T. Grenga and D. Mira, "Analysis of thermodiffusive instabilities in hydrogen premixed flames using a tabulated flamelet model," *International Journal of Hydrogen Energy*, vol. Submitted, 2024.
- [33] A. Vreman, "An eddy-viscosity subgrid-scale model for turbulent shear flow: Algebraic theory and applications," *Physics of Fluids*, vol. 16, no. 10, p. 3670–3681, 2004.
- [34] M. Burke, M. Chaos, Y. Ju, F. Dryer and S. Klippenstein, "Comprehensive H<sub>2</sub>/O<sub>2</sub> kinetic model for high-pressure combustion," *International Journal of Chemical Kinetics*, vol. 44, no. 7, pp. 444-474, 20212.
- [35] E. Fortes, E. Pérez-Sánchez, T. Grenga, M. Gauding, H. Pitsch and D. Mira, "Large-eddy simulations of a lean hydrogen premixed turbulent jet flame with tabulated chemistry," in *13th Mediterranean Combustion Symposium*, Submitted.
- [36] P. Smith, D. Golden, M. Frenklach, N. Moriarty, B. Eiteneer, M. Goldenberg, C. Bowman, R. Hanson, S. Song, C. William, J. Gardiner, V. Lissianski and Z. Qin, "GRI-mech web site," 1999. [Online]. Available: <http://www.me.berkeley.edu/gri-mech/>.
- [37] G. Jiang and J. Chen, "Efficient Implementation of Weighted ENO Schemes," *Journal of Computational Physics*, vol. 126, no. 1, pp. 202-228, 1996.
- [38] O. Desjardins, G. Blanquart, G. Balarac and H. Pitsch, "High order conservative finite difference scheme for variable density low mach number turbulent flows," *Journal of Computational Physics*, vol. 227, 2008.
- [39] M. Germano, U. Piomelli, P. Moin and W. H. Cabot, "A dynamic subgrid-scale eddy viscosity model," *Physics of Fluids*, vol. 3, pp. 1760-1765, 1991.
- [40] H. Böttler, H. Lulic, M. Steinhausen, X. Wen, C. Hasse and A. Scholtissek, "Flamelet modeling of thermo-diffusively unstable hydrogen-air flames," *Proceedings of the Combustion Institute*, pp. 1567-1576, 2023.
- [41] W. Zhang, S. Karaca, J. Wang, Z. Huang and J. v. Oijen, "Large eddy simulation of the Cambridge/Sandia stratified flame with flamelet-generated manifolds: Effects of non-unity Lewis numbers and stretch," *Combustion and Flame*, pp. 106-119, 2021.
- [42] J. A. M. d. Swart, R. J. M. Bastiaans, J. A. v. Oijen and L. P. H. d. Goey, "Inclusion of Preferential Diffusion in Simulations of Premixed Combustion of Hydrogen/Methane Mixtures with Flamelet Generated Manifolds," *Flow Turbulence Combust*, p. 473–511, 2010.
- [43] N. Mukundakumar, D. Efimov, N. Beishuizen and J. v. Oijen, "A new preferential diffusion model applied to FGM simulations of hydrogen flames," *Combustion Theory and Modelling*, pp. 1245-1267, 2021.
- [44] R. Kai, T. Tokuoka, J. Nagao, A. L. Pillai and R. Kurose, "LES flamelet modeling of hydrogen combustion considering preferential diffusion effect," *International Journal of Hydrogen Energy*, pp. 11086 - 11101, 2023.
- [45] X. Liu, W. Shao, X. B. Ce Liu, Y. Liu and Y. Xiao, "Numerical study of a high-hydrogen micromix model burner using flamelet-generated manifold," *International Journal of Hydrogen Energy*, pp. 20750-20764, 2021.
- [46] F. Almutairi, K. R. Dinesh and J. v. Oijen, "Modelling of hydrogen-blended dual-fuel combustion using flamelet-generated manifold and preferential diffusion effects," *International Journal of Hydrogen Energy*, pp. 1602 -1624, 2023.
- [47] ANSYS Inc., Ansys Fluent Release 2023 R1, Canonsburg, PA, USA, 2023.

### D2.3 - Report on simulation framework for H<sub>2</sub>/O<sub>2</sub> and H<sub>2</sub>/air combustion

- [48] ANSYS Inc., Ansys Fluent Customization Manual, Canonsburg, PA, USA, 2023.
- [49] ANSYS Inc., Ansys Fluent Theory Guide, Canonsburg, PA, USA, 2023.
- [50] F. Menter, "Two-equation eddy-viscosity turbulence models for engineering applications," *AIAA*, p. 1598–1605, 1994.
- [51] J. Jiang, X. Jiang and M. Zhu, "A computational study of preferential diffusion and scalar transport in nonpremixed hydrogen-air flames," *International Journal of Hydrogen Energy*, pp. 15709-15722, 2015.
- [52] N. Burali, S. Lapointe, B. Bobbitt, G. Blanquart and Y. Xuan, "Assessment of the constant non-unity Lewis number assumption in chemically-reacting flows," *Combustion Theory and Modelling*, pp. 632-657, 2016.
- [53] L. Verhoeven, W. Ramaekers, J. van Oijen and L. De Goey, "Modeling non-premixed laminar co-flow flames using flamelet-generated manifolds," *Combustion and Flame*, pp. 230-241, 2012.

# Get in touch

## Website

<http://hyinheat.eu/>

## Email address

[info@hyinheat.eu](mailto:info@hyinheat.eu)

